DEVELOPMENT OF SIMULATION TOOLS, CONTROL STRATEGIES, AND A HYBRID VEHICLE PROTOTYPE

A Thesis
Presented to
The Academic Faculty

by

Dekun Pei

In Partial Fulfillment
of the Requirements for the Degree
Master of Science in the
School of Mechanical Engineering

Georgia Institute of Technology
December 2012

DEVELOPMENT OF SIMULATION TOOLS, CONTROL STRATEGIES, AND A HYBRID VEHICLE PROTOTYPE

Approved by:

Dr. Michael J. Leamy, Advisor
School of Mechanical Engineering
Georgia Institute of Technology

Dr. Aldo A. Ferri
School of Mechanical Engineering
Georgia Institute of Technology

Dr. Nader Sadegh
School of Mechanical Engineering
Georgia Institute of Technology

Date Approved: November 6, 2012

Dedicated to my father and mother.

ACKNOWLEDGEMENTS

First and foremost I would like to thank my advisor Dr. Michael Leamy, whose time, patience and guidance was invaluable to my research. Not only did Dr. Leamy provide his knowledge and resources to my academic work, he shared with me his experience and insight into other areas of life as well. Most importantly, he always challenged me to go outside my comfort zone, which helped me discover new knowledge and experience. Additionally, I would like to thank Dr. Aldo Ferri and Dr. Nader Sadegh, who took their valuable time to serve on my thesis committee and to provide their helpful feedback. I must also thank Dr. Andrei Fedorov, Dr. Gregg Larson and Dr. David Taylor, all of whom played pivotal roles in my decision to attend graduate school.

I would also like to thank John Arata, who left a wealth of information for me to kick start my research on hybrid electric vehicles. Additionally, I enjoyed working with Haider Ali, Laith Gammoh, Michael Hooper, Elsa Johnson, Kyle Karlson and Keong Yong on the hydraulic hybrid bus project. Conversations, both academic and otherwise, with my other lab mates Jason Kulpe, Kevin Manktelow, and Farzard Sadeghi, also helped make my graduate study interesting.

Lastly, I would like to thank those who are closest to me in life. Without the motivation from my father and mother, I would never have started this whole adventure. Even when I seem to take to the air on my own, my parents are always right below to catch me should I fall. In addition, my godfather and godmother also provided their advices and encouragements over the past six years. Finally, my girlfriend, Rachel Andrews, was always there for me to cheer me up when I needed her the most.

TABLE OF CONTENTS

LIST OF TABLES

LIST OF FIGURES

LIST OF ABBREVIATIONS

AHS-II	Allison Hybrid System II
A-ECMS	Adaptive Equivalent Cost Minimization Strategy
BLS	Backward-looking simulation
BSFC	Brake specific fuel consumption
CAFE	Corporate Average Fuel Economy
CL	Clutch
DP	Dynamic programming
ECU	Engine control unit
EVT	Electrically variable transmission
ECMS	Equivalent Cost Minimization Strategy
EM	Electric machine
FE	Fuel economy
FLS	Forward-looking simulation
FWD	Front-wheel drive
GM	General Motors
HEV	Hybrid electric vehicle
HHB	Hydraulic hybrid bus
HHV	Hydraulic hybrid vehicle
HP	High pressure
HWFET	Highway Fuel Economy Driving Schedule, represents highway driving under 60 MPH (97 km/h)
IC engine	Internal combustion engine
I/O	Input/output

km/h	Kilometers per hour
LA92	Unified driving schedule, represents a mix of urban and highway driving
LP	Low pressure
MPG	Miles per gallon
MPH	Miles per hour
NYCC	New York City Cycle, represents low speed stop-and-go traffic driving
PCB	Printed circuit board
PG	Planetary gear set
PM	Pump/motor
PWM	Pulse-width modulation
RPM	Revolutions per minute
SOC	Battery state of charge
THS-II	Toyota Hybrid System II
UDDS	Urban Dynamometer Driving Schedule, represents city driving conditions
US06	Supplemental Federal Test Procedure, represents high acceleration aggressive driving

LIST OF SYMBOLS

a	Vehicle acceleration (m/s)
$\boldsymbol{\alpha_w}$	Angular acceleration of the wheels (rad/s^2)
A	Vehicle frontal area (m^2)
$\boldsymbol{\beta}$	Tangent scaling factor (g/kw-h)
C_d	Drag coefficient
$\boldsymbol{\delta}$	Vehicle mass factor
f_r	Rolling resistance factor
$\boldsymbol{g}$	Acceleration of gravity (m/s^2)
$\boldsymbol{g_0}$ and $\boldsymbol{g_N}$	Initial and final cost
$\boldsymbol{F_k}$	State transition function
F_{req}	Required force at the wheel (N)
$\boldsymbol{h_k}$	Incremental cost in dynamic programing
i	Gear ratio
$\boldsymbol{J_k}$	Cost to end of cycle
$\boldsymbol{k}$	Specific heat capacity ratio
$\boldsymbol{k_L}$, $\boldsymbol{k_{LP}}$, $\boldsymbol{k_{LD}}$, $\boldsymbol{k_{L\omega}}$, $\boldsymbol{k_F}$, $\boldsymbol{k_{FP}}$, $\boldsymbol{k_{FD}}$, and $\boldsymbol{k_{F\omega}}$	Correlating efficiency coefficients for the pump/motor
M	Mass (kg)
$\boldsymbol{\dot{m}_{fuel}}$	Mass flow rate of fuel (g/s)
N	Gear tooth number
$\boldsymbol{\eta}$	Efficiency
ω	Angular velocity (rad/s)

$\boldsymbol{P_{PM}}$	Pressure difference across the pump/motor inlet and outlet
$\boldsymbol{P_{bat}}$	Battery power (kw)
$\boldsymbol{P_{gas}}$	Pressure of the gas in an accumulator
$\boldsymbol{\phi_k}$	Constraint violation cost
$\boldsymbol{q_{p/m}}$	Pumping/motoring flow rate
r	Radius (m)
ρ_1 and ρ_2	Planetary gear set characteristic ratio
ρ_{air}	Density of air (kg/m^3)
s	Equivalence factor (g/kw-h)
$\boldsymbol{\sigma_{shift}}$ and $\boldsymbol{\sigma_{thr}}$	Transmission shift signal and throttle signal in Simulink simulations
SOC	Battery state of charge
Subscripts *e* and *EM*	Indicates quantities related to engine and electric machine
Subscripts *m* and *p*	Indicates quantities related to motoring and pumping of a pump/motor
Subscripts *pre* and *max*	Indicates pre-charge and maximum for pressures
Subscripts *R*, *C*, and *S*	Indicates quantities related to ring, carrier and sun gears of a planetary gear set
T	Torque (Nm)
$\boldsymbol{v}$	Vehicle acceleration (m/s^2)
$\boldsymbol{u_k}$	Control variable
$\boldsymbol{x_k}$	State variable

SUMMARY

This thesis (1) reports the development of simulation tools and control strategies for optimizing hybrid electric vehicle (HEV) energy management, and (2) reports the design and testing of a hydraulic hybrid school bus (HHB) prototype. A hybrid vehicle is one that combines two or more energy sources for use in vehicle propulsion. Hybrid electric vehicles have become popular in the consumer market due to their greatly improved fuel economy over conventional vehicles. The control strategy of an HEV has a paramount effect on its fuel economy performance. In this thesis, backward-looking and forward-looking simulations of three HEV architectures (parallel, power-split and 2-mode power-split) are developed. The Equivalent Cost Minimization Strategy (ECMS), which weights electrical power as an equivalent fuel usage, is then studied in great detail and improvements are suggested. Specifically, the robustness of an ECMS controller is improved by linking the equivalence factor to dynamic programming and then further tailoring its functional form. High-fidelity vehicle simulations over multiple drive-cycles are performed to measure the improved performance of the new ECMS controller, and to show its potential for online application.

While HEVs are prominent in the consumer market and studied extensively in current literature, hydraulic hybrid vehicles (HHVs) only exist as heavy utility vehicle prototypes. The second half of this thesis reports design, construction, and testing of a hydraulic hybrid school bus prototype. Design considerations, simulation results, and preliminary testing results are reported, which indicate the strong potential for hydraulic hybrids to improve fuel economy in the school bus vehicle segment.

CHAPTER 1

INTRODUCTION AND BACKGROUND

1.1 Motivation

Transportation has integrated into every aspect of modern societies because it allows transference of natural resources, finished goods, and human between distant locations. However, transportation depends on a non-renewable natural resource – crude oil. Because of the ever increasing price of crude oil and the environmental impact of using it, there has been increased interest in fuel efficient vehicle technology from the government, consumers and car manufacturers.

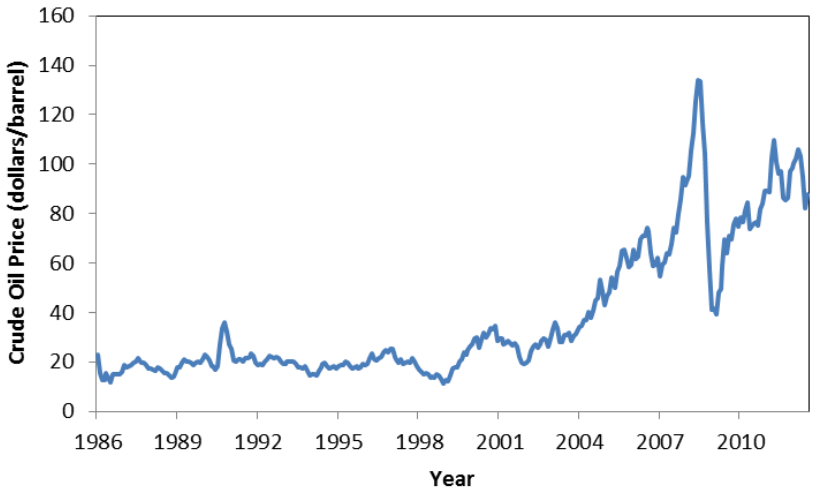

Figure 1.1: Historic prices (not adjusted for inflation) of West Texas Intermediate (WIT) grade crude oil, produced with data from [1]

Since the US domestic oil production peaked in the 1970s, crude oil price in the US skyrocketed due to the increased dependence on imported oil [1]. Figure 1.1 illustrates the crude oil price in the US since 1986. The price of crude oil has risen from an average

of $15 per barrel in 1986 to $97 per barrel in 2012, with an all-time high of $134 in 2008. When adjusted for inflation, the price of crude oil more than tripled in the 26-year period shown. More importantly, the rate of increase started to accelerate at an alarming pace at the turn of the Twenty-first Century.

Transportation suffers the most severe impact from oil price fluctuations, for that the industry uses 72% of the crude oil in the U.S. [2]. Furthermore, alternative fuel vehicles such as electric or hydrogen fuel vehicles have not matured enough for widespread use. As a result, hybrid vehicles have become the most promising technology to bridge the gap between fossil fuel and alternative fuel vehicles. Since introduction of hybrid vehicles in the U.S. market in 1999, consumers' interest in hybrid vehicles have skyrocketed. As shown in Figure 1.2, new hybrid vehicle sales in the US have risen almost every year while overall new consumer vehicles sales decrease in the same period [3]. The decline after 2007 can be attributed to the start of Great Recession in 2008, and this decrease is mirrored in the overall new car sales as well. The car manufacturers responded to consumer's demand by expanding the number of hybrid models available from 1 in 1999 to 25 in 2012 [4].

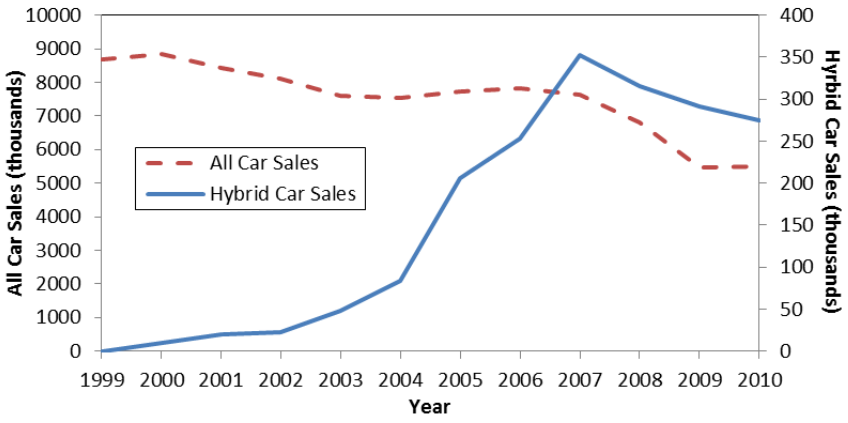

Figure 1.2: Statistics of new car sales in the U.S.

Stricter government regulations also play a role for the increasing interest in hybrid vehicle technology, and the most prominent rule is the Corporate Average Fuel Economy (CAFE) [2,5]. CAFE rules, first enacted in 1970s and revamped by the Obama administration in 2011, regulate the sale-weighted fleet average fuel economy (FE) of consumer vehicle manufacturers. The CAFE regulations are intended to reduce overall oil consumption and emissions, while also increasing long-term fuel savings for vehicle owners. The average FE of the U.S. passenger vehicle fleet is set to increase by as much as 66% from the 2012 level by the year of 2025 under the CAFE regulations [5]. The 2025 FE requirement of 54.5 miles per gallon (MPG) cannot be met by any conventional fossil fuel vehicle sold in the US in the year of 2012, and this will only further drive the hybridization of the passenger vehicles in the future. The overhaul in 2011 also includes new regulations for medium and heavy-duty vehicles (*e.g.*, semi-trucks, heavy-duty pickup, and buses), requiring FE increases ranging from 10 to 20% by the year of 2018 [5]. As a result of all aforementioned conditions, there is an urgent need for advancing the development of hybrid vehicle technology.

1.2 HEV Architecture Overview

A hybrid vehicle uses two or more types of power plants for the purpose of propulsion. A hybrid electric vehicle (HEV) uses an internal combustion (IC) engine and one or more electric machines (EM) as power plants. IC engines have a narrow range of efficient operating conditions, typically under full throttle and mid RPM operations. Inclusion of an EM in the powertrain avoids inefficient low power engine operations. Additionally, an EM supplements the IC engine in terms of torque characteristic since an EM's full torque is available from near zero speed; this ultimately leads to sizing of

smaller and more efficient engines. Lastly, the EM can recapture some of the vehicle's braking energy that would be otherwise lost. Efficient cooperation of the two types of power plants must be ensured to optimize the overall efficiency of the powertrain. There are three major types of powertrain configuration for HEVs: series, parallel and power-split [6,7]. Figure 1.3 depicts the basic powertrain layouts of these three architectures. This section will further detail the characteristics of these architectures.

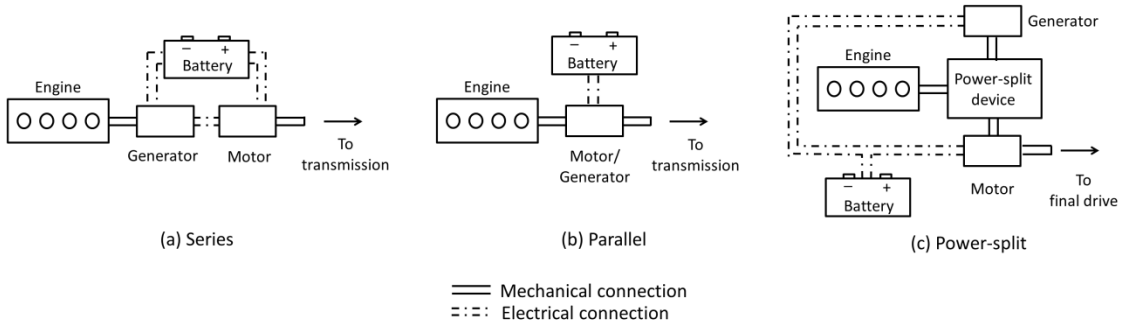

Figure 1.3: Three major types of HEV architectures: (a) series, (b) parallel, and (c) power-split

1.2.1 Series Architecture

A series HEV employs a full size engine to drive an electric generator which in turn powers a traction motor as depicted in Figure 1.3(a). The engine-generator combination on the series architecture can always operate at its maximum efficiency independent of wheel speed or torque requirement, while the battery acts as an energy buffer. The control logic for the series architecture is also relatively simple because of the simplicity of the layout and because only one EM drives the wheel. The series architecture necessitates a full-sized engine, generator and traction motor, which lead to higher cost.

The series architecture has been commonly used in diesel-electric locomotives and ships, but can also be found in a few passenger vehicles, namely the Chevrolet Volt (strictly a power-split, but used predominantly in series mode) and the lesser-known Fisker Karma [53,54].

1.2.2 Parallel Architecture

Shown in Figure 1.3(b), parallel HEVs use a full-sized or reduced-sized engine, augmented with an electric machine that acts as both a generator and a motor. Fuel economy improvement is achieved through engine downsizing and regenerative braking. Since both the engine and the EM drive the wheels, power plant sizing is more flexible than in the series case. However, inefficient engine operations can occur as the engine is not decoupled from the wheels. Furthermore, the power division between the two power plants must be optimized properly, leading the more complicated control logic than in the series architecture.

Honda is an example of an automaker employing predominantly parallel-type hybrid vehicles. The Honda Insight, Civic Hybrid and the CR-Z all use the parallel architecture with an electric machine installed at the engine crank output [55]. Honda elects to use a relatively small (~10 kW) electric machine that primarily assists the engine and recaptures braking energy. However, this architecture is not capable of taking off on electric power only. On the hand, Hyundai employs a larger (~30 kW) electric machine in its Sonata Hybrid and it is capable of operating in pure electric mode up to 74 MPH [56].

1.2.3 Power-split Architecture

Power-split HEVs combine the features of the series and parallel architectures by using two EMs with a power-split device to realize a continuously variable transmission. Figure 1.3(c) shows a schematic of this architecture. This type of transmission typically uses one or more planetary gear sets as the power-split device and is sometimes termed an Electrically Variable Transmission (EVT) [8]. The generator varies the gear ratio in the transmission as well as generates electricity from engine power, while the motor provides extra tractive torque and regenerative braking. The continuously variable gear ratio in the transmission allows more efficient operation of the engine than that in a parallel architecture. Inclusion of a traction motor also leads to downsizing of the engine, further increasing the overall powertrain efficiency. Due to its complexity, the power-split architecture requires the most complicated control logic of the three architectures described.

A prominent example of a vehicle employing a power-split architecture is the Toyota Prius [8]. Despite using the most complex type out of the three primary hybrid architectures, the Toyota Prius was the first mass-produced hybrid vehicle and by far the best seller to-date. General Motors developed a multiple-split form of the power-split architecture [34,35] for use primarily in larger vehicles (e.g, small and large sport utility vehicles and light trucks).

1.3 HEV Control Strategy Literature Review

The control strategies for HEV can be classified into rule-based strategies and optimization-based strategies [6]. Rule-based strategies are based on heuristics and engineering intuition, and they are typically easier to implement. On other hand,

optimization-based strategies optimize for a performance metric systematically; depending on the optimization methods, these strategies are not always implementable. This section will give a review of the recent control strategy development.

1.3.1 Rule-based Control Strategies

Deterministic rules-based strategies for HEV typically seek to keep battery state of charge (*SOC*) at a certain level while fulfilling drivers' torque command [6]. Thermostat or on/off control lets the battery pack operate between a maximum and a minimum. The EM charges the battery when *SOC* reaches the minimum and discharges it when *SOC* reaches the maximum. On the other hand, the maximum *SOC* strategy seeks to maintain the battery *SOC* at its highest level while meeting torque demands. This ensures electrical tractive power is always available, at the expense of sacrificing some regenerative braking capabilities. Fuzzy rule-based strategies that replace exact rules with approximate ones are also applied to HEV control [9,10]. While rule-base methods are easy to implement, they often require extensive tuning and result in sub-optimal control strategies.

1.3.2 Optimization-based Control Strategies

Optimization-based strategies seek to optimize for a set of performance metrics. Global optimization of the HEV operation can be achieved for a known time horizon and operating conditions, such as in the case of optimizing for a drive cycle. Dynamic programming (DP) is often employed to find an absolute optimal operation policy for a specific drive cycle, and it serves as a benchmark for other control strategies [11-16]. The optimization can even be multi-objective, as in the case of optimizing for fuel economy (FE) and emissions simultaneously [12]. However, since DP requires the future

knowledge of the operation conditions and heavy computational loads, vehicle online implementation is not possible. Nevertheless, attempts have been made to extract heuristic rules from dynamic programming results [12,13].

Pontryagin's Minimum Principle (PMP) is based on instantaneous minimization of a Hamiltonian function over a drive cycle [16,17]. Kim *et al.* derived an application of PMP for a power-split architecture [16]. They showed that, for the same boundary conditions, the solution from PMP is unique in the HEV control problem, which implies that it is the globally optimal solution. By setting a correct initial guess of the co-state, instantaneous minimization of the Hamiltonian function through a drive cycle results in a control policy that closely matches results from DP when the state boundary conditions are met. Since PMP is a shooting method that solves a boundary value problem, the resulting control strategy is not causal and thus not online implementable.

A more readily implemented approach to the HEV supervisory control problem is the Equivalent Consumption Minimization Strategy (ECMS) [8,17-20]. It is based on the instantaneous minimization of a cost index, which is the sum of a number of operation metrics weighted by equivalence factors. The commonly used metrics in HEV control are engine fuel usage rate and battery power. ECMS was first developed based on the heuristic concept that the usage of battery power will ultimately result in a future usage of fuel [18]. Many authors have since showed that ECMS is an approximation to PMP [16,17]. ECMS has been viewed as a promising online implementable strategy due its causal nature and ability to produce results almost as good as DP [11,19].

1.4 HHV Background

While HEVs are widespread in the consumer market and have been studied extensively in current literature, hydraulic hybrid vehicles (HHVs) exist mostly as heavy utility vehicles prototypes [21]. Hydraulic hybrid vehicles are analogous to HEVs: instead of EMs, hydraulic pump/motors (PMs) hybridize a powertrain to provide extra motoring power and regenerative braking; instead of batteries, gas-charged accumulators act as energy buffers to power the PMs and to store regenerative braking energy. All three architectures (series, parallel and power-split), are applicable to HHVs and so are the aforementioned control strategies. This section will focus on providing a brief overview on current development of HHVs.

Presently, there exist HHV prototypes of all three primary architectures described for HEVs. The United States Environmental Protection Agency (EPA), in partnership with various companies, has produced prototypes of a wide array of series and parallel HHVs [21]. The prototypes range from a series delivery truck that produces 60-70% fuel economy improvement to a parallel Ford F-550 truck with 20-30% fuel economy improvement, as well as a passenger car test chassis with a series architecture. On the other hand, researchers from Monash University in Australia have fit a six-wheel-drive military vehicle with a parallel hydraulic hybrid architecture. In controlled acceleration and deceleration runs, fuel saving and acceleration improvement with this parallel architecture are reported to be 26.77% and 38%, respectively [22]. Finally, the Center for Compact and Efficient Fluid Power (CCEFP) headed by University of Minnesota, has produced a functional power-split HHV on an all-terrain vehicle. However, the vehicle

chassis is not built for high speed road use and suffers vehicle stability issues at speed over 25 miles per hour (MPH) [23].

Compared to studies of HEVs, relatively little literature studies control strategies of HHVs specifically. Nevertheless, thermostat control and fuzzy logic control for HHVs have been described by Kim *et. al.* and Matheson *et. al*. [24,25]. Furthermore, a rule-based control derived from DP results has also been studied for a parallel HHV [26]. Lastly, feasible mechanical configurations for a power-split HHV have been found from exhaustively studying all possible power-split configurations in [27].

1.5 Contribution and Organization

This thesis (1) reports the development of simulation tools and control strategies for optimizing hybrid electric vehicle (HEV) energy management, and (2) reports the design and testing of a hydraulic hybrid school bus (HHB) prototype. In Chapter 2 and 3, the backward-looking simulations (BLS) and forward-looking simulations (FLS) of three types of HEV architectures (*i.e.*, parallel, power-split and 2-mode power-split) will be developed. The Equivalent Cost Minimization Strategy (ECMS), which weights electrical power as an equivalent fuel usage, is studied in great detail and improvements are suggested in Chapter 2. Specifically, the robustness of an ECMS controller is improved by linking the equivalence factor to dynamic programming and then further tailoring its functional form. Simulations over multiple drive cycles performed on parallel and power-split architectures are used to examine the robustness of the new ECMS controller. Chapter 3 explores the online application potential of the new robust ECMS controller on a 2-mode power-split architecture. Forward-looking simulations are used which mimic the command structure of actual vehicles and simulate component

dynamics in high fidelity. Chapter 4 reports design, construction, and testing of a hydraulic hybrid school bus prototype and seeks to explore a new application of hydraulic hybrids. Design considerations, simulation results, and preliminary performance measures are reported, which indicate the strong potential for hydraulic hybrids to improve fuel economy in the school bus vehicle segment. Lastly, Chapter 5 provides concluding remarks for the thesis and suggestions for future work.

CHAPTER 2

DEVELOPMENT OF DYNAMIC PROGRAMMING-INFORMED EQUIVALENT COST MINIZATION CONTROL STRATEGIES FOR HYBRID ELECTRIC VEHICLES

2.1 Introduction

This chapter presents a direct mathematical approach for determining the state of charge-dependent equivalent cost factor in hybrid electric vehicle (HEV) supervisory control problems using globally-optimal dynamic programming (DP). The equivalence factor is then further modified with corrections based on battery state of charge, with the aim of making it robust to drive cycle and component variations. This results in a new robust DP-informed Equivalent Cost Minimization Strategy (ECMS). Simulations performed on parallel and power-split HEV architectures demonstrate the cross-platform applicability and cross-drive-cycle robustness of the DP-informed ECMS approach. The controller approach detailed should result in ECMS supervisory controllers that can achieve near optimal fuel economy (FE) performance, even if component parameters vary from assumed values (*e.g.*, due to manufacturing variation, environmental effects or aging), or actual driving conditions deviate largely from standard drive cycles

As discussed in the Chapter 1, while rule-based control strategies are easy to implement, they are often suboptimal and require extensive tuning. However, optimization-based control strategies are not always online implementable due to their high computation loads or non-causal natures. The Equivalent Cost Minimization Strategy is a promising optimization-based control strategy because it uses instantaneous

optimization and it can produce near-optimal results. In HEV control problems, the equivalent cost is usually defined as the following,

$$C = \dot{m}_{fuel} + sP_{bat} \tag{2.1}$$

where $\dot{m}_f$ denotes the mass flow rate of fuel, P_{bat} is the power of the battery required to operate the EM, C denotes the equivalent cost, and s the equivalence factor. As appeared in Eq. (2.1), the equivalence factor would convert the battery power into an equivalent amount of fuel and would have the unit of mass rate over power.

The definitions of the equivalence factor vary greatly in the literature. Some authors derive the equivalence factor by considering the average power conversion efficiency between battery power and fuel [18,20]. Two equivalence factors, s_{cha} and s_{dis}, are sometimes employed for charging and discharging operations of the battery - this difference accounts for the non-constant electric efficiency of the battery. The weakness of this approach is that engine operating points, and thus engine thermal efficiency, can vary from that predicted. Poor estimation of the equivalence factor can result in poor FE. Drive cycle specific optimization of s_{cha} and s_{dis} is also used [11], but it shares the same weakness of a possible mismatch between actual operation conditions and prediction. Adaptive ECMS (A-ECMS) overcomes this weakness by updating *s* according to actual operating conditions [19]. However, the A-ECMS approach still requires problematic predictors of future operating conditions.

A second issue arising in the HEV supervisory control problem is the need for battery charge sustaining operation to ensure battery life. This is not explicitly addressed in Eq. (2.1). Many authors propose that the equivalence factor be defined as a function of battery state of charge – *i.e.*, $s(SOC)$ [8,11,20,]. The implementations are similar in

spirit: define a reference value of *SOC* and decrease the equivalence factor when the battery *SOC* is higher than the reference value, and vice-versa. Serrao *et al.* [11] used a tangent type function resulting in an equivalence factor that stays nearly constant until close to the limits of SOC operation range. On the other hand, Arata *et al.* [8] set two equivalence factors, s_{min} and s_{max}, at the battery *SOC* operation limits and defined $s(SOC)$ within the operation limits using a linear function or an inverse-tangent function. Sciarretta *et al.* [15] approached the charge sustaining problem differently than the others - they defined a probability factor based on current electrical energy usage and predicted future energy usage, and this probability factor was used to weight between two equivalence factors, s_{cha} and s_{dis}, determined from the marginal tradeoff between engine and electrical energy usage at the end of a driving cycle. The problem of cross drive cycle variations was not addressed by any of these authors.

A well-tuned ECMS controller can be near optimal for a single drive cycle; many authors [11,19,20] present FE figures of a properly tuned ECMS algorithm within 3% of that from DP. However, the tuning of $s(SOC)$ is drive cycle specific. On other drive cycles, if $s(SOC)$ overestimates the cost, the powertrain will not take full advantage of the electrical power. Conversely, if $s(SOC)$ underestimates cost, the battery will be drained too quickly, rendering EM motoring impossible. Furthermore, while the absolute optimal FE is important in theory, robustness is arguably more important since the actual operation of an HEV can often deviate from the vehicle parameters and driving conditions assumed during control algorithm tuning.

In this chapter, a robust ECMS controller is developed directly from dynamic programming. This method builds on the *SOC*-weighted equivalence factor concept from

[8,11,20]. Equations are first derived which yield the reference value of the equivalence factor from DP. The procedure relies on a Pareto optimality criterion to develop minimization conditions that the equivalence cost expression must adhere to in both DP and ECMS. The equivalence factor can be considered as a marginal cost of using electrical power, and it is shown to be very close to that obtained from a brute force optimization method of iterative ECMS simulations. Subsequently, an *SOC* correction in the equivalence factor is introduced to increase robustness of the controller across different drive cycles. The *SOC* correction term varies with the deviation from the reference *SOC* as a tangent function. The robust controller is based on the inherent energy balance in the battery of an optimal ECMS controller. Adaptive logic is also implemented to ensure battery charge sustaining at the reference *SOC*. Two case studies employing the robust controller are done on parallel and power-split HEV architectures to demonstrate the efficacy of the controller. Fuel economy results show that the robust ECMS controller can consistently achieve FE within 1% of the global optima prescribed by dynamic programming across different drive cycles. Extreme robustness tests further demonstrate that the robust controller can keep the FE within 1-2% of the global optimum even when the equivalence factor deviates substantially from the optimal value. This implies that the performance of the robust controller does not depend on having an optimal equivalence factor; and further, it should achieve near optimal FE even if component parameters vary from assumed values, or actual driving conditions deviate largely from standard drive cycles.

2.2 HEV Modeling Approach

This section introduces kinematics of the parallel and power-split HEV architectures used for the case studies. The generic DP and ECMS algorithms and their application to the two HEV architectures are then discussed, followed by development of a new procedure for directly determining the equivalence factor using dynamic programming.

2.2.1 Parallel HEV Architecture

The architecture shown here is a post transmission torque-coupled parallel hybrid electric vehicle. The transmission selected is a 5-speed automated manual transmission. Figure 2.1 depicts the selected architecture and its mechanical and electrical power flows.

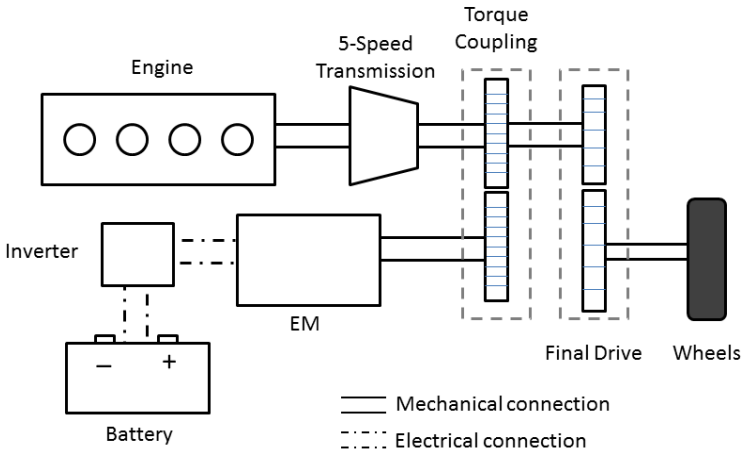

Figure 2.1: Schematic of a post transmission torque-coupled parallel architecture

The engine output is connected to the transmission and the torque output of the transmission (T_0) is coupled with the torque output of the EM (T_{EM}) such that,

$$T_0 + i_{EM} T_{EM} = T_f = \frac{T_w}{i_f} \tag{2.2}$$

where T_f is the torque at the final drive and i_{EM} is the EM gear ratio in the torque coupling. Additionally, T_w denotes the torque at the wheels and i_f denotes the gear ratio of the final drive. The gear ratios of the transmission will be denoted as i_n with n = 1 to 5. The total torque output at the wheels T_w is

$$T_w = i_f i_n T_e + i_f i_{EM} T_{EM} \tag{2.3}$$

Drive cycles from the Environmental Protection Agency (EPA) are used for FE simulations. Using a backward-looking approach, the required force (F_{req}) at the wheels can be computed from a drive cycle as follows,

$$F_{req} = \frac{T_w}{r_w} = f_r M g + \frac{1}{2}\rho_{air} C_d A_f v^2 + \delta M a \tag{2.4}$$

where r_w denotes the rolling radius of the tire, f_r the rolling resistance coefficient, M the mass of the vehicle, g the acceleration of gravity, ρ_{air} the air density, C_d the vehicle's drag coefficient, A_f the frontal area of the vehicle, δ the mass factor used to account for acceleration of rotating bodies on the vehicle, and v the velocity specified by the drive cycle, and a the acceleration calculated from the drive cycle. The acceleration of the vehicle is calculated as the finite difference of vehicle velocity (*i.e.*, $\Delta v/\Delta t$). The speed constraint resulting from the torque coupling requirement is given by,

$$\frac{\omega_e}{i_n i_f} = \frac{\omega_{EM}}{i_{EM} i_f} = \omega_w = \frac{v}{r_w} \tag{2.5}$$

where ω_e, ω_{EM}, and ω_w are the angular velocities of the engine, the EM and the wheels, respectively. The transmission, torque coupling and final drive are comprised of direct gearings and their efficiencies are assumed to be one. The engine and the electric machine are characterized by their torque capability curves. Their efficiency data comes from a brake specific fuel consumption (BSFC) map and a combined motor and inverter

efficiency map, respectively. Finally, the battery is operated within a narrow state of charge range from 0.4 to 0.8. For this reason, the battery can be modeled to have a constant voltage over its operating range [11,16], and thus the turnaround loss at the battery is neglected. The battery power is given by the following,

$$P_{bat} = (\eta_{EM})^{-sgn(\mathrm{T_{EM}}\omega_{\mathrm{EM}})}\mathrm{T_{EM}}\omega_{\mathrm{EM}} \tag{2.6}$$

with the convention that positive battery power indicates discharging of the battery. The variable η_{EM} denotes the combined efficiency of the EM and its inverter. The efficiency term has different definitions depending on the direction of power flow. The signum function in the exponents of the efficiency terms addresses this. The simulation parameters of the parallel hybrid HEV are listed in Table A.1 of Appendix A.

2.2.2 Power-split HEV Architecture

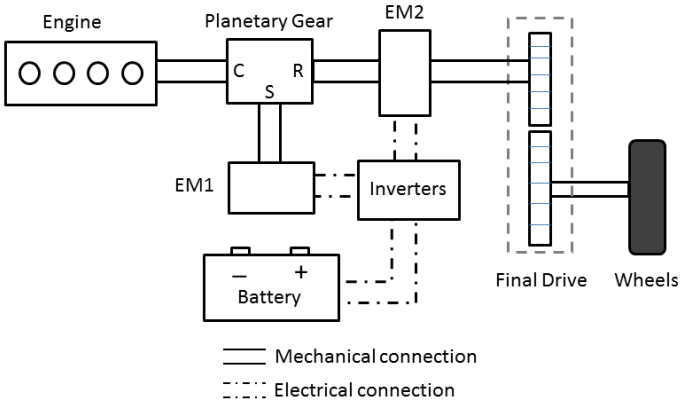

Figure 2.2: Schematic of the THS-II power-split HEV architecture

The power-split architecture considered in this chapter is based on the 2004 Toyota Prius drivetrain (Toyota Hybrid System II, or THS-II). Figure 2.2 depicts the schematic

of the THS-II power-split HEV architecture. The letters *C*, *R*, and *S*, denote the carrier, ring and sun ports on the planetary gear set.

Figure 2.3 shows the structure of the simple planetary gear set used as the power-split device in THS-II. It is comprised of an outer ring gear, an inner sun gear and three pinion gears in the space between the ring and the sun gear. The three pinion gears are connected by a carrier arm (not shown in Figure 2.3), which rotates about the same axis as the ring and sun gears. On the THS-II power-split architecture shown in Figure 2.2, the engine output is connected to the carrier arm of the planetary, while EM1 is connected to the sun gear. Electric machine 2 connects to the ring gear of the planetary, which in turn connects to the final drive of the vehicle.

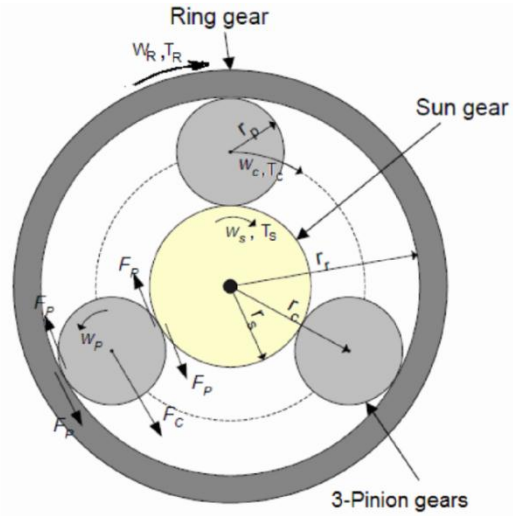

Figure 2.3: Simple planetary gear set, reproduced from [8]

The planetary gear set has a characteristic ratio ρ defined as the tooth-number of the sun gear to the tooth-number on the ring gear. The characteristics ratios defined for the two planetary gear sets have the following relationship,

$$\rho = \frac{N_S}{N_R} = \frac{r_S}{r_R} \tag{2.7}$$

where *N* denotes the tooth-number and *r* the radius.

Reference [29] details the derivation process of the steady-state angular velocity and torque relationships for the simple planetary gear set. The results will be summarized here. In essence, by assuming equal velocities at the contact points, the steady-state angular velocity relationship of the planetary gear set becomes the following,

$$(1+\rho)\omega_C - \rho\omega_S - \omega_R = 0 \tag{2.8}$$

Additionally, by neglecting gear acceleration and performing energy balance on a gear set, the steady-state torque relationship becomes,

$$T_C = (1+\rho)T_R = -\frac{1+\rho}{\rho}T_S \tag{2.9}$$

Note that while the torques have one degree of freedom in the planetary gear set, the three angular velocities have two degrees of freedom. Furthermore, the steady state kinematic and torque constraints on the engine and EMs due to the mechanical connections are,

$$\begin{matrix}\text{Power-split HEV} \\ \text{Mechanical} \\ \text{Constraints}\end{matrix} : \begin{cases} \omega_e = \omega_C \\ \omega_{EM1} = \omega_S \\ \omega_{EM2} = \omega_R \\ T_e = T_C \\ T_{EM1} = T_S \\ T_{EM2} = T_f - T_R \end{cases} \tag{2.10}$$

The planetary gear set has efficiency that is fixed and close to one, thus it can be assumed to have no loss [8,28]. Nevertheless, the engines and EMs are both characterized by their torque capability curves and efficiency maps. The torque and speed at the wheels are,

$$T_w = i_f(T_R + T_{EM2}) = i_f\frac{1}{1+\rho_{simp}}T_e + i_f T_{EM2} \tag{2.11}$$

$$\omega_w = \frac{\omega_R}{i_f} = \frac{(1+\rho)\omega_e - \rho\omega_{EM1}}{i_f} \tag{2.12}$$

The force required at the wheels is same as that presented for the parallel HEV in Eq. (2.4). Note that Eq. (2.12) implies that the engine speed can be varied independent of the wheel speed by changing the speed of ω_{EM1}. Effectively, the simple planetary gear set is a transmission with an infinite number of gear ratios controlled by the speed of EM1.

The battery power expression depends on the direction of power flow in the EMs: the convention is positive powers of EM1 and EM2 deplete the battery. Similar to the parallel hybrid case, the battery itself is modeled to have a constant voltage and no turn around loss due to the narrow *SOC* operation range. All the losses in the conversion from mechanical power to electrical power arise from the combined inefficiencies of the inverters and the EMs. The following expression for battery power describes a total of four scenarios depending on the power flow in the EMs,

$$P_B = (\eta_{EM2})^{-sgn(P_{EM2})} T_{EM2}\omega_{EM2} + (\eta_{EM1})^{-sgn(P_{EM1})} T_{EM1}\omega_{EM1} \tag{2.13}$$

The efficiency terms (η_{EM1} and η_{EM2}) have different definitions depending on the direction of power flow. The signum function in the exponents of the efficiency terms addresses this issue. Finally, the simulation parameters of the power-split HEV are listed in Table A.2 in Appendix A.

2.2.3 Dynamic Programming

A generic dynamic programming adapted from [14] will be presented here. The DP algorithm is used on a class of discrete-time models in the following form,

$$\boldsymbol{x}_{k+1} = \boldsymbol{F}_k(\boldsymbol{x}_k, \boldsymbol{u}_k), \quad k = [0, N-1] \tag{2.14}$$

where k denotes the index of discretized time, $\boldsymbol{x}_k$ the state variable, $\boldsymbol{u}_k$ the control variable, and $\boldsymbol{F}_k$ the function defining the state transition. Additionally, for application of dynamic programming, the state and control variables have to be discretized as well.

The total cost of using the control strategy $\pi = \{\boldsymbol{u}_0, \boldsymbol{u}_1, \dots \boldsymbol{u}_{N-1}\}$ with the initial state $\boldsymbol{x}_0$ is,

$$J_{0,\pi}(\boldsymbol{x}_0) = g_0(\boldsymbol{x}_0) + g_N(\boldsymbol{x}_N) + \phi_N(\boldsymbol{x}_N) + \sum_{k=0}^{N-1} [h_k(\boldsymbol{x}_k, \boldsymbol{u}_k) + \phi_k(\boldsymbol{x}_k, \boldsymbol{u}_k)] \tag{2.15}$$

where $J_{0,\pi}(\boldsymbol{x}_0)$ denotes the total cost, $g_{0/N}(\boldsymbol{x}_{0/N})$ the initial/final cost, $\phi_k(\boldsymbol{x}_k, \boldsymbol{u}_k)$ the penalty function enforcing the constraints on the state and control variables, and $h_k(\boldsymbol{x}_k, \boldsymbol{u}_k)$ the incremental cost of applying the control at time k. The optimal control policy is one that minimizes the total cost represented in Eq. (2.15).

According to the Bellman's Optimality Principle, an optimal control policy will have the property that the optimality of the past action has no effect on the optimality of the future actions [30]. Dynamic programming utilizes this principle by minimizing the cost in Eq. (2.15) backward in time starting from the end time step. To minimize the total cost in Eq. (2.15), the state variable is discretized such that $\boldsymbol{x}_k^i$ represents a point in the discrete state-time space. The state-time space is a space parameterized by the independent states and time; the goal of dynamic programming is to find the trajectory with the least cost through this space. Working backwards, the cost for each state value at the final time step is first evaluated as,

$$J_N(\boldsymbol{x}_N^i) = g_N(\boldsymbol{x}_N^i) + \phi_N(\boldsymbol{x}_N^i) \tag{2.16}$$

At intermediate time steps, the cost at each state point must satisfy,

$$J_k(\boldsymbol{x}_k^i) = \min\left[J_{k+1}(\boldsymbol{x}_{k+1}^i) + h_k(\boldsymbol{x}_k^i, \boldsymbol{u}_k) + \phi_k(\boldsymbol{x}_k^i, \boldsymbol{u}_k)\right] \tag{2.17}$$

which implies an optimal path is taken forward of $\boldsymbol{x}_k^i$. The next step cost $J_{k+1}(\boldsymbol{x}_{k+1}^i)$ is found by first evaluating the state transition from Eq. (2.14), then a nearest neighbor interpolation is carried out to find the corresponding state point $\boldsymbol{x}_{k+1}^i$ at the k+1 time step. The incremental cost term $h_k(\boldsymbol{x}_k^i, \boldsymbol{u}_k)$ and the penalty cost term $\phi_k(\boldsymbol{x}_k^i, \boldsymbol{u}_k)$ are based on current time step k states and controls only. By repeating the process from Eq. (2.17) backward in time to the initial time step, the total minimum cost at each state point is arrived at. Finally, the global minimization is done by selecting the state point with lowest total minimum cost at the initial time step. Using the next time step states ($\boldsymbol{x}_{k+1}^i$) and the optimal control ($\boldsymbol{u}_k$) stored for each point of the state-time space, the optimal state trajectory $\boldsymbol{X}^* = \{\boldsymbol{x}_0^*, \boldsymbol{x}_1^*, \boldsymbol{x}_2^*, \ldots \boldsymbol{x}_{N-1}^*\}$ and the optimal control trajectory $\boldsymbol{U}^* = \{\boldsymbol{u}_0^*, \boldsymbol{u}_1^*, \boldsymbol{u}_2^*, \ldots \boldsymbol{u}_{N-1}^*\}$ can be recovered in a forward sense from the global minimum solution.

2.2.4 Equivalent Cost Minimization Strategy

While the DP algorithm has to be solved backwards in time from the end state and leads to a globally optimal control strategy, it is not implementable online (*i.e.*, in an actual vehicle) when there is limited knowledge of the future operating conditions. Even when the future operating conditions are specified, a strategy based on DP is still computationally prohibitive due to the exponential increase of complexity with the number of independent state and control variables. An alternative is to use an instantaneous cost minimization algorithm, as opposed to the global cost minimization of DP. The Equivalent Cost Minimization Strategy is based on an instantaneous minimization algorithm that minimizes an equivalent cost,

$$C_k = s_1 f_1(\boldsymbol{x}_k, \boldsymbol{u}_k) + s_2 f_2(\boldsymbol{x}_k, \boldsymbol{u}_k) + \cdots + s_n f_n(\boldsymbol{x}_k, \boldsymbol{u}_k) \tag{2.18}$$

where $f_1(\cdot), f_1(\cdot), \ldots f_{\mathrm{n}}(\cdot)$ are performance metrics under consideration and $s_1, s_2, \ldots s_n$ are the equivalence factors weighing each performance metric such the combined metric, or equivalent cost C_k, can be optimized. The equivalence factors need to be optimized so that the design requirements of the system are met.

2.2.5 Application of DP to HEV Supervisory Control

The application of the generic dynamic programming algorithm to the parallel and the power-split HEV architectures is discussed next. The DP algorithm is implemented in MATLAB with backward-looking simulation in which the vehicle is assumed to follow a drive cycle, and the steady state kinematic and torque relationships are used to compute component operation states. The advantage of a backward-looking simulation is the speed-up of computation, which comes at the cost of neglecting energy due to transient effects.

The DP control problem of the parallel HEV is characterized as,

$$\boldsymbol{x} = (SOC, v, F_{req}) \tag{2.19}$$

$$\boldsymbol{u} = (T_e, \omega_e, T_{EM}, \omega_{EM}, i_n) \tag{2.20}$$

$$h_k = \dot{m}_{fuel}(\boldsymbol{x}, \boldsymbol{u}) \tag{2.21}$$

where $\dot{m}_{fuel}$ is the mass rate of fuel burned. The dynamic programming algorithm, applied to HEVs, seeks to minimize the forward fuel consumption at any point of discretized state-time space. This minimizing operation can be summarized in Eq. (2.22),

$$J_k\left(SOC_k^i\right) = \min\left[J_{k+1}\left(SOC_{k+1}^i\right) + \dot{m}_{fuel}(\cdot) + \phi_k(\cdot)\right] \tag{2.22}$$

The constraints on the components' capabilities are summarized as,

$$\text{Parallel HEV Component capability constraints}: \begin{cases} T_{e,min} \le T_e \le T_{e,max} \\ \omega_{e,min} \le \omega_e \le \omega_{e,max} \\ T_{EM,min} \le T_{EM} \le T_{EM,max} \\ \omega_{EM,min} \le \omega_{EM} \le \omega_{EM,max} \\ i_n \epsilon [i_1, i_2, i_3, i_4, i_5] \end{cases} \tag{2.23}$$

For charge sustaining operation of the battery, the following constraints are also applied,

$$SOC_{min} \le SOC \le SOC_{max} \tag{2.24}$$

$$SOC_0 = SOC_N = SOC_{ref} \tag{2.25}$$

These constraints are enforced through the penalty terms $\phi_k(\cdot)$, $g_0(\cdot)$, and $g_N(\cdot)$ described earlier. The penalty terms are several orders of magnitude larger than the h_k term when a constraint is violated; otherwise they are zero.

In general, the computation time of a DP routine increases exponentially with the number of independent state and control variables since all permissible values of state and control variables are visited at each time step. However, the control problem of the parallel hybrid electric vehicle can be simplified by applying certain constraints. In a backward-looking simulation, the vehicle is assumed to follow the drive cycle exactly, therefore the drive cycle prescribes v and F_{req}, making SOC the only independent state variable. Furthermore, one can apply the steady state constraints Eqs. (2.3)-(2.5) to reduce the independent control variables to $\boldsymbol{u} = (T_e, \omega_e)$. Essentially, the control candidates will be constrained to the set meeting the speed and torque requirements at the wheels. Note the number of feasible ω_e choices is limited to at most the number of gear ratios in the transmission due the kinematic constraint from Eq. (2.5). Nevertheless, using $\boldsymbol{u} = (T_e, \omega_e)$ instead of $\boldsymbol{u} = (T_e, i_n)$ as the independent control variables for the parallel HEV facilitates the analogy between the parallel HEV and the power-split HEV in the later discussions. Lastly, $\dot{m}_{fuel}$ is assumed to be only a function of engine

operation points characterized by T_e and ω_e. During application of DP to an HEV, the discretized engine operation point (T_e, ω_e) candidates are searched exhaustively to find the minimization operation point for Eq. (2.22).

The application of dynamic programming to the power-split HEV model is similar to that of the parallel HEV model. Through the applications of kinematic constraints, the independent state and control variables become $x = (SOC)$ and $\boldsymbol{u} = (T_e, \omega_e)$; the incremental cost is also $h_k = \dot{m}_{fuel}(\boldsymbol{x}, \boldsymbol{u})$. Since the power-split HEV uses a second electric machine to vary the effective gear ratio in the powertrain, there is an infinite number of engine speeds for the same road load conditions, as opposed to the case of parallel HEV. The component capability constraints for the powers-split HEV are summarized as the following,

$$\text{Power-split HEV component capability constraints}: \begin{cases} T_{e,min} \le T_e \le T_{e,max} \\ \omega_{e,min} \le \omega_e \le \omega_{e,max} \\ T_{EM1,min} \le T_{EM1} \le T_{EM1,max} \\ \omega_{EM1,min} \le \omega_{EM1} \le \omega_{EM1,max} \\ T_{EM2,min} \le T_{EM2} \le T_{EM1,max} \\ \omega_{EM2,min} \le \omega_{EM2} \le \omega_{EM1,max} \end{cases} \tag{2.26}$$

The power-split architecture will also have the same *SOC* constraints presented for the parallel case in Eqs. (2.24) and (2.25). The constraints on these states are then enforced in DP with a penalty cost term.

The resolution on the state variable plays an important role in determining the accuracy and performance of the DP simulation. If the resolution is set too low, the state trajectory and the resulting FE may get distorted. If the resolution is set too high, the simulation will take excessively long to run. Convergence tests are performed to determine the state variable resolution required for the FE to converge. The convergence tests are done on EPA's UDDS drive cycle with the two HEV architectures previously

discussed. Figure 2.4 depicts FE convergence for the parallel architecture as the number of state discretization points increases. The range of the state variable *SOC* in the DP simulations is [0,1].

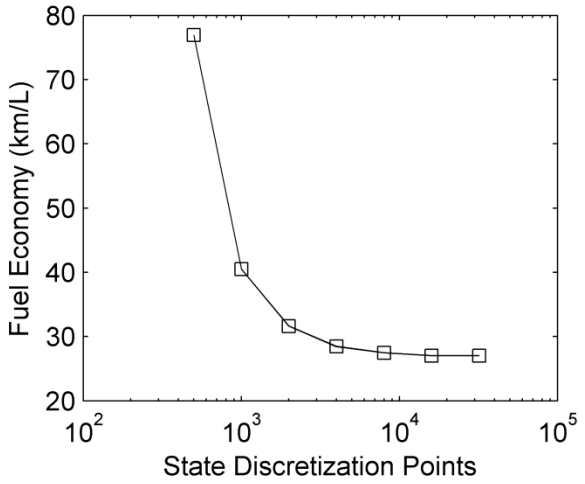

Figure 2.4: Fuel economy convergence with number of state discretization points using the UDDS drive cycle

Figure 2.4 demonstrates that the FE obtained converges as the number of state discretization points increases. From the data in Figure 2.4, it is determined that 16,000 state discretization points (*i.e.*, a resolution of 6.25×10^{-5}) are needed for the approximated error in FE to drop below 1%. A similar convergence test was performed for the power-split HEV and it is found that 16,000 points are also needed for errors less than 1% in predicted FE.

2.2.6 Application of ECMS to HEV Supervisory Control

The ECMS implementation uses the same state and control variables as the DP implementation. However, instead of optimizing for a global minimum of FE over the entire drive cycle, a cost function *C* is minimized at each discrete time *k* in a drive cycle,

$$C = \dot{m}_{fuel} + sP_{bat} + \phi_k(\cdot) \tag{2.27}$$

where s is the equivalence factor (battery power's equivalent fuel usage) and the $\phi_k(\cdot)$ term is included to enforce constraints specified in Eqs. (2.24)-(2.26). Note that the final *SOC* condition in Eq. (2.25) cannot always be enforced with ECMS due to the lack of future operation knowledge; therefore, only the initial *SOC* is specified and enforced. Equation (2.27) is applied directly to both the parallel and power-split HEV with proper definition of the penalty term for component constraints discussed in the DP application. The goal of minimizing the equivalent cost in Eq. (2.27) is to determine an engine operation point for the HEV. However, minimizing Eq. (2.27) at each time instance in a drive cycle (i.e., locally) does not necessarily guarantee global minimization of fuel usage for the entire drive cycle.

The minimizing engine operation point for Eq. (2.27) changes with the equivalence factor *s*. As a result, the value of *s* in Eq. (2.27) must be determined properly in order to achieve desirable fuel economy performance over a drive cycle. Incorrect functional forms for *s* will cause the powertrain to over- or under-value battery power. This will lead to inefficient use of the electric machines, and ultimately lead to poor FE. Two existing methods of estimating the optimal form for *s* will be briefly reviewed in the next section before detailing a new method based on DP marginal cost.

2.2.7 Methods of Estimating Equivalence Factors in ECMS

While the application of DP guarantees optimal FE for a given drive cycle, obtaining optimal FE using the ECMS requires tuning of the equivalence factor. The optimized value for *s* is also drive cycle specific [19], further increasing the difficulty of properly defining *s*. Two existing methods of estimating an optimal functional form for *s* will be

reviewed in this section. The first method uses brute force optimization, while the second method relies on the average efficiency of converting fuel to electrical energy. Finally, a third method based on marginal cost in the HEV drivetrain will be introduced. Subsequent case studies of the parallel and power-split HEV will analyze the effectiveness of these *s* estimation methods using simulation data.

2.2.7.1 Equivalence Factors Based on Direct ECMS Optimization

The first method of finding optimal *s* values for a drive cycle is to iteratively run ECMS simulations. Some authors suggest that two values (s_{cha} and s_{dis}) are needed to account for the different efficiencies in charging and discharging operations of the battery [11,13,15], necessitating a two parameter optimization approach. Musardo *et al.* showed that a single value of *s* can be used with little sacrifice in FE [19]. This approach is followed herein where a single value of *s* will be optimized on a per drive cycle basis since the optimal value of *s* is known to be drive-cycle dependent [11].

2.2.7.2 Equivalence Factors Based on Average Component Efficiency

Since all propulsion power ultimately comes from fuel in an HEV, the equivalence factor can be interpreted as the equivalent amount of fuel represented by a given amount of electrical energy. A classical way to calculate the equivalence factor for ECMS is to consider the average efficiency of converting fuel to electrical energy, as described by Liu *et. al.* in [20],

$$s = \frac{\overline{BSFC}}{\overline{\eta_{bat}} \cdot \overline{\eta_{EM}} \cdot \overline{\eta_i}} \tag{2.28}$$

where η_{bat}, η_{EM} and η_i are the efficiencies of the battery, electric machines and inverters, respectively. The horizontal bar above each variable denotes averaging. The calculation of *s* is made drive-cycle specific by averaging efficiency data obtained from dynamic

programming during the drive cycle. In the case of the power-split hybrid, the efficiency of the second EM and inverter will also be used in Eq. (2.28).

2.2.7 3 Equivalence Factors Based on Marginal Cost in DP

The section will present a third and new method for deriving the value of the equivalence factor from dynamic programming. This method assumes that for a fixed road load condition, the DP operating point minimizes the equivalent cost of an ECMS presented in Eq. (2.27) with the reasonable assumption that the penalty term ϕ_k is zero. From Eq. (2.27), the equivalent cost would be a surface parameterized by both $\dot{m}_{fuel}$ and P_{bat}, which are in turn functions of engine operation points (ω_e, T_e) for a fixed road load condition. By additional insight into the DP minimization process, it can be shown that only a subset $\boldsymbol{U}_{DP}$ of all possible operation points $\{(\dot{m}_{fuel}, P_{bat}) \in \boldsymbol{U}\}$ is used for dynamic programming operation. Furthermore, in this subset $\boldsymbol{U}_{DP}$, the choice of P_{bat} uniquely defines $\dot{m}_{fuel}$ as explained below. With this condition, the equivalent cost in Eq. (2.27) can be considered as only a function of P_{bat}, and its minimization is simplified to two conditions on its derivatives.

The demonstration that P_{bat} uniquely parameterizes $\dot{m}_{fuel}$ will be done by contradiction. Consider Eq. (2.22), which is the cost to be minimized at each point in the state-time space during dynamic programming. For the HEV architectures considered, the independent state and control vectors are $x = SOC$ and $\boldsymbol{u} = (T_e, \omega_e)$, respectively. The incremental cost is solely the engine fuel consumption rate $\dot{m}_{fuel}$, which in turn is only a function of the engine operation point (T_e, ω_e). Equation (2.22) can then be rewritten as,

$$J_k\left(SOC_k^i\right) = \min\left[J_{k+1}\left(SOC_{k+1}^i\right) + \dot{m}_{fuel}(T_e, \omega_e) + \phi_k(SOC_n, T_e, \omega_e)\right] \quad (2.29)$$

Additionally, note that the state transition from SOC_k^i to SOC_{k+1}^i is solely a function of the battery power $P_{bat,k}$ used at time *k*, as in the following,

$$SOC_{k+1}^i - SOC_k^i = \Delta SOC(P_{bat,k}(T_e, \omega_e)) \quad (2.30)$$

Assume starting from the same state SOC_k^i at time *k*, there are two sets of controls (T_e^a, ω_e^a) and (T_e^b, ω_e^b) that use the same battery power and neither of these controls incurs a penalty (*i.e.*, $\phi_k(\cdot) = 0$). This implies the state transition, and thus the next time step cost ($J_{k+1}(\cdot)$), will be the same for both controls. In this case, Eq. (2.29) can be satisfied by minimizing $\dot{m}_{fuel}(T_e, \omega_e)$. By this token, only the control with the lowest fuel rate will be used for a given battery power. In other words, DP confines engine operations to fuel rate minimizing operations for a given battery power. These engine operation points can be considered as a Pareto-optimal operation front [31]. Figure 2.5 illustrates an example of Pareto-optimal operation points as compared to all operation candidates. Under this consideration, the fuel rate can be parameterized by the battery power as $\dot{m}_{fuel}^{DP}(P_{bat})$. This simplifies the conditions for minimizing Eq. (2.27) to,

$$\frac{dC}{dP_{bat}} = \frac{d\dot{m}_{fuel}^{DP}(P_{bat})}{dP_{bat}} + s = 0 \quad (2.31)$$

$$\frac{d^2C}{d(P_{bat})^2} = \frac{d^2\dot{m}_{fuel}^{DP}(P_{bat})}{d(P_{bat})^2} > 0 \quad (2.32)$$

Equation (2.30) can be used to derive a DP-informed *s* value for ECMS operation. This definition of *s* can be considered a marginal cost of using the electrical power.

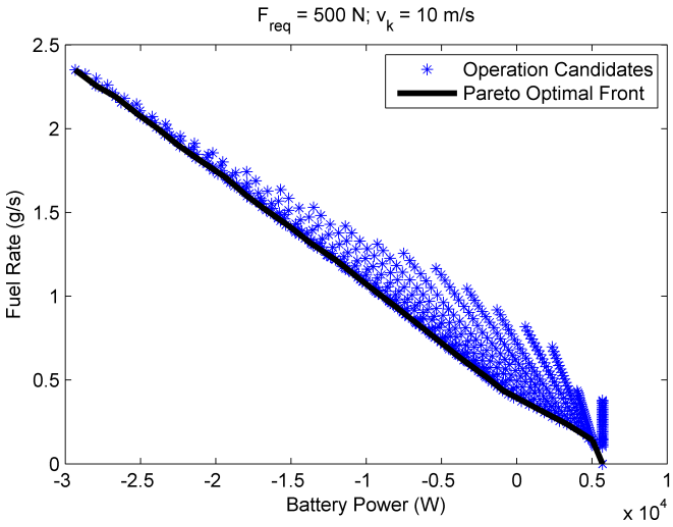

Figure 2.5: Pareto-optimal operation points for the power-split HEV

2.3 Results from Controller Case Studies

In the case studies of parallel and power-split HEVs, the comparison of the different methods of estimating the values of *s* will be made. The impact on FE from using a suboptimal value of *s* will also be discussed. Finally, by varying the functional form of *s*, the ECMS controller will be improved to make it more robust to changes in the drive cycle. The robust ECMS controller development is first calibrated on the parallel HEV. Subsequently, the same controller will be applied to the power-split model to demonstrate the cross platform applicability of the controller.

2.3.1 Case Study 1 - Parallel HEV

A case study is first conducted on the parallel HEV since it is the simpler of the two HEV architectures. The detailed simulation parameters are listed in Table A.1 of Appendix A. Comparison of the equivalence factor generation methods are made, which demonstrates the inadequacy of simply considering average component efficiency.

Studies of the *SOC* trajectories resulting from sub-optimal equivalence factors then motivate the introduction of the *SOC* based corrections in the equivalence factors.

2.3.1.1 Comparison of s Values Obtained from Different Methods

The estimated *s* values obtained using the methods outlined in Section 2.2.7 are compared for different drive cycles in Figure 2.6. From this figure it is evident that the average-value method of computing *s* consistently overestimates optimal values. On the other hand, considering the marginal cost of using electrical power from Eq. (2.31) yields estimates of *s* that match very well with the values obtained from brute force ECMS optimization. While the optimal *s* value can always be found by brute force optimization, applying the marginal cost method has the advantage of closely estimating the optimal *s* value without the need for lengthy drive cycle iterations.

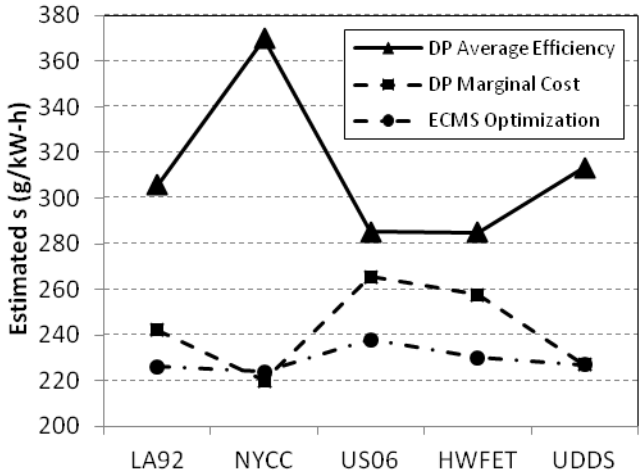

Figure 2.6: Comparison of s values from the three presented estimation methods

2.3.1.2 Implementing SOC Correction in the Equivalence Factors

During the direct optimization of *s* in ECMS, the value of *s* remains constant for each iteration. Using a constant equivalence factor can produce optimal FE as long as the

equivalence factor is tuned properly. Other authors have also suggested a constant *s* value is sufficient [16,19]. Additionally, when the value of *s* is optimized, the constant-*s* ECMS produces a battery *SOC* trajectory that is very similar to that produced by DP, as illustrated by Figure 2.7. This figure depicts the *SOC* trajectories from DP and ECMS during the UDDS drive cycle. The two trajectories bear strong similarities in overall shape. The major difference comes from the high speed phase between 160 sec to 320 sec, where ECMS depletes the battery slightly more than DP. The DP trajectory results in a FE of 27.03 km/L while the ECMS trajectory results in 26.98 km/L. The numbers show little distinction, with ECMS producing 0.18% less FE than DP. This reinforces the idea that ECMS can approximate the globally optimal solution.

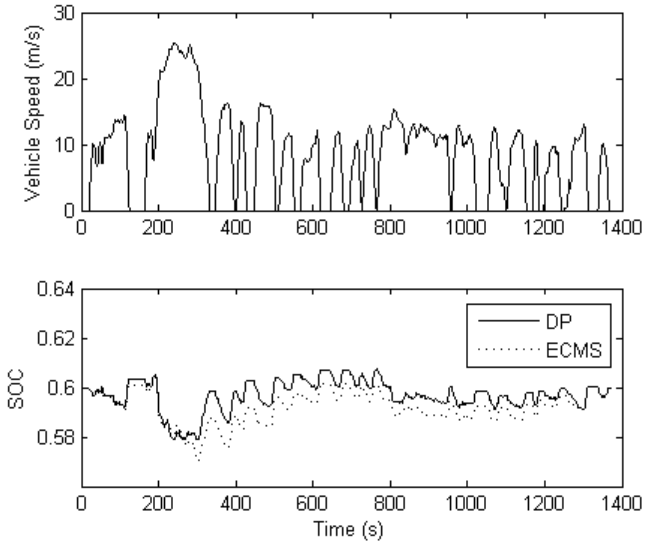

Figure 2.7: Comparison of DP and ECMS *SOC* trajectories using the UDDS drive cycle

While the constant-*s* ECMS can produce FE almost indistinguishable from the DP solution, the optimal value of *s* is drive cycle-dependent as shown in Figure 2.6 (see, for example, the ECMS Optimization results). Even though the obtained values of *s* across

different drive cycles are relatively close, the FE can still be very sensitive to the chosen value. Figure 2.8 illustrates the dependence of FE on the value of *s* using the UDDS drive cycle. The figure documents a sharp peak of FE where the value of *s* is optimal. Note that if a value of *s* that is optimal for the US06 drive cycle is used on the UDDS drive cycle, the predicted FE would have dropped a substantial 6.29% from the maximum in UDDS. Another interesting phenomenon evident in Figure 2.8 is that underestimation of the *s* value incurs less FE penalty than overestimation. This can be explained by noting that one of the major advantages of an HEV is regenerative braking. When the value of *s* is overestimated, battery *SOC* will be sustained near its upper operation limit, and this reduces the opportunities of regenerative braking. On the contrary, when the value of *s* is underestimated, battery *SOC* will be sustained near its lower operation limit, reducing the opportunities for electric machines to assist the engine, but still allowing for regenerative braking whenever necessary.

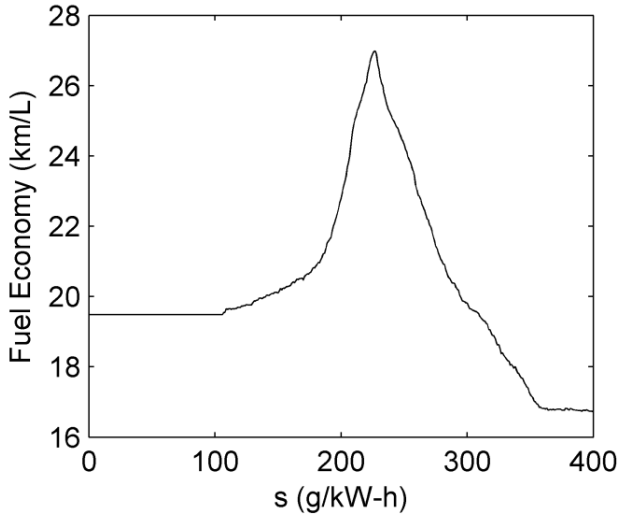

Figure 2.8: Optimization of s for the UDDS drive cycle

The effect of using an suboptimal *s* value can be evaluated further by studying the *SOC* trajectories. Figure 2.9 presents the *SOC* trajectory of the parallel HEV when the value of *s* is set to 275 g/kW-h (the optimal value should be 227 g/kW-h). The overestimation of the *s* value causes the controller to overvalue battery power. This results in underutilization of the battery power such that the *SOC* is sustained near its upper allowable limit. More importantly, this underutilization of the battery heavily penalizes the FE, as evidenced in Figure 2.8.

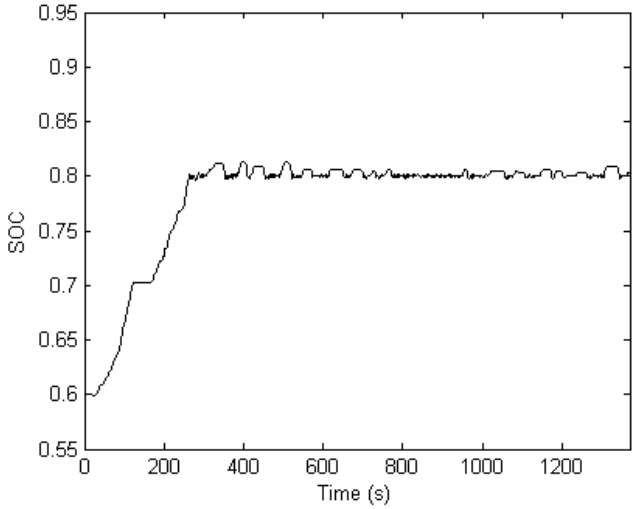

Figure 2.9: *SOC* trajectory using the UDDS drive cycle with overestimated s_{ref}

Since the effect of incorrect estimations of *s* is undesirable *SOC* deviations from the reference value, it is reasonable that a correction in *s* based on *SOC* can mitigate this. This inspires the form of the *s(SOC)* profile described in Eq. (2.33),

$$s(SOC) = s_{ref} - \beta \cdot \tan\left(\frac{\pi}{b + 0.02} * (SOC - SOC_{ref})\right) \tag{2.33}$$

where SOC_{ref} is the reference *SOC* for charging sustaining operation, s_{ref} is the reference value of *s* at the SOC_{ref}, β is the tangent scaling factor and *b* is the width of the SOC

operation range. Note that a small quantity (0.02) has been added to the denominator of the tangent function to avoid singularities at the SOC operating boundaries. The use of the tangent function ensures the *s(SOC)* profile is a smooth function while also ensuring *s(SOC)* increases when the *SOC* is lower than the reference value, thus discouraging battery use, and vice-versa. Figure 2.10 depicts a series of representative $s(SOC)$ curves demonstrating the profiles derived from various values of β. The reference value of *s* can be those values found using the three methods described in Section 2.7. The inclusion of the parameter β allows for tuning of the strength of the *SOC* correction in *s*. A small β allows *s(SOC)* to stay mostly constant until very close to the operation limits of the *SOC* range. This mimics using a constant value for *s(SOC)*. However, subsequent analysis will show that while a small β value can produce the optimal FE figures, it is not necessarily the most robust, and thus further considerations are required to choose an appropriate β.

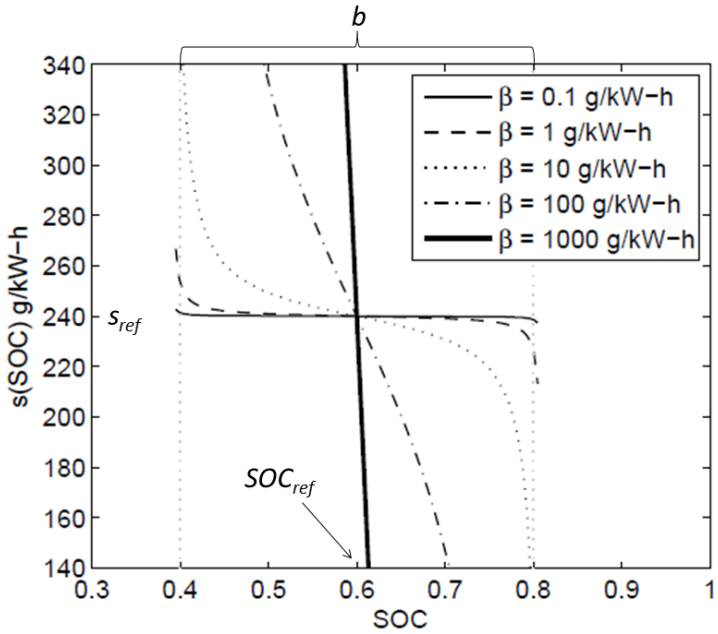

Figure 2.10: Example curves of $s(SOC)$

Figure 2.11 depicts a contour map of iso-FE areas parameterized by s_{ref} and β in ECMS simulations using the UDDS drive cycle. The figure illustrates that an increase in the strength of the *SOC* correction desensitizes the FE figures to the optimality in s_{ref}. The most optimal combinations of the s_{ref} and β are within the darkest red triangular area. When the value of β is sufficiently high, as in the case $\beta = 100$, the FE figures are no longer sensitive to the optimality of s_{ref}. As the value of β increases, there exists a small tradeoff in maximum FE in exchange for more robustness to the effects of sub-optimal values of s_{ref}. Ultimately, the gain in robustness implies the controller will be able to produce near-optimal FE figures under a wide range of driving conditions.

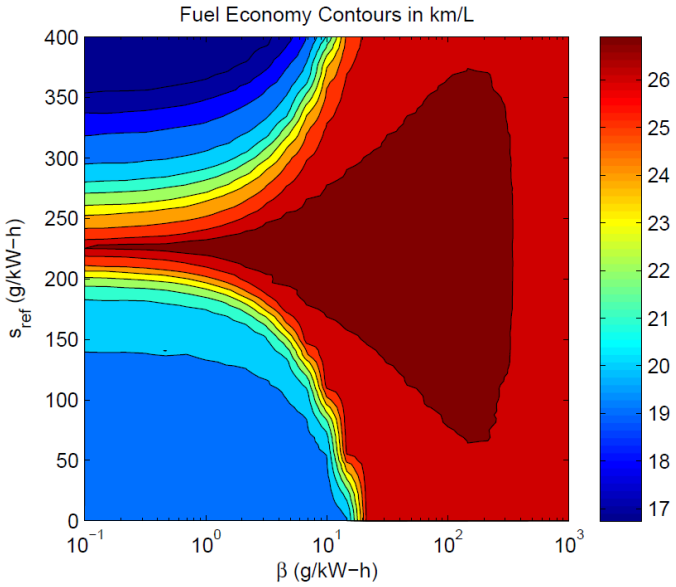

Figure 2.11: Fuel economy contours as a function of s_{ref} and β using the UDDS drive cycle

The effect of having a strong *SOC* correction can be examined by studying the *SOC* trajectories when the value of s_{ref} is over, or under, the optimal value. Figure 2.12 depicts *SOC* trajectories using the UDDS drive cycle with different s_{ref} values, holding the

tangent scaling factor (β) to a value of 100. Although the two trajectories start at the same initial $SOC = 0.6$, they both quickly stabilize about different *SOC* values. The trajectory with s_{ref} = 275 g/kW-h has a mean *SOC* of 0.6585 while the trajectory with s_{ref} = 175 g/kW-h has a mean *SOC* of 0.5448. Using Eq. (2.33), the mean *SOC* of the two trajectories are found to correspond to *s* = 228 g/kW-h and *s* = 219 g/kW-h, respectively. These values are very close to the optimal *s* value of 227 g/kW-h presented in Figure 2.6 for the UDDS cycle using the direct optimization method. This result suggests that by using a strong *SOC* correction in *s*, the *SOC* trajectory of the parallel HEV will have the advantageous tendency to charge sustain around an *SOC* value that corresponds to the optimal *s* value. By extension, this implies that the optimal ECMS operation of an HEV necessitates charge sustaining operation. It is also important to note that since the proposed controller will only use battery *SOC* for state feedback and will not depend on battery power and energy ratings, it can be used in an HEV with battery swapping modularity described in [32].

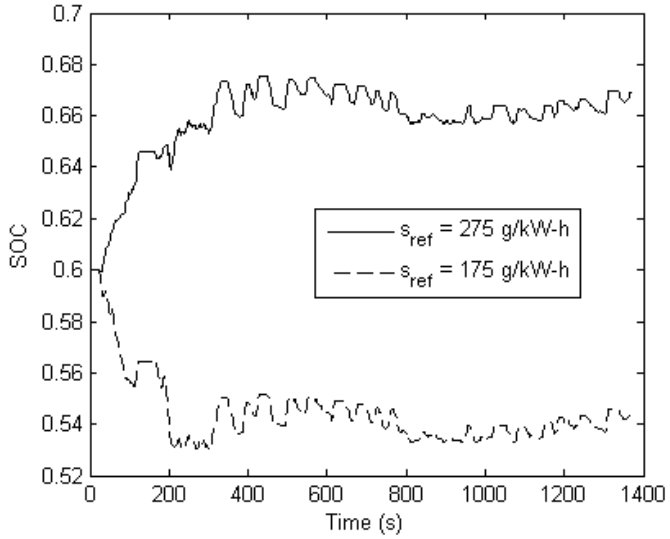

Figure 2.12: *SOC* Trajectories in UDDS Drive Cycle with β = 100 g/kW-h

Insight gained from Figure 2.12 can also be used to define an adaptive controller with further robustness. For a sub-optimal value for s_{ref}, the deviation in the average *SOC* from the reference value can be mitigated by implementing an adaptive law to change the value of s_{ref} on-the-fly in the form of Eq. (2.34),

$$s_{ref,new} = s_{ref} + K_p(SOC_{sma} - SOC_{ref}) \tag{2.34}$$

where SOC_{sma} is the simple moving average of the battery *SOC*, K_p denotes a proportional gain of negative value, and $s_{ref,new}$ the new reference equivalence factor after feedback correction. To test this idea, the adaptive law is executed at every 10 simulation time steps to in order to avoid evoking the high frequency response in the *SOC* trajectory.

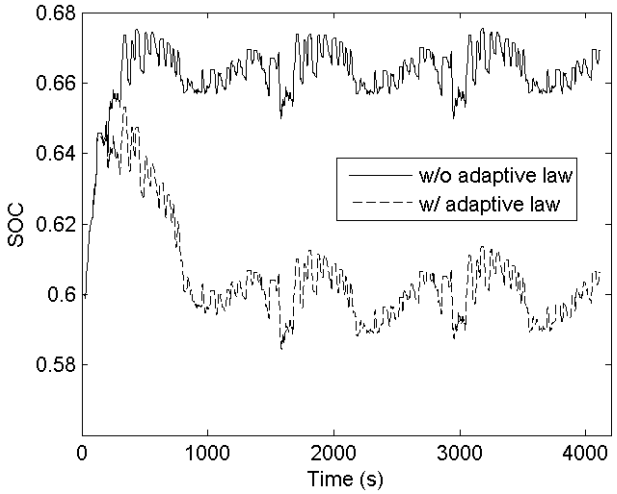

Figure 2.13 *SOC* trajectories in three repetitions of the UDDS drive cycle with β = 100 g/kW-h and s_{ref} = 275 g/kW-h

Using a combined drive cycle composed of three back-to-back UDDS drive cycles, Figure 2.13 demonstrates that the adaptive law is effective in correcting the *SOC* trajectory over a long time period. Over this drive cycle, the ECMS controller with β =

100 g/kW-h and s_{ref} = 275 g/kW-h will produce an *SOC* trajectory that averages an *SOC* of 0.6622. However, after the implementation of the adaptive law to correct the value of s_{ref}, the average *SOC* drops to 0.6061, very close to the reference value of 0.6. Note that the FE increases a non-significant 0.0008% with the adaptive law. Importantly, by staying close to the desired reference value, the adaptive law results in available battery capacity for absorbing large braking events.

While the adaptive law of Eq. (2.34) can force the *SOC* trajectory to average about the reference value specified, it does not adversely affect the fuel economy. Additional simulations (not presented) confirm that fuel economy performance shows the same dependence on the optimality of s_{ref}, and the same tradeoff with the value of β, as the ECMS controller without the adaptive law.

2.3.2 Case Study 2 - Power-split HEV

The power-split HEV model is based on the THS-II system described in Section 2.2.2. The detailed parameters are listed in Table A.2 from Appendix A. In contrast to the parallel architecture, the power-split HEV has the ability to vary engine speed independent of the road speed by the use of a planetary gear set and a second EM. The robust ECMS controller developed from the parallel HEV model will be applied to the power-split HEV model to demonstrate its cross-platform applicability. In this case study, the comparison of the *s* value estimation methods presented in Section 2.2.7 will be made for the power-split architecture. Additionally, the ECMS controller in the form of Eq. (2.33) will be shown to have the same robustness characteristics when applied to the power-split model.

2.3.2.1 Comparison of the Equivalence Factors Obtained from Different Methods

The methods of estimating the functional form of *s* for the parallel HEV apply directly to the power-split HEV since both architectures employ the same state and control variables. Since the power-split HEV architecture has two electric machines, the average efficiency of the two electric machines will be used for estimating *s* when using the average component efficiency method. The estimated *s* values from all three methods discussed earlier are plotted in Figure 2.14 for the power-split HEV.

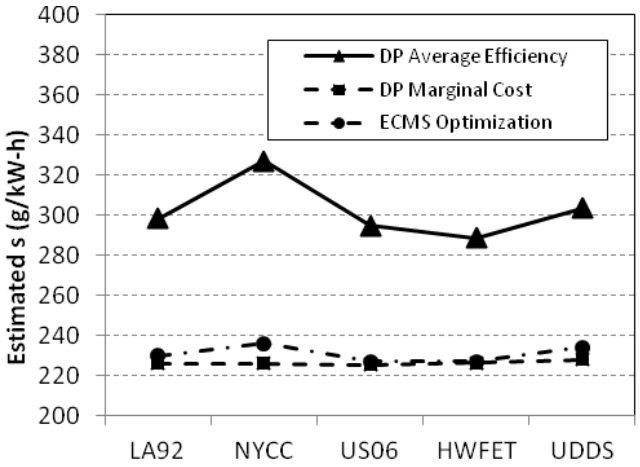

Figure 2.14: Comparison of *s* values from different estimation methods for the power-split HEV architecture

As in the case of the parallel HEV, the average component efficiency method results in overestimations of the optimal *s* value, while the marginal cost method better predicts the optimal value. As in the discussion of the parallel HEV, overestimation of the *s* value will be more detrimental to FE than underestimation if an *SOC* correction in *s* is not implemented. The ECMS optimization of *s* for the UDDS drive cycle demonstrates this point – see Figure 2.15. As Figure 2.15 demonstrates, even more so than in the parallel case, there is a steep drop in FE even if the value of *s* is even weakly overestimated.

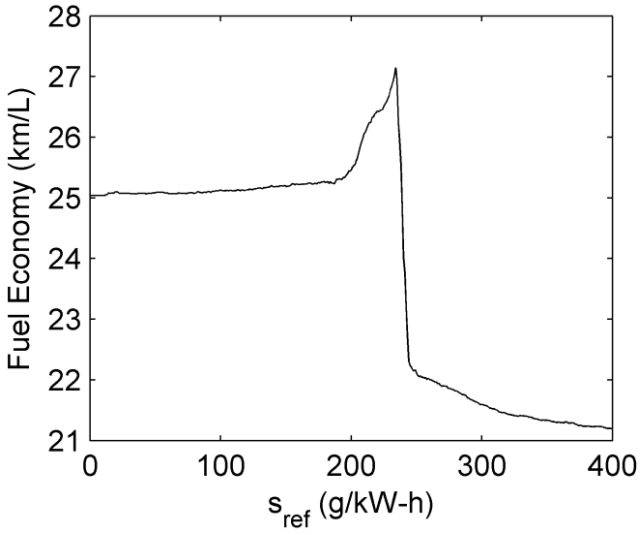

Figure 2.15: ECMS optimization of *s* using the UDDS drive cycle

2.3.2.2 Implementing SOC Correction in the Equivalence Factors

The ECMS controller of the power-split HEV can also be made robust to the variations in *s* by increasing β in Eq. (2.33). Figure 2.16 depicts iso-FE contours using different values of s_{ref} and β in the ECMS controller. The FE numbers of the power-split architecture react to the changes in s_{ref} and β in the same manner as the parallel architecture. The darkest red tear-shape area indicates combinations of s_{ref} and β where the FE is maximized. As the strength of the *SOC* correction in *s* is increased by increasing β, the FE figures become insensitive to the values of the s_{ref}. For example, when $\beta = 10^{-1}$ g/kW-h, the FE can be as low as 21.5 km/L when s_{ref} is not optimized. On the other extreme, if $\beta = 10^{3}$ g/kW-h, the lowest FE will only be about 26.5 km/L when s_{ref} is not optimized. As a tradeoff, the maximum FE is no longer achievable with this β no matter the value of s_{ref}. However, the tradeoff is small - approximately 0.5 km/L for the power-split architecture running the UDDS drive cycle. Since the optimal value of *s*

depends on the drive cycle, the implication of Figure 2.16 is that by choosing a proper value of β, the ECMS controller can achieve near optimal FE in all driving conditions.

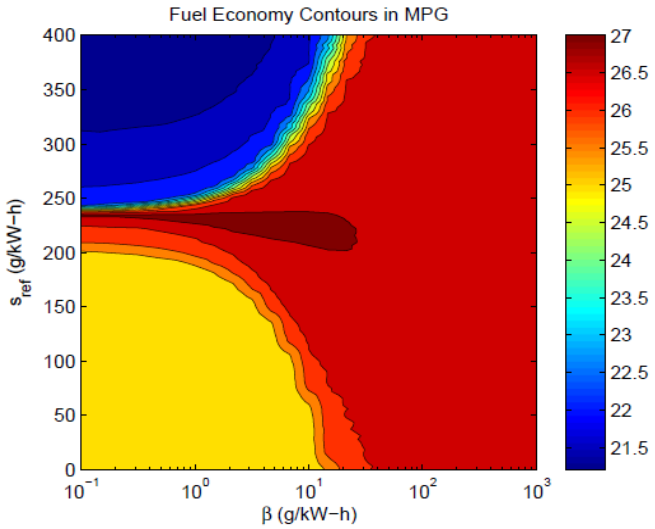

Figure 2.16: Fuel economy contours as a function of s_{ref} and β using the UDDS drive cycle

2.4 Fuel Economy Results for Controller Robustness over Multiple Drive Cycles

In this section the fuel economy numbers for 5 different EPA drive cycles will be presented for the parallel HEV and the power-split HEV using the constant equivalence factor and DP-derived robust ECMS controllers developed earlier. The EPA drive cycles used are LA92, NYCC, US06, HWFET and UDDS, which simulate city with some highway driving, stop and go traffic, high speed aggressive driving, highway driving under 60 MPH (97 km/h), and urban driving, respectively. Both controllers will be optimized first for the UDDS and then for the US06 drive cycle to study the FE performance. This simulates typical controller design compromise. The constant equivalence factor ECMS controller will employ the reference equivalence factor from the brute force optimization method and also from the average efficiency method; the

DP-derived robust ECMS controller will use the reference equivalence factor from the DP marginal cost method and a value of 100 g/kW-h for the tangent scaling factor. Their FE performance will be compared against each other, as well as the DP global optimum, across different drive cycles.

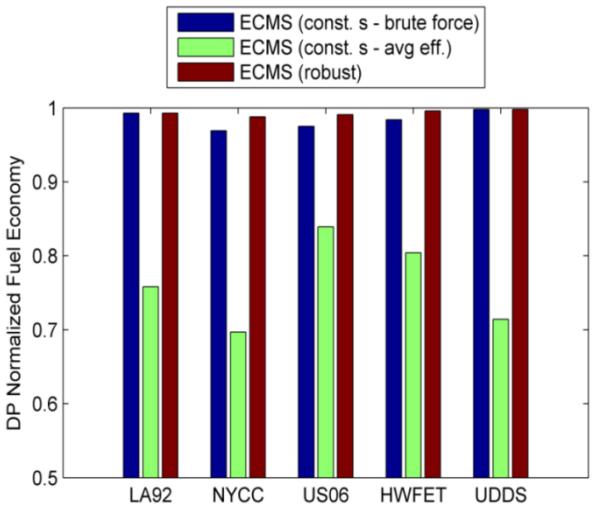

Figure 2.17: DP normalized fuel economy comparison for the parallel HEV with controllers optimized for the UDDS drive cycle

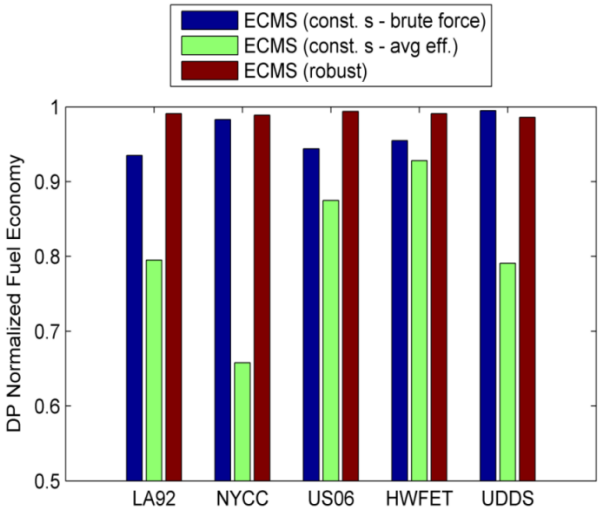

Figure 2.18: DP normalized fuel economy comparison for the power-split HEV with controllers optimized for the UDDS drive cycle

Figure 2.17 documents the FE performance of the three ECMS controllers for the parallel HEV while Figure 2.18 documents that for the power-split HEV, with the controllers optimized for the UDDS drive cycle. All FE numbers are normalized to that of DP for comparison. The complete data set for the UDDS optimized case is attached as Tables A.3 and A.4 in Appendix A. In either architecture, the DP derived robust controller out performs the two constant-*s* controllers. It consistently produces FE that is within 1% of the DP optimum, while the constant-*s* controller with the brute force optimized s_{ref} has FE penalties as much as 3% when compared with the DP optimum in the parallel case and 6% in the power-split case. The average efficiency method regularly overestimates the optimal s_{ref} and has FE penalties in the range of 10-30% in both architectures.

When the ECMS controllers are optimized for the US06 drive cycle, similar FE trends are observed. The data set for the US06 optimized case is also attached for reference as Tables A.5 and A.6 in Appendix A. In this case, the robust controller still consistently produces FE within 1% of the DP optimum. However, the performance of the constant-*s* controller with the brute force optimized s_{ref} is reversed between the two architectures. It produces as much as 8% less than the DP optimum in the parallel architecture, but only as much as 3% less in the power-split case. The robust controller handles cross drive cycle variability much better than the constant-*s* controller regardless of architectures or the drive cycle for which it has been optimized. It should be also noted that since the direct optimization method requires assumptions of exact specifications of the powertrains, it will not be able to handle uncertainties such as

manufacturing variance and component aging that may cause the optimal value of the equivalence factor to shift.

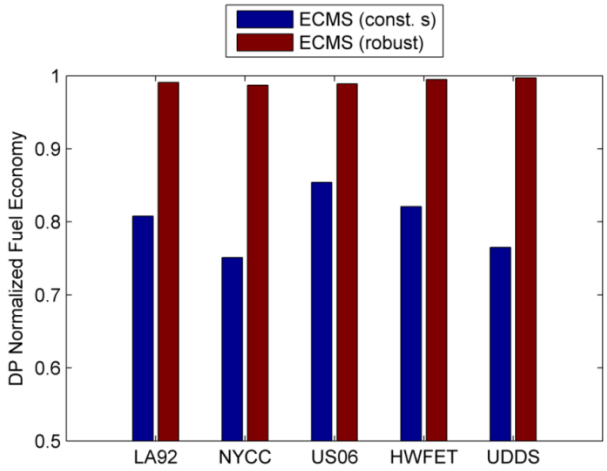

Figure 2.19: DP normalized fuel economy comparison for the parallel HEV with extreme range of s_{ref}

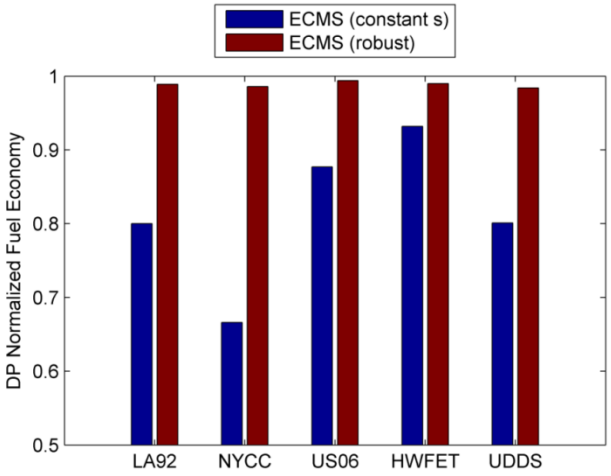

Figure 2.20: DP normalized fuel economy comparison for the power-split HEV with extreme range of s_{ref}

To further assess the robustness of the DP derived robust controller, the values of s_{ref} are varied from 175 to 275 g/kW-h to simulate extreme mismatch of the driving condition with the equivalence factor. The minimum values of FE obtained over this large range of

s_{ref} are then compared for the constant-*s* and the robust ECMS controllers. The dynamic programming FE is also presented for comparison purposes.

Figure 2.19 provides the predicted FE for the parallel HEV while Figure 2.20 shows the predicted FE for the power-split HEV. The complete data set is attached as Tables A.7 and A.8 in Appendix A. When s_{ref} is not optimal for the drive cycle, the FE penalty can be as high as 20-30% compared to DP. On the other hand, the robust ECMS controller produces much more consistent FE, within 1-2% of DP, regardless of the variations in the reference equivalence factor. Thus the robust ECMS controller incurs an insignificant penalty on maximum FE in exchange for a large gain in robustness. Not that in real world situations, shifts of the optimal equivalence factor can arise from component variance (due to environmental conditions, aging, etc.) and deviations from standard drive cycles. Since the constant-*s* controller shows such a large FE penalty with respect to equivalence factor mismatch, its potential for online application remains poor. On the other hand, the robust controller performs much better in this respect and is a promising candidate for real world applications.

2.5 Summary

This chapter has presented a rational approach for informing the equivalent cost factor in ECMS control strategies using dynamic programming and marginal cost. Two existing methods of estimating the equivalence factor are compared to the presented approach. It is found that using the marginal cost method with dynamic programming data results in an estimated equivalence factor closely matching that obtained from the brute force method of iterative simulations. Fuel economy and *SOC* time history data demonstrate that ECMS can be implemented with a constant equivalence factor to

achieve near globally optimal FE performance. However, the resulting FE exhibits high sensitivity with respect to the equivalence factor. Poor FE stems from undesirable *SOC* deviations away from its reference value. This necessitates a method for increasing the robustness of the ECMS controller. The dynamic programming-informed equivalence factor is used as a reference value at the desired charge sustaining *SOC* and a correction term based on the battery *SOC* is used to adjust the reference equivalence factor. Strong *SOC* correction is shown to desensitize the FE to the optimality of the reference equivalence factor, but still produces some *SOC* deviation. To further improve the *SOC* trajectory deviation, an adaptive law is added and it is shown to effectively sustain the *SOC* at the reference value. Finally, FE figures are compared for a constant equivalence factor ECMS controller and a robust one. The robust controller is shown to produce FE that is consistently within 1% of the global optimum prescribed by dynamic programming across five different drive cycles regardless of the drive cycle the controller is optimized for. Even when reference equivalence factor deviates substantially from the optimal value, the robust controller still produces excellent FE that is within 1-2% of DP. In contrast, the constant equivalence factor can suffer FE penalties as high as 20-30% in similar situations. In conclusion, the proposed robust controller should produce near optimal FE, even in the presence of powertrain component variance and drive cycle deviations.

CHAPTER 3

FORWARD-LOOKING SIMULATION OF THE GM FRONT-WHEEL DRIVE TWO-MODE POWER-SPLIT HEV USING DYNAMIC PROGRAMMING-INFORMED EQUIVALENT COST MINIMIZATION STRATEGIES

3.1 Introduction

This chapter presents a forward-looking simulation (FLS) approach of implementing the dynamic programming (DP)-informed Equivalent Cost Minimization Strategy (ECMS) developed in Chapter 2. The goal is to address the inadequacies of using backward-looking simulations (BLS) for control strategy verification. Implementation of the DP-informed ECMS will demonstrate its potential for online applications.

The architecture chosen for study is the front wheel drive (FWD) General Motors Allison Hybrid System II (GM AHS-II), which is a type of power-split architecture. As described in Chapter 1 and 2, power-split HEVs combine the features of the series and parallel architectures by using two EMs with planetary gear sets (PG) to realize a Electrically Variable Transmission (EVT) with the gear ratio varied by one EM, while the other EM provides extra traction torque. The most prominent example of this architecture is the Toyota Hybrid System II (THS-II), which is detailed in Chapter 2. While the THS-II powertrain has one EVT mode that is optimized for city driving, its highway performance suffers due to the excessive power circulation loops at high speed driving [29]. On the other hand, General Motors developed a 2-mode EVT, the Allison Hybrid System II (AHS-II). The front-wheel drive (FWD) version of the 2-mode EVT

utilizes two planetary gear sets and four clutches to realize two power-split modes as well as four fixed gear modes [33,34]. The incorporation of two EVT modes allows optimization for both low speed and high speed driving, as well as reducing the power requirement of the electric machines [35]. However, Arata *et. al.* found that, with similar power plant parameters, the THS-II and AHS-II powertrains perform similarly in terms of fuel economy (FE) [8].

Chapter 2 developed a robust ECMS controller with excellent robustness against drive cycle and component variations. Its fuel economy performance is near the global optimal solution. The efficacy of the controller is verified with backward-looking simulations (BLS) on parallel and THS-II power-split architectures. Backward-looking simulations assume perfect cycle tracking and use the steady state energy or torque balance compute component operation states. It is widely used in literature for efficient control strategy verification and architecture comparison [8,11,20]. However, backward-looking simulations often neglect fast component transients and do not accurately represent the causality relationship in an actual vehicle, therefore they do not provide enough insight into the control strategy's viability for online implementation.

This chapter addresses these inadequacies by performing forward-looking simulations on the GM AHS-II power-split architecture using the robust ECMS controller developed in the previous chapter. This will further verify the cross platform applicability of the robust ECMS controller on a complex powertrain. Forward-looking simulations closely mimic the command structure of an actual vehicle in which a driver command ultimately results in a torque output at the wheel. Component dynamics are simulated in FLS, and the effects of component transients on FE will be analyzed. The FLS controller uses

component operation lookup maps generated by the backward-looking model. The effectiveness of this approach will also be discussed. This chapter will also give insight into the online implementation of an optimization based controller on the GM AHS-II architecture, and demonstrate the efficacy of the robust ECMS controller.

The organization of the chapter is as follows: first an overview of the GM FWD 2-mode architecture will be presented. The backward-looking simulation approaches and the application of the backward-looking simulation results to the forward-looking simulation will then be described. Finally, simulation results from both the BLS and the FLS models will be compared.

3.2 GM AHS-II Architecture Overview

In this section, an overview of the GM AHS-II architecture will be given. Operation and kinematics of the two EVT modes will be discussed. This establishes the steady-state constraints used in the backward-looking simulations.

3.2.1 Operations of the Planetary Gear Sets

The heart of the GM AHS-II architecture is two planetary gear sets. Unlike in the THS-II architecture where only one simple planetary is used, the GM AHS-II architecture uses two planetary gear sets – one simple and one compound. Figure 3.1 depicts the simple planetary while Figure 3.2 shows the compound planetary. The simple planetary found in GM AHS-II is identical in function to the simple planetary found in the THS-II power-split architecture, discussed in details in Chapter 2. The structure of the compound planetary is similar to that of a simple planetary, except the three pinion gears are replaced by three sets of two coupled pinion gears. A carrier arm also joins the three sets of pinion gears and rotates about the same axis as the ring and the sun gears.

Compare to the simple planetary, the key difference in the compound planetary gear is that the direction of rotation of the ring gear reverses.

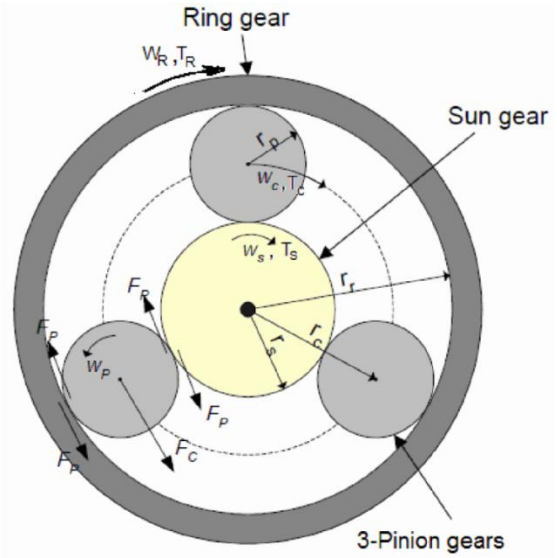

Figure 3.1: Simple planetary gear set, reproduced from [33]

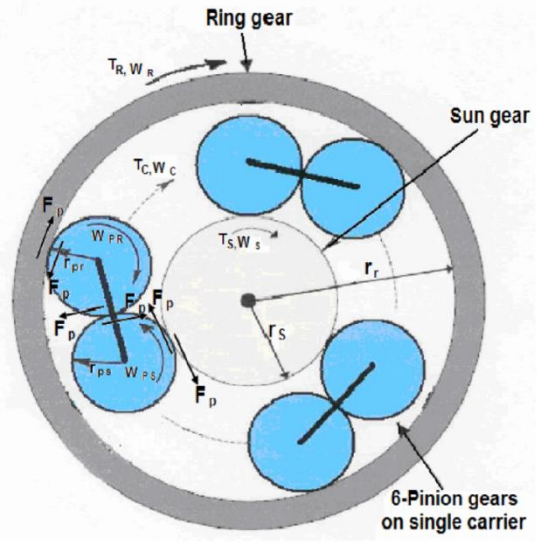

Figure 3.2: Compound planetary gear set, reproduced from [33]

Figure 3.3 depicts a schematic of the FWD GM AHS-II architecture and its use of the planetary gear sets. The planetary PG1 is the compound planetary while PG2 is the simple planetary. The letters R, C, and S denote the ring, carrier and sun connection ports on a planetary gear set, while a succeeding number represents the respective planetary gear set. The two planetary gear sets and four clutches (CL) enable different modes of operation. The powertrain uses an IC engine and two electric machines (denoted as EM) as power plants.

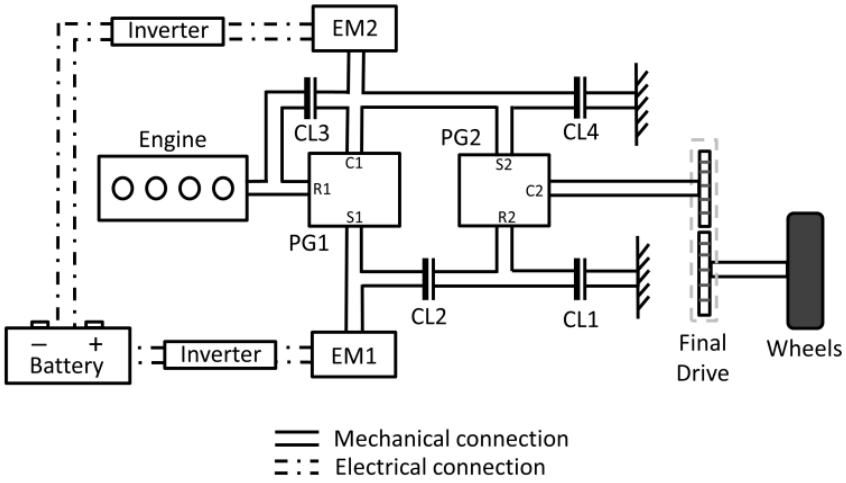

Figure 3.3: Schematic of the GM AHS-II architecture

Each planetary gear set has a characteristic ratio ρ defined as the tooth-number of the sun gear to the tooth-number on the ring gear. Reference [33] provides the steady-state angular velocity and torque relationships for both planetary gear sets. The results will be summarized here. In essence, by assuming equal velocities at the contact points, the steady-state angular velocity relationships of the planetary gear sets become,

$$(1-\rho_1)\omega_{C1} + \rho_1\omega_{S1} - \omega_{R1} = 0 \tag{3.1}$$

$$(1+\rho_2)\omega_{C2} - \rho_2\omega_{S2} - \omega_{R2} = 0 \tag{3.2}$$

where ω denotes angular velocity. Note the differences in signs of the two equations as they are for two different planetary gear types. The steady state torque relationships come from neglecting gear acceleration and performing an energy balance on a gear set, resulting in,

$$T_{R1} = -\frac{1}{\rho_1}T_{S1} = -\frac{1}{1-\rho_1}T_{C1} \tag{3.3}$$

$$T_{R2} = \frac{1}{\rho_2}T_{S2} = -\frac{1}{1+\rho_2}T_{C2} \tag{3.4}$$

In the AHS-II architecture, connection ports C1 and S2 on the two planetary gear sets are always rigidly connected. Port C2 is always connected to the final drive and its torque and angular velocity are essentially the outputs of the EVT. Different modes of operations are enabled by engagements of different combinations of the clutches of the powertrain. The EVT-1 mode is activated by engaging only CL1, which grounds the R2 port to the frame of the vehicle. On the other hand, the EVT-2 mode is activated by engaging only CL2, which connect port S1 and port R2.

In addition to the EVT modes, there are four fixed gear (FG) modes, made possible by engagements of two clutches at the same time. The fixed gear modes enable power transmission characteristics similar to that of a conventional discrete gear transmission. Furthermore, FG-2 mode uses both CL1 and CL2, and serves as the transition between the two EVT modes. This guarantees the transitions between the two EVT modes occur only when the angular velocity of the EM1 is zero. Table 3.1 shows the modes of operation and the required clutch engagements. Notice each fixed gear mode uses at least one of the clutches already utilized by either EVT-1 or EVT-2 mode. The FG modes can

be treated as subsets of the EVT modes with additional kinematic constraints. For this reason, the Fuel Economy simulations for AHS-II are done with only the EVT modes.

Table 3.1: Clutch engagements for different operation modes

	CL1	CL2	CL3	CL4
EVT-1	X			
EVT-2		X		
FG-1	X		X	
FG-2	X	X		
FG-3		X	X	
FG-4		X		X

3.2.2 EVT-1 Kinematics

In EVT-1 mode, only CL1 engages and the powertrain is in input split mode. Engine power splits at PG1, while PG2 acts as a simple gear reduction. Figure 3.4 shows the GM AHS-II architecture in EVT-1 mode and its mechanical and electrical connections. Engine connects to the ring gear of PG1 while EM1 connects to the sun gear of PG1. Electric Machine 2 connects to both the carrier arm of PG1 and the sun gear of PG2. Finally the carrier arm of PG2 acts as the output of the EVT and drives the wheels. In this mode, EM1 acts primarily as a generator and stores energy in the battery while EM2 acts primarily as a motor and injects energy into PG1 [8]. The constraints between the two planetary gear sets are $\omega_{C1} = \omega_{S2}$, $T_{C1} = T_{S2}$, and $\omega_{R2} = 0$. The resultant steady-state torque and angular velocity relationships in the powertrain are,

$$\omega_{EM1} = \frac{1}{\rho_1}\omega_e - \frac{(1-\rho_1)(1+\rho_2)}{\rho_1\rho_2}\omega_{\mathrm{C2}} \tag{3.5}$$

$$\omega_{EM2} = \frac{1+\rho_2}{\rho_2}\omega_{\mathrm{C2}} \tag{3.6}$$

$$T_{EM1} = -\rho_1 T_e \tag{3.7}$$

$$T_{EM2} = -(1-\rho_1)T_e + \frac{\rho_2}{1+\rho_2} T_{C2} \tag{3.8}$$

where the subscript *e* denotes the engine.

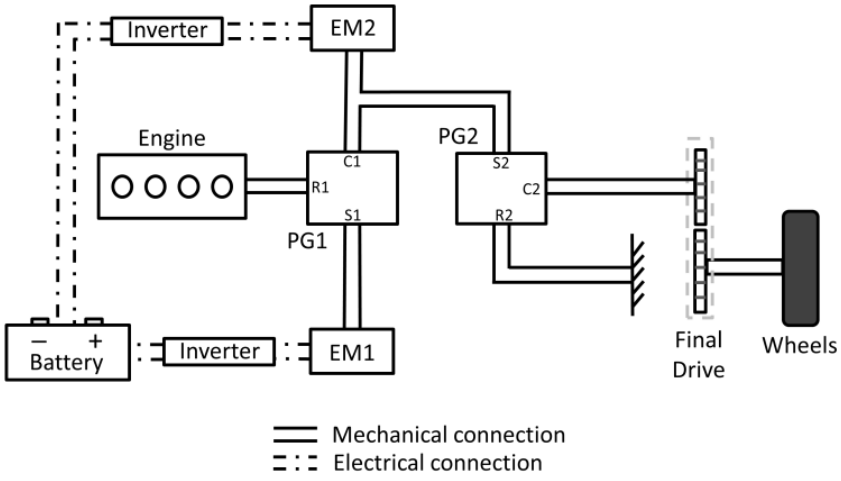

Figure 3.4: Schematic of the GM AHS-II architecture in EVT-1 mode

3.2.3 EVT-2 Kinematics

In EVT-2 mode, only CL2 engages and the powertrain is in compound split mode. Engine power splits at PG1 and recombines with EM1 and EM2 power at PG2. Figure 3.5 depicts the GM AHS-II architecture in EVT-2 mode and its mechanical and electrical connections. The engine still only connects the ring gear of PG1. However, both EMs are now mechanically linked to both planetary gear sets. Electric machine 1 connects to the sun gear of PG1 and the ring gear PG2; electric machine 2 still retains the same mechanical connections as those in EVT-1 mode. The roles of the electric machines are reversed: EM-1 acts primarily as a motor while EM-2 acts primarily as a generator [8]. The constraints between the two planetary gear sets are $\omega_{C1} = \omega_{S2}, T_{C1} = T_{S2}, \omega_{S1} =$

ω_{R2}, and $T_{S1} = T_{R2}$. The resultant steady-state torque and angular velocity relationships in the powertrain are,

$$\omega_{EM1} = -\frac{\rho_2}{1-\rho_1-\rho_1\rho_2}\omega_e + \frac{(1-\rho_1)(1+\rho_2)}{1-\rho_1-\rho_1\rho_2}\omega_{C2} \tag{3.9}$$

$$\omega_{EM2} = \frac{1}{1-\rho_1-\rho_1\rho_2}\omega_e - \frac{1-\rho_1(1+\rho_2)}{1-\rho_1-\rho_1\rho_2}\omega_{C2} \tag{3.10}$$

$$T_{EM1} = -\rho_1 T_e + \frac{\rho_2}{1+\rho_2}T_{C2} \tag{3.11}$$

$$T_{EM2} = -(1-\rho_1)T_e + \frac{\rho_2}{1+\rho_2}T_{C2} \tag{3.12}$$

Compared to EVT-1, EVT-2 mode allows lower engine speeds and avoids power circulation loops in the electrical path at high vehicle speeds. This helps the engine operate near its most efficient point and maintain overall efficient power transmission through the EVT.

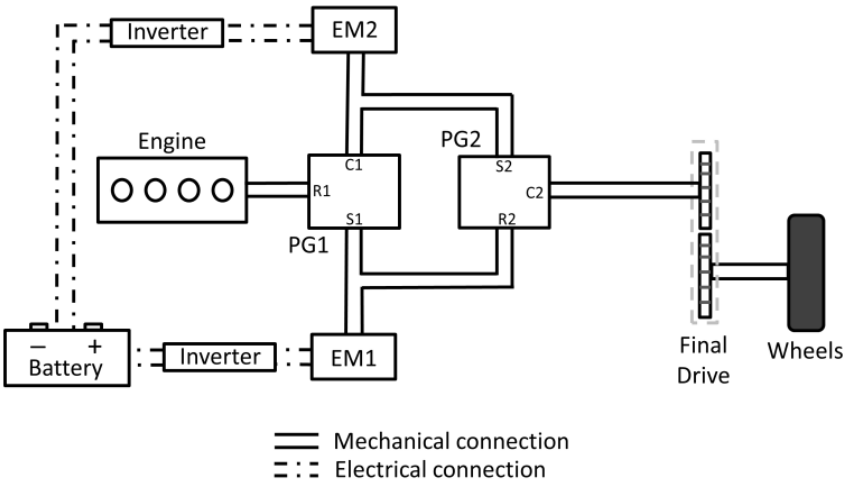

Figure 3.5: Schematic of the GM AHS-II architecture in EVT-2 mode

3.3 Backward-looking Simulations

The backward-looking simulations for the GM AHS-II are implemented in the same fashion as the previous chapter for the parallel and the THS-II power-split architectures. This section will reiterate a few key points. It will then develop the robust ECMS controller described in Chapter 2 as applied to the GM AHS-II architecture. Finally, dynamic programming results will inform the parameter decision of the robust ECMS controller.

3.3.1 GM AHS-II Vehicle Operation Overview

A backward-looking simulation is conducted with the specification of a drive cycle and the assumption that the drive cycle is followed exactly. The vehicle velocity specified by the drive cycle leads to the definition of force required at the wheel,

$$F_{req} = \frac{T_w}{r_w} = f_r Mg + \frac{1}{2}\rho_{air} C_d A_f v^2 + \delta Ma \tag{3.13}$$

where T_w and r_w denote the torque at the wheel and the tire radius, respectively, f_r denotes the rolling resistance factor, ρ_{air} the density of air, C_d the drag coefficient, A_f the vehicle frontal area, v vehicle velocity, a the vehicle acceleration, M the mass of the vehicle and δ the mass factor. In BLS, a first-order finite difference representation (*i.e.*, $\Delta v/\Delta t$) is taken for the acceleration. This leads to the following required angular velocity and torque at the EVT output,

$$\omega_{C2} = \frac{v i_f}{r} \tag{3.14}$$

$$T_{C2} = \frac{F_{req} r_w}{i_f} \tag{3.15}$$

where i_f denotes the final drive gear ratio. Since ω_{C2} and T_{C2} are specified directly from the drive cycle, combined with the steady-state constraints from Eq. (3.5) – (3.12), only one torque and one speed are needed to fully specify the system operation states. In this case, engine torque and speed are used as control inputs while the torques and speeds of the EMs can be calculated from Eq. (3.5) – (3.12). The fuel rate of the engine is found from a brake specific fuel consumption (BSFC) map. The battery power is calculated as the following.

$$P_{bat} = T_{EM1}\omega_{EM1}\eta_{EM1}^{-sgn(T_{EM1}\omega_{EM1})} + T_{EM2}\omega_{EM2}\eta_{EM2}^{-sgn(T_{EM2}\omega_{EM2})} \tag{3.16}$$

The combined inverter and EM efficiencies η_{EM1} and η_{EM2} come from efficiency maps. The sign convention is such that positive battery power depletes the battery. The efficiency terms have different definitions depending on the direction of power flow. The signum function in the exponents of the efficiency terms addresses this. The battery state of charge (*SOC*) operation range is chosen to be between 0.4 and 0.8, in which battery internal resistance remains fairly constant [16]. Therefore, the battery is modeled as a constant voltage source. The battery *SOC* will be the only independent state of the system. Table B.1 in Appendix B details the simulation parameters for the GM AHS-II architecture.

3.3.2 Overview of Dynamic Programming for GM AHS-II

This section will detail the application of dynamic programming to the GM AHS-II architecture. As introduced in Chapter 2, dynamic programming solves discrete-time models that can be expressed in the following form,

$$\boldsymbol{x}_{k+1} = \boldsymbol{F}_k(\boldsymbol{x}_k, \boldsymbol{u}_k), \quad k = [0, N-1] \tag{3.17}$$

where k denotes the index of discretized time, $\boldsymbol{x}_k$ the state variable, $\boldsymbol{u}_k$ the control variable, and $\boldsymbol{F}_k$ the function defining the state transition. The goal is to find the optimal trajectory through a discretized state-time space, which is a space parameterized by the independent states and time.

When applied to the GM AHS-II architecture, the DP problem is to minimize the following cost at each point in the state-time space,

$$J_k\left(SOC_k^i\right) = \min\left[J_{k+1}\left(SOC_{k+1}^i\right) + \dot{m}_{fuel}(T_e, \omega_e) + \phi_k(SOC_n, T_e, \omega_e)\right] \quad (3.18)$$

where, J_k is the cost to go, SOC_k^i is the discretized state-time point indexed by state index i and time index k, $\dot{m}_{fuel}$ is the fuel consumption rate, and ϕ_k is the constraint violation cost. The constraints are summarized in Eq. (3.19).

$$\text{GM 2-mode power-split HEV: constraints} \begin{cases} T_{e,min} \le T_e \le T_{e,max} \\ \omega_{e,min} \le \omega_e \le \omega_{e,max} \\ T_{EM1,min} \le T_{EM1} \le T_{EM1,max} \\ \omega_{EM1,min} \le \omega_{EM1} \le \omega_{EM1,max} \\ T_{EM2,min} \le T_{EM2} \le T_{EM2,max} \\ \omega_{EM2,min} \le \omega_{EM2} \le \omega_{EM2,max} \\ SOC_{min} \le SOC \le SOC_{max} \\ SOC_0 = SOC_N = SOC_{ref} \end{cases} \quad (3.19)$$

A violation of any of the constraint will incur a constraint violation cost ϕ_k that is several orders of magnitude greater than $\dot{m}_{fuel}(T_e, \omega_e)$, which essentially ensures the constraints are always satisfied. The minimization of Eq. (3.18) is performed backward in time at every point of the state-time space while keeping track of the next time step state (SOC_{k+1}^i) and controls applied (T_e, ω_e). By selecting the starting point that has the minimal cost, the optimal control policy and the state trajectory can be recovered in a forward fashion. The process is not causal, as it uses future operation knowledge, but it will result in a globally minimum fuel consumption rate over a drive cycle. The results

from dynamic programming are used here as the controller performance benchmark and to inform the robust ECMS controller.

3.3.3 Overview of Robust ECMS for GM AHS-II

In contrast to dynamic programming, the Equivalent Cost Minimization Strategy minimizes the following cost at each time step,

$$C = \dot{m}_{fuel} + s \cdot P_{bat} + \phi_k(*) \tag{3.20}$$

where *s* is the equivalence factor to convert battery power to an equivalent amount of fuel usage. The tuning of the equivalence factor affects the FE performance and is drive cycle-specific as discussed in Chapter 2.

Chapter 2 demonstrates that both DP and ECMS uses Pareto-optimal pairs for ($\dot{m}_{fuel}$, P_{bat}); that is, one quantity is always minimized given the other. Under this consideration, the fuel rate in dynamic programing can be parameterized by the battery power as $\dot{m}_{fuel}^{DP}(P_{bat})$. Assuming the dynamic programming operation also minimizes the cost in ECMS and that no constraint is violated, the following conditions must be satisfied.

$$\frac{dC}{dP_{bat}} = \frac{d\dot{m}_{fuel}^{DP}(P_{bat})}{dP_{bat}} + s = 0 \tag{3.21}$$

$$\frac{d^2C}{d(P_{bat})^2} = \frac{d^2\dot{m}_{fuel}^{DP}(P_{bat})}{d(P_{bat})^2} > 0 \tag{3.22}$$

Equation (3.21) provides a DP-informed *s* value for ECMS operation. This definition of *s* can be considered a marginal cost of using the electrical power. Averaging the *s* found using Eq. (3.21) over a drive cycle will result in an equivalence factor that is very close to the optimal value for the drive cycle.

The same *SOC* based functional form of the equivalence factor is taken from Chapter 2,

$$(SOC) = s_{ref} - \beta \cdot \tan\left(\frac{\pi}{b + 0.02} * (SOC - SOC_{ref})\right) \quad (3.23)$$

where SOC_{ref} is the reference *SOC* for charging sustaining operation, s_{ref} is the reference value of *s* at the SOC_{ref}, β is the tangent scaling factor and *b* is the width of the SOC operation range. The value of s_{ref} will be the equivalence factor found using the aforementioned DP-informed method for a standard Environment Protection Agency drive cycle, such as Urban Dynamometer Driving Schedule (UDDS). The use of the tangent function ensures the *s(SOC)* profile is a smooth function while also ensuring *s(SOC)* increases when the *SOC* is lower than the reference value, thus discouraging battery use, and vice-versa. In Chapter 2, this functional form of *s(SOC)* is show to have excellent robustness with correct specification of the tangent scaling factor β.

3.4 Forward-looking Simulations

This section describes the FLS model of the GM AHS-II architecture. Component modeling will be described and implementing the robust ECMS controller in FLS will be detailed. Simulation parameters are listed in Table B.1 in Appendix B.

3.4.1 System Model

The forward-looking simulations are implemented with Simulink. The highest level of the vehicle model consists of three subsystems: driver, plant, and controller as shown in Figure 3.6. The communication between the three main subsystems emulates that in a vehicle CAN bus.

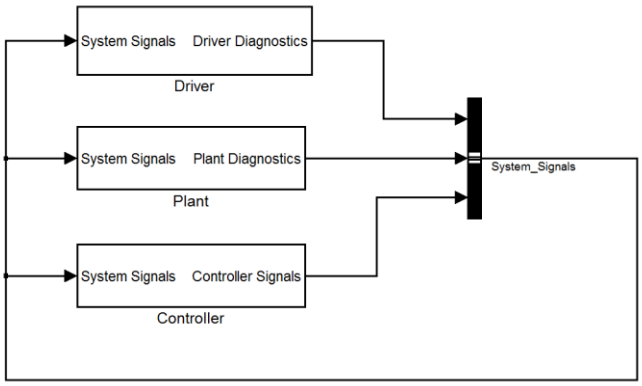

Figure 3.6: High level system modeling

3.4.2 Driver Model

The driver model uses a PID controller to accomplish speed tracking of the vehicle. The tracking error between the vehicle speed and drive cycle specified speed is converted to acceleration and braking requests. These requests are processed by the controller and result in torque demands at various vehicle components.

3.4.3 Plant Model

The plant model encompasses all the physical components of the vehicles. The component schematic is shown in Figure 3.7. Engine and EMs are modeled as torque actuators producing a requested torque. Their torque capabilities are provided by component datasheets. Engine fuel rate and EM power usage are computed using BSFC and efficiency maps. In situations where speed tracking of a power plant is required, PID controllers are employed to convert tracking errors into torque requests. The EVT is comprised primarily of direct gearings with efficiency close to unity, thus no efficiency loss is modeled in the EVT except clutch slippage during EVT mode transitions. The

Battery is modeled as a constant voltage source with the assumption of constant internal resistance within the narrow operation range.

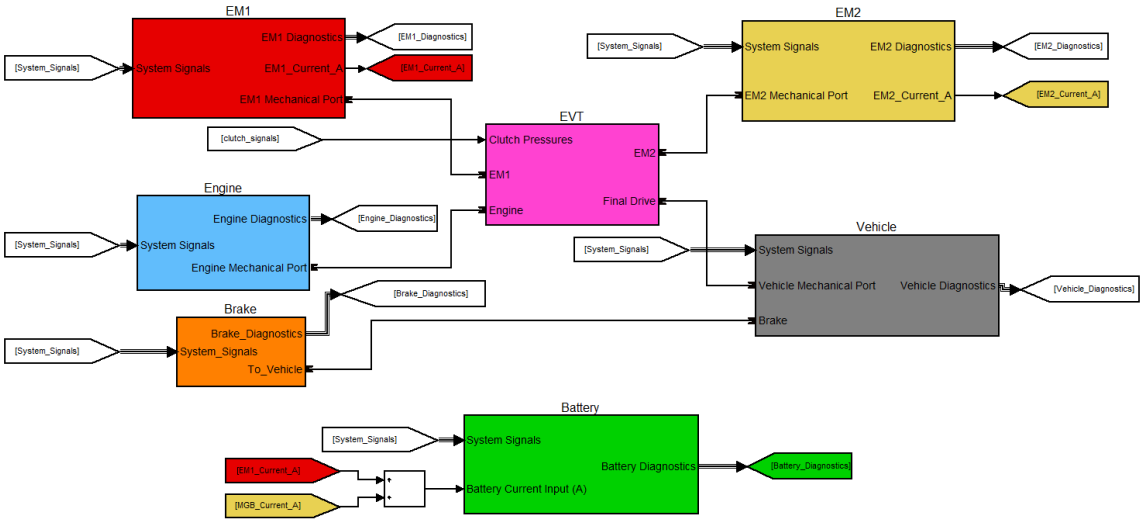

Figure 3.7: Vehicle components schematic

In forward-looking simulations, instead of assuming quasi-static operation, the moment balance equation is applied to each rotating component (*e.g.*, engine, electric machine, gears, etc.). While the vehicle longitudinal dynamics presented in Eq. (3.13) for BLS still applies, it is converted to rotational dynamics of an equivalent inertia and opposing torques on the drive shaft in the following form,

$$T_{C2} i_f - \left(f_r mg + \frac{1}{2} \rho_{air} C_d A v^2 \right) r_w = (m r_w^2) \alpha_w \tag{3.24}$$

where α_w is the angular acceleration of the wheel and $m r_w^2$ becomes the effective inertia on the driveshaft. Multiplication of wheel angular acceleration α_w with wheel radius produces vehicle acceleration, the integration of which yields vehicle velocity.

3.4.4 Controller Model

The controller model uses off-line generated lookup tables similar to that proposed in [36]. Component operating states are computed using the steady-state speed and torque equations for a range of vehicle speed, force required at the wheel and battery *SOC* (v, F_{req}, SOC). The components are operated according to the lookup values during FLS. The approach detailed in [36] is for a THS-II power-split architecture with only one EVT mode; additional considerations have to be made for the GM AHS-II architecture.

The AHS-II EVT employs primarily direct gearings. Assuming no slippage or backlash in the gearings, the angular velocity relationships (Eqs. (3.5), (3.6), (3.9) and (3.10)) still apply in FLS, except for during the brief moment of an EVT mode transition. There are four angular velocities of interest, but only two constraints in a given EVT mode. However, the EVT output speed ω_{C2} is directly coupled with the wheel speed and effectively controlled by the driver. Therefore only one angular velocity quantity is directly controlled during FLS. The controlled angular velocity is ω_{EM1} in EVT-1 and ω_{EM2} in EVT-2; the decision is based on the primary function (*i.e.* generating or motoring) of the EMs.

There exist also four torques of interest in FLS. However, the two steady-state constraints do not apply in general since all rotation components are modeled with finite moments of inertia in FLS. Nevertheless, the FLS controller still assumes steady-state operation and lets the driver speed tracking model compensate for the difference in output torque at the wheels. Two torque quantities will be directly controlled in FLS under this assumption. The engine torque output (T_e) is always controlled and a different EM torque output (T_{EM2} in EVT-1 and T_{EM1} in EVT-2) is controlled based on the EVT

mode. The choice of controlled EM torque is also based on the primary function of the EMs.

In summary, a total of one angular velocity and two torque quantities will be controlled during FLS. The controlled quantities are $(T_e, \omega_{EM1}, T_{EM2})$ for EVT-1 mode and $(T_e, T_{EM1}, \omega_{EM2})$ for EVT-2 mode and they are chosen based on the primary roles of the EMs. In EVT-1 mode, EM1 acts primarily as a generator while EM2 acts primarily as a motor, thus the angular velocity of EM1 is controlled while the torque of EM2 is controlled in EVT-1. Their primary roles reverse in EVT-2 and so do the controlled states. Mode switch decisions are handled with a preferred EVT mode lookup map. If the current EVT mode is different from that preferred, the controller will attempt to switch EVT mode. However, an EVT mode change will only be executed if ω_{EM1} is within 200 RPM and 2 seconds have elapsed since the last mode changes. The first condition reduces component state transients between EVT modes while the second condition reduces excessive mode changes. Figure 3.8 presents a flow chart of the controller decision process discussed here. The control decision process is carried out at rate of 10 Hz since no additional benefit to fuel economy is observed at higher rates (*e.g.*, less than 0.1% increase in FE switching from 10 Hz sample rate to 100 Hz).

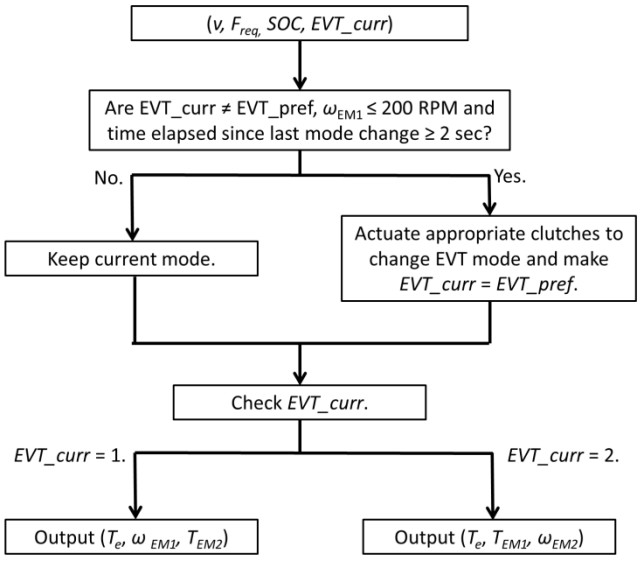

Figure 3.8: Controller decision making process

3.5 Simulation Results

In this section, the simulation results from BLS and FLS using the robust ECMS controller will be presented. The battery *SOC* and EVT mode change histories will be examined for both BLS and FLS. Comparison of the actual torque required and its lookup values will be made for an EM during FLS. Using the DP-informed method discussed previously, the reference equivalence factor (s_{ref}) is calculated to be 247 g/kW-h, using the UDDS dynamic programming data. The tangent scaling factor (β) is chosen to be 100 g/kW-h as used in Chapter 2, considering the similarities between the specifications of the power plants in these HEVs. Fuel economy figures from both BLS and FLS will also be presented and compared to the DP global optimum to evaluate the performance of the robust ECMS controller.

3.5.1 Component States in BLS vs. FLS

BLS and FLS are performed with the UDDS drive cycle using the robust ECMS controller. Figure 3.9 compares the battery *SOC* time histories of BLS and FLS.

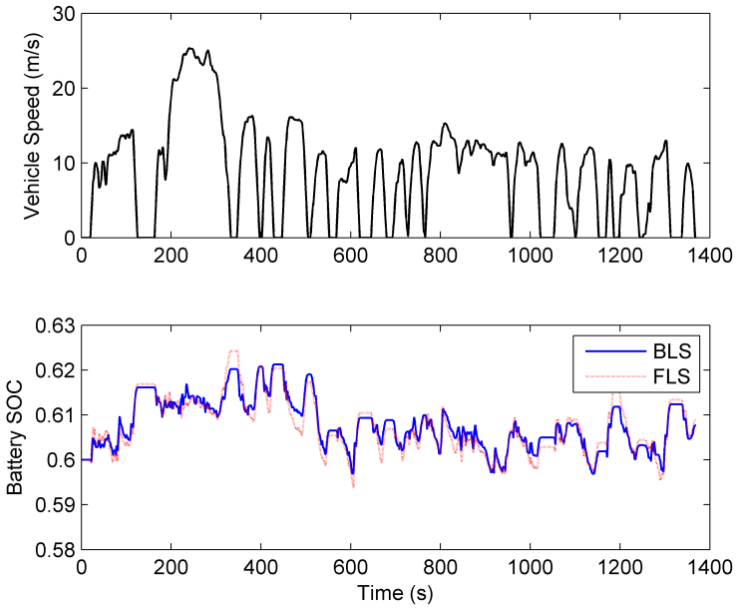

Figure 3.9: Comparison of BLS and FLS SOC trajectories

The *SOC* trajectories of both simulations have the same overall trend. However, there are instances where the FLS trajectory shows more *SOC* fluctuations (*e.g.*, between 300 sec to 500 sec). This is because BLS neglects component transients, which require extra energy. Since the battery is the energy buffer of a hybrid vehicle, extra energy variations manifest as higher fluctuations of the battery *SOC*.

Next the EVT modes used by the two types of simulators will be examined. Figure 3.10 depicts the EVT mode changes exhibited by both simulations; a high signal in either trajectory represents EVT-2 mode. Both simulations show almost the same EVT mode

usage. EVT-1 mode is primarily used for low speed take-offs, while EVT-2 mode is primarily used for high speed cruising operations.

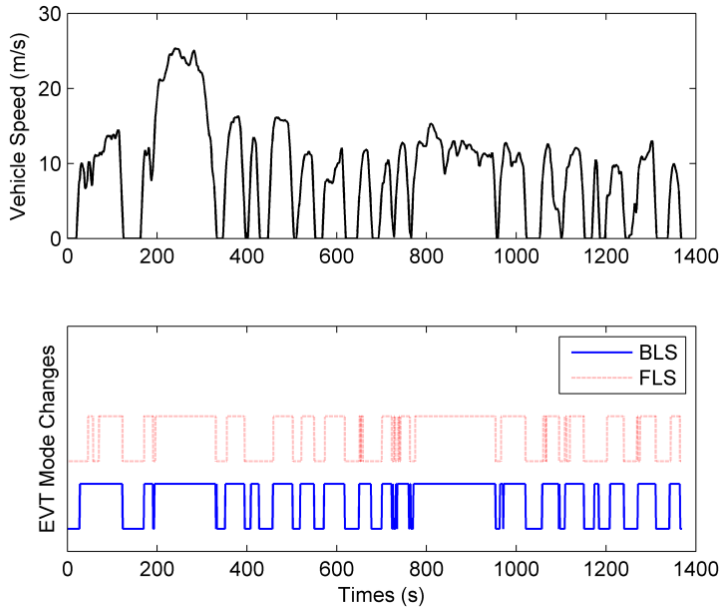

Figure 3.10: Comparison of BLS and FLS EVT mode usage

Lastly, it is important to examine how an actual component state during FLS differs from the lookup values computed by the steady-state backward-looking model. Figure 3.11 illustrates the actual and lookup torque outputs of EM1 when it is tracking a prescribed angular speed. The actual torque output is fairly close to the lookup values when the prescribed angular speed is relatively steady. When prescribed speed changes quickly, large torque spikes can be observed in the actual torque output. Again, this phenomenon stems from the fact that the lookup table values are generated by a backward-looking model that neglects component acceleration. This will not be problematic in actual applications, as the torque output of EM1 is constrained according to its torque capability data in FLS.

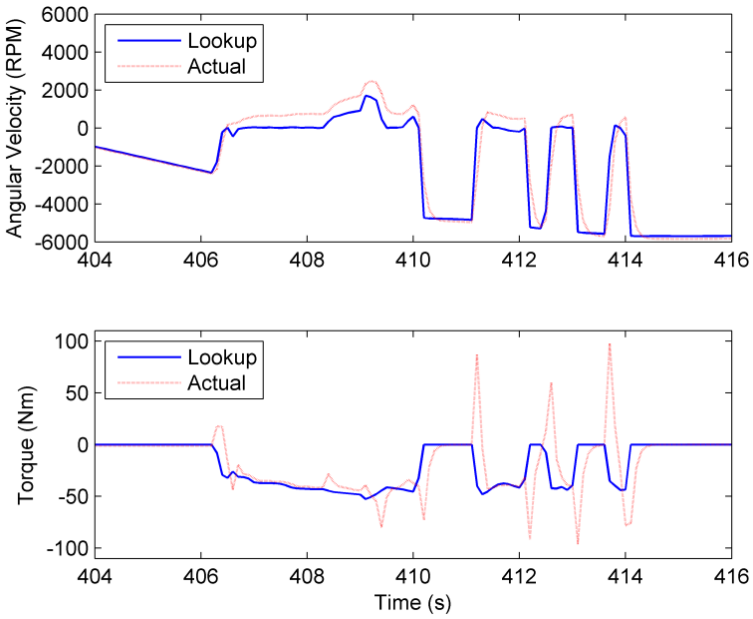

Figure 3.11: Comparison of actual and lookup torque outputs of EM1

3.5.2 Comparison of Fuel Economy in BLS vs FLS

Fuel economy results on the UDDS and the US06 drive cycle will be presented next. Since the robust ECMS controller is optimized for the UDDS drive cycle, using it on the aggressive high speed US06 drive cycle will demonstrate its cross drive cycle robustness. Since the robust ECMS controller does not use future knowledge of the drive cycle in its decision process, the end of cycle battery *SOC* is not directly enforceable, unlike in DP. End-of-cycle battery *SOC* deviation will affect the accuracy of the FE numbers. Therefore, FE simulations with the robust ECMS controller use 20 consecutive cycles of UDDS and 30 cycles of US06. This ensures less than 1% errors in the FE numbers even with the end-of-cycle *SOC* at the battery operation limits. Dynamic programming simulations only need to be performed with one execution of a drive cycle since end of cycle battery *SOC* deviation can be constrained to be zero.

Table 3.2: Fuel economy results from DP and ECMS with BLS and FLS

	UDDS		US06	
	Normalized FE	Normalized Propulsion Energy	Normalized FE	Normalized Propulsion Energy
DP	1.00	1.00	1.00	1.00
ECMS - BLS	0.98	1.00	0.99	1.00
ECMS - FLS	0.93	1.09	0.97	1.04

Table 3.2 presents the FE numbers of the robust ECMS controller, normalized to the DP global optima. Also presented is the DP-normalized propulsion energy required at the wheel for one execution of the drive cycle. The BLS with the robust ECMS controller obtains fuel economy figures within 2% of the global optima prescribed by DP. This result is consistent with that observed in Chapter 2 for other HEV architectures. While the FLS with the robust ECMS controller shows 3-7% lower FE than the BLS, the differences can be readily explained with the extra propulsion energy required in FLS. Since FLS simulates component transients, it is expected that extra energy will be lost due to acceleration of the onboard components. These FE results show that the robust ECMS controller still maintains its cross drive cycle robustness on the GM AHS-II architecture. More importantly, the FLS application of the robust ECMS controller demonstrates its potential as an online implementable control strategy.

3.6 Summary

This chapter presents a direct application of Chapter 2's robust ECMS controller on the GM AHS-II architecture in FLS. The robust ECMS controller from Chapter 2 uses dynamic programming results to inform its parameter selection and has excellent cross

drive cycle robustness. The forward-looking simulator uses lookup tables of component operation states generated by a backward-looking model. Simulation results show that FLS and BLS have similar battery *SOC* time history and EVT mode usage. Analysis of the actual torque outputs during FLS shows that BLS does not capture the torque spikes present in components due to transient effects. Fuel economy data demonstrates that the DP-informed robust ECMS controller performs well in FLS across different drive cycles, compared to the DP global optima. Discrepancies of FE numbers between FLS and BLS can be readily explained by the extra propulsion energy required to traverse the drive cycle. Since FLS mimics command structure in an actual vehicle, the results show the potential of online application of the robust ECMS controller.

CHAPTER 4

DEVELOPMENT OF A HYDRAULIC HYBRID SCHOOL BUS PROTOTYE

4.1 Introduction

As described in the introduction, hybrid electric vehicles (HEVs) are widely available as passenger vehicles and have thus been extensively studied. Hydraulic hybrid technology, on the other hand, has just started to garner attention in heavy vehicle applications. Analogous to HEVs, hydraulic hybrid vehicles (HHVs) use a hydraulic pump/motor (PM) for engine assist and regenerative braking, while employing accumulators as energy buffers. The space typically available between frame rails on a heavy vehicle allows using large accumulators. The typical stop-and-go drive cycles experienced by heavy vehicles, such as garbage refuse trucks, delivery trucks and school buses, make hybridization a rational choice for increasing overall drivetrain efficiency.

While Chapter 2 and Chapter 3 develop simulation tools and control strategies for HEVs, this chapter will focus on detailing the development of an HHV prototype. A Bluebird school bus is retrofitted with hydraulic components to produce a hydraulic hybrid bus (HHB). An overview of the system architecture and design consideration will be first given. A forward-looking simulator, which facilitated critical component sizing decisions, will then be described. Chapter 4 will go on to detail the operation of the HHV prototype, providing insights into the hydraulic system components, as well as the

microcontroller. The will help identify areas for future improvements. Finally, preliminary results and the commercialization potential of the HHB will be discussed.

4.2 Overview of the HHB System

This section provides an overview of the hydraulic hybrid bus system. The architecture chosen is a post transmission parallel hybrid. Figure 4.1 presents a hydraulic schematic of the system. The HHB uses a variable displacement hydraulic PM and two compressed-nitrogen bladder accumulators as the hybridizing power plant and the energy buffer. One high pressure (HP) and one low pressure (LP) accumulator are used. The hydraulic system stores energy from the drivetrain by pumping hydraulic oil from the LP accumulator into the HP accumulator and releases this energy by moving oil from the HP accumulator to LP accumulator, in turn powering the PM in motoring mode. Manual isolation valves are installed to allow shut-off of the accumulators when the HHB is not in use. Additionally, the pressure in each of the accumulators is monitored by a pressure sensor. Finally a 4500 psi pressure relief valve ensures the HP accumulator never pressurizes above its maximum pressure limit.

The system uses a variable displacement PM to move hydraulic fluid between the two accumulators. The displacement of the PM is controlled by a swash plate, which is actuated by two proportional solenoids (within the PM and not shown in Figure 4.1). The swash plate solenoids require a 290 psi pressure to operate. This pressure is referred to as the control pressure and is provided by a pressure reducing valve connected to the HP accumulator. The control pressure flow goes through the control circuit of the PM and ultimately to the LP accumulator through the case drain path. A mechanical pressure

gauge is installed in the control pressure line to provide a visual check of the control pressure.

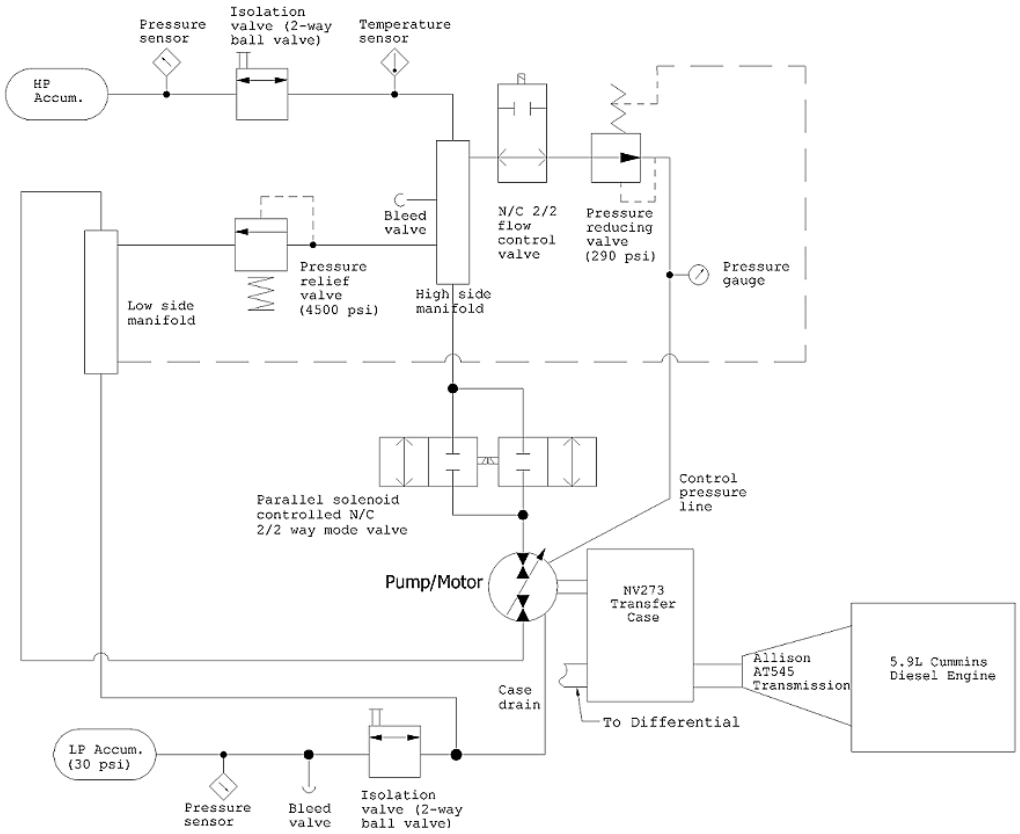

Figure 4.1: Schematic of the hydraulic system

Two normally-closed 2-way solenoid valves in parallel control the main fluid flow through the PM. Two valves are needed to accommodate the maximum flow rate of the pump. These two valves close whenever the PM is not in use to reduce the leakage through the pump.

Detailed flow diagrams of the hydraulic circuit are attached as Figures C.1 and C.2 in Appendix C. During pumping operations, hydraulic fluid from the LP accumulator combines with the drain flows in the system before going into the PM. The PM displaces

this hydraulic fluid by taking power from the drivetrain and delivers the fluid to the HP accumulator at high pressure. During motoring operation, the high pressure fluid from the HP accumulator flows through the PM to provide power to the drivetrain. The flow out of the pump combines with two drain flows before going into the LP accumulator. In both motoring and pumping operations, part of the fluid in the HP accumulator goes through the pressure reducing valve to provide a control pressure to the PM.

The hybrid system retains the bus's original Allison 545 transmission and the 5.9L Cummins diesel engine. An added NV273 transfer case couples the output of the transmission and the PM with a 1:1 ratio. The HHB can operate with the PM coupled and use it as a motor to enhance acceleration, or as a pump to recapture braking energy. The transfer case can also disengage the PM from the drivetrain to reduce parasitic torque when the PM is not in use. However, on the fly engagement and disengagement of the transfer case are not yet feasible as explained later.

4.3 Forward-looking Simulator of the HHB

A forward-looking simulator of the HHB informs key component sizing decisions and assesses potential fuel economy improvement of the hybrid bus over the unmodified bus. The simulation of the powertrain uses MATLAB Simulink with the Simscape package. The Simulink model works by solving Newton's Second Law for rotational motion for each of the components modeled. This section will detail the modeling methodology of the HHB.

4.3.1 HHB Driver Model

A PID controller emulates a driver following a drive cycle; it is illustrated in Figure 4.2. The difference between the speed of the vehicle and the speed prescribed by a drive

cycle creates an error signal fed into the PID controller. The PID controller converts the error signal into a a control signal between 1 and -1. A positive control signal represents an acceleration request while a negative control signal represents a braking request.

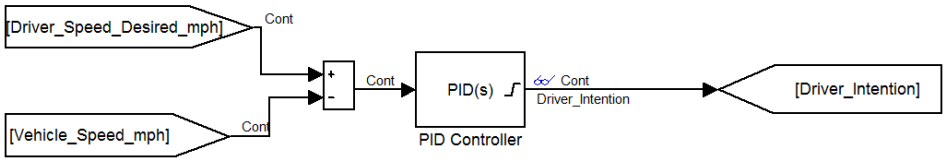

Figure 4.2: HHB driver model

4.3.2 HHB Engine Model

The Cummins 5.9L diesel engine equipped on the school bus is modeled with look-up tables for engine torque output and engine fuel consumption.. While the engine torque and fuel consumption data is not available for the Cummins 5.9L diesel engine, it is approximated from data of a small diesel engine by scaling the engine torque and fuel consumption proportionally with engine displacement.

4.3.3 HHB Transmission Model

The 4-speed automatic transmission is modeled with a modified Ravigneaux 4-Speed, and a Torque Converter block from Simulink's SimDriveline library. Figure 4.3 shows the transmission model in Simulink. The shift logic is governed by vehicle speed and throttle signal as described in [37] and [38] for automatic transmissions. The shift signal σ_{shift} is modeled as the following,

$$\sigma_{shift} = v - \varepsilon_{thr}\sigma_{thr} \tag{4.1}$$

where v is the vehicle velocity, σ_{thr} is throttle signal and ε_{thr} is some positive constant. Transmission gear changes occur at predetermined threshold values of σ_{shift}. Upshifting occurs with increased vehicle speed while the throttle signal can delay upshifting or cause downshifting.

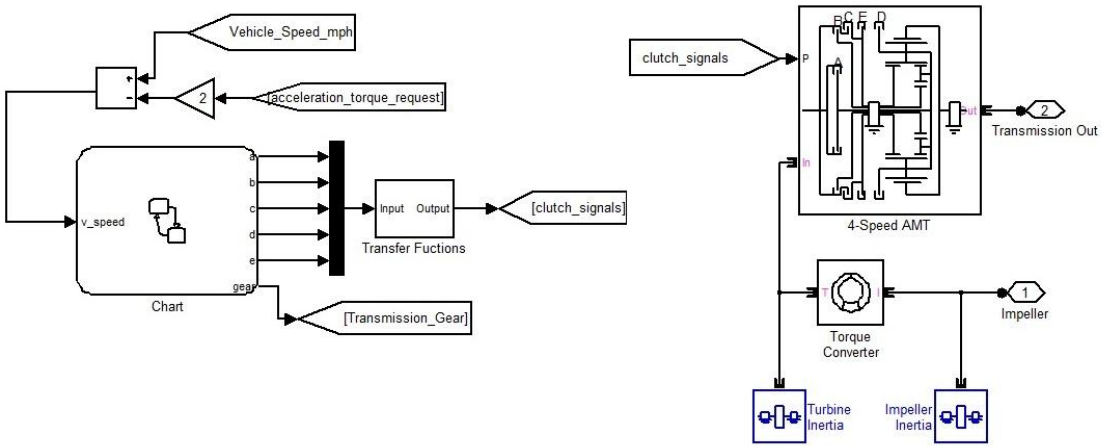

Figure 4.3: Transmission system model

Different gear ratios of the automatic transmission are produced by different engagements of clutches in the transmission. A stateflow chart determines the clutch engagements and generates the appropriate clutch pressure signals.

4.3.4 HHB Vehicle Model

The vehicle drivetrain is modeled with a series of rotational bodies with inertias and torque actuators. Simulink solves the equations of motions using the torque input from the powertrain and computes the resulting longitudinal force on the vehicle body. Figure 4.4 presents the vehicle model in Simulink.

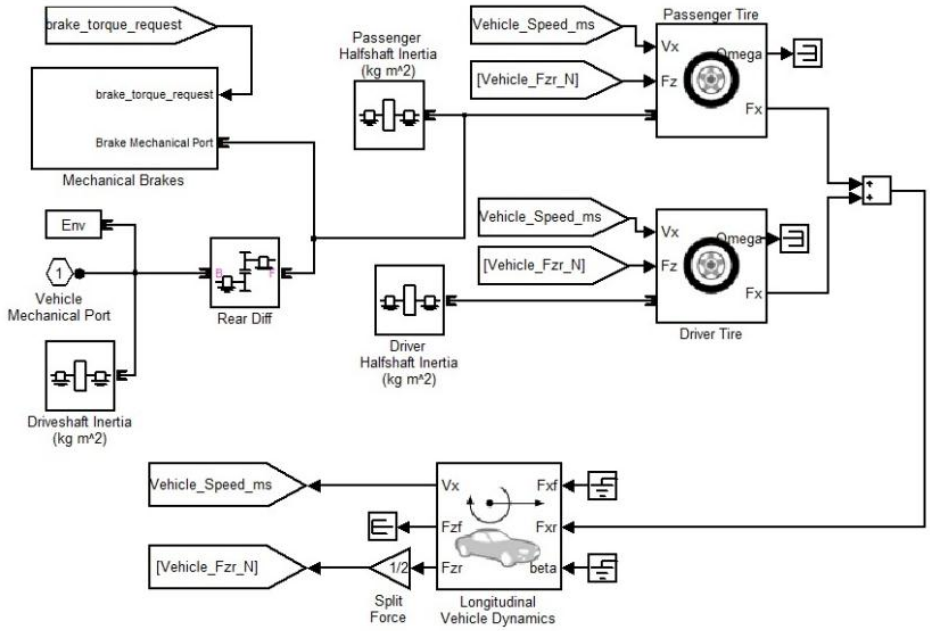

Figure 4.4: Vehicle system model

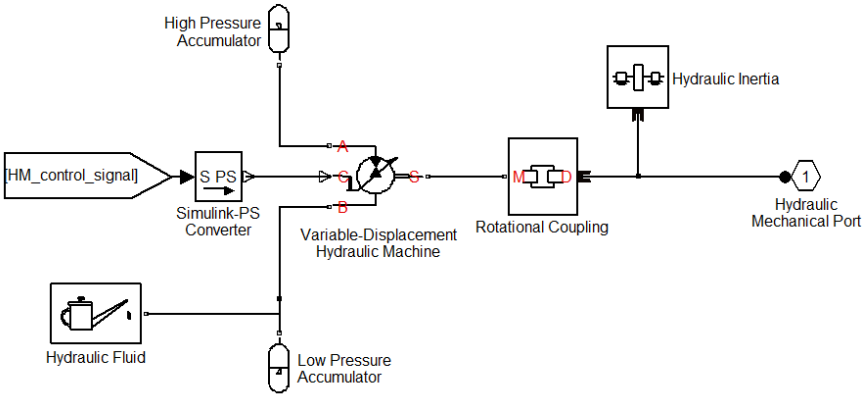

Figure 4.5: Hydraulic system model

4.3.5 HHB Hydraulic System Model

The hydraulic system consists primarily of a PM connected with two accumulators as shown in Figure 4.5. The PM delivers positive power to the drivetrain by releasing

hydraulic fluid from the high pressure accumulator to the low pressure accumulator; it delivers negative power to the drivetrain by pumping fluid from the lower pressure accumulator to the high pressure accumulator. A control signal controls the direction of the hydraulic fluid flow and thus the power flow.

4.3.5.1 Hydraulic Pump/Motor Model

The modeling of the PM is based on Simscape's Variable-displacement Hydraulic Machine block. The governing equations use pump displacements, shaft angular velocities, pressure differentials and a number of efficiency coefficients to determine the instantaneous torque and flow rate of the PM [39]. An overview of the modeling equations and some important observations will be given here. When the PM operates as a pump, the pumping flow rate q_p and shaft torque T_p are modeled as,

$$q_p = D \cdot \omega - q_L \tag{4.2}$$

$$T_p = D \cdot P_{PM} + T_{fr} \tag{4.3}$$

where ω and D represents the angular velocity and instantaneous displacement of the PM, P_{PM} the pressure different between the high and low pressure ports of the PM, and q_L and T_{fr} the leakage and frictional torque inside the PM. Similarly, when the PM operates as a motor, the motoring flow rate q_m and shaft torque T_m are,

$$q_m = D \cdot \omega + q_L \tag{4.4}$$

$$T_m = D \cdot P_{PM} - T_{fr} \tag{4.5}$$

The leakage and frictional torque of the PM can be approximated as,

$$q_L = \bar{D} \cdot \bar{\omega} \cdot k_L (\overline{P_{PM}})^{k_{LP}} (\bar{D})^{k_{LD}} (\bar{\omega})^{k_{L\omega}} \tag{4.6}$$

$$T_{fr} = \bar{D} \cdot \overline{P_{PM}} \cdot k_F (\overline{P_{PM}})^{k_{FP}} (\bar{D})^{k_{FD}} (\bar{\omega})^{k_{F\omega}} \tag{4.7}$$

where $\overline{P_{PM}}$, $\bar{D}$ and $\bar{\omega}$ are the pressure difference, instantaneous displacement and angular velocity normalized to their respective maximums; the quantities k_L, k_{LP}, k_{LD}, $k_{L\omega}$, k_F, k_{FP} , k_{FD} ,and $k_{F\omega}$ are correlating coefficients. The volumetric and mechanical efficiencies, η_{Vp} and η_{Mp}, of the PM when pumping can then be defined as,

$$\eta_{Vp} = \frac{q_p}{q_{p,th}} = \frac{D\omega - q_L}{D\omega} = 1 - k_L(\overline{P_{PM}})^{k_{LP}}(\bar{D})^{k_{LD}}(\bar{\omega})^{k_{L\omega}} \tag{4.8}$$

$$\eta_{Mp} = \frac{T_{p,th}}{T_p} = \frac{DP_{PM}}{DP_{PM} + T_{fr}} = \frac{1}{1 + k_F(\overline{P_{PM}})^{k_{FP}}(\bar{D})^{k_{FD}}(\bar{\omega})^{k_{F\omega}}} \tag{4.9}$$

where the subscript "*th*" denotes the theoretical quantities under full efficiency. Similarly, for motoring, the volumetric and mechanical efficiencies are,

$$\eta_{Vm} = \frac{q_{m,th}}{q_m} = \frac{D\omega}{D\omega + q_L} = \frac{1}{1 + k_L(\overline{P_{PM}})^{k_{LP}}(\bar{D})^{k_{LD}}(\bar{\omega})^{k_{L\omega}}} \tag{4.10}$$

$$\eta_{Mm} = \frac{T_m}{T_{m,th}} = \frac{DP_{PM} - T_{fr}}{DP_{PM}} = 1 - k_F(\overline{P_{PM}})^{k_{FP}}(\bar{D})^{k_{FD}}(\bar{\omega})^{k_{F\omega}} \tag{4.11}$$

One key purpose of the forward-looking simulator is to determine the optimal PM sizing for an Eaton/Linde DuraForce PM. Since the efficiency depends on dimensionless variables of a PM, it is reasonable to assume that PMs of the same series have the same efficiency coefficients. As a result, the experimental pumping efficiency data of a DuraForce PM is used to model the entire series. Linearization of Eq. (4.8) and Eq. (4.9) yields the following linear correlations used to fit the experimental pumping efficiencies from [40].

$$\ln(1 - \eta_{Vp}) = \ln(k_L) + k_{LP}\ln(\overline{P_{PM}}) + k_{LD}\ln(\bar{D}) + k_{L\omega}\ln(\bar{\omega}) \tag{4.12}$$

$$\ln(1 - \eta_{Mp}) - \ln(\eta_{Mp}) = \ln(k_F) + k_{FP}\ln(\overline{P_{PM}}) + k_{FD}\ln(\bar{D}) + k_{F\omega}\ln(\bar{\omega}) \tag{4.13}$$

Table 4.1 presents the estimated efficiency coefficients found from the experimental data fit. By examining Table 4.1 and Eqs. (4.4) to (4.11), it can be deducted that the operating displacement of the PM has the same effect on both the volumetric and mechanical efficiencies – the closer the PM is operating at maximum displacement, the more efficient it is. However, the operating pressure and angular velocity of the PM have opposing effects on PM efficiencies.

Table 4.1 Correlating efficiency coefficients of the Eaton/Linde DuraForce PMs

Volumetric Efficiency		Mechanical Efficiency	
k_L	0.06	k_F	0.05
k_{LP}	1.19	k_{FP}	-0.76
k_{LD}	-1.17	k_{FD}	-0.73
$k_{L\omega}$	-0.38	$k_{F\omega}$	0.46

To further characterize the efficient operation regime of the PM, the volumetric and mechanical efficiencies of the PM can be combined into a single efficiency metric. The volumetric efficiency prescribed in Eq. (4.8) can be redefined as,

$$\eta_{Vp} = \frac{q_p}{q_{p,th}} = \frac{D * \omega_{th}}{D * \omega} = \frac{\omega_{th}}{\omega} \tag{4.14}$$

Combine the new definition of volumetric efficiency from Eq. (4.14) with mechanical efficiency defined in Eq. (4.9), it can be obtained the following relationships for pumping,

$$T_p \omega_p = \frac{T_{p,th} \omega_{p,th}}{\eta_{Mp} \eta_{Vp}} \tag{4.15}$$

A combined pumping power efficiency can then be defined as $\eta_{Cp} = \eta_{Mp}\eta_{Vp}$ from Eq. (4.16). Similarly the combined motoring power efficiency can be defined as $\eta_{Cm} = \eta_{Mm}\eta_{Vm}$. Figures 4.6 and 4.7 depict the combined pumping and motoring efficiency contours parameterized by $\bar{\omega}$ and $\overline{P_{PM}}$ while holding $\bar{D}$ constant at 0.5.

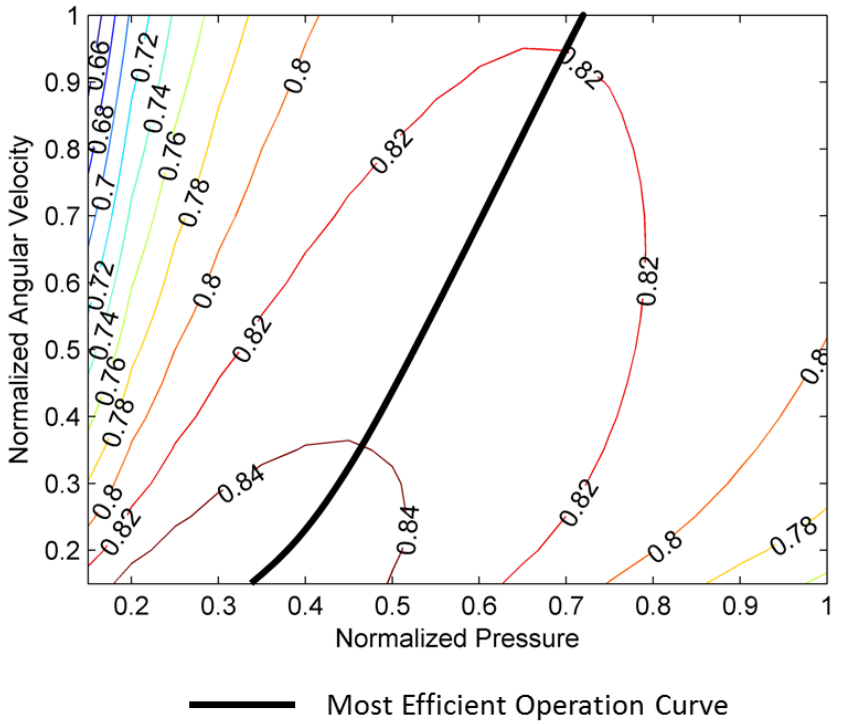

Figure 4.6: Combined pumping power efficiency contours

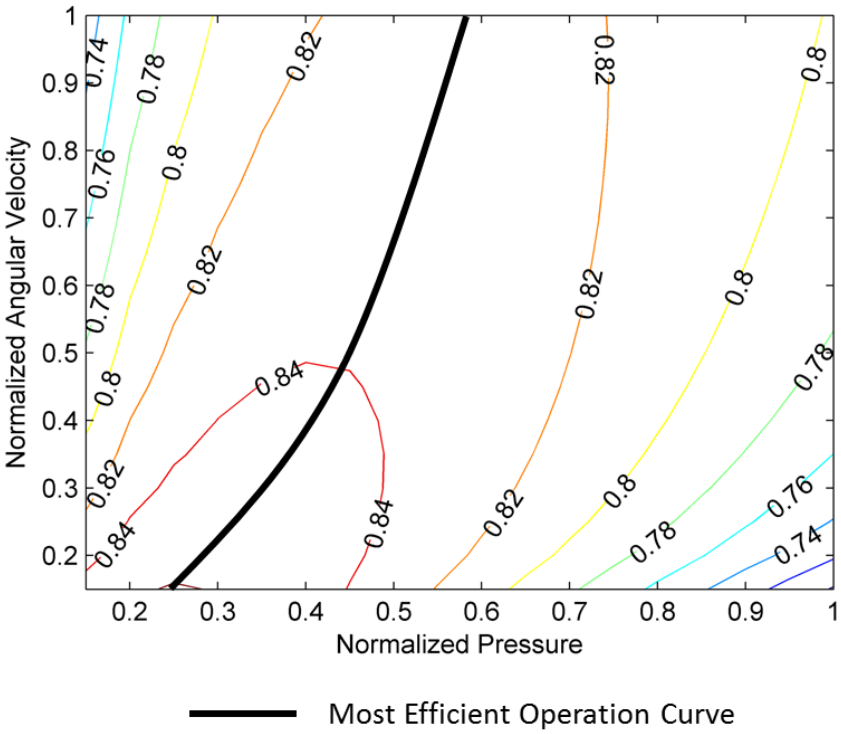

Figure 4.7: Combined motoring power efficiency contours

Both contour plots have similar shapes and suggest the most efficient combinations of pressure and PM angular velocity. The efficient operation regime of the PM involves moderate speed and pressure, while most inefficient operation regime involves maximum pressure at low speed or maximum speed at low pressure. Finally, the thick black line marks the most efficient operation curve on each efficiency map.

4.3.5.2 Accumulator Model

The accumulators are modeled assuming nitrogen gas in the bladder undergoes adiabatic compression and expansion. This simulates the fast charging and discharging of the accumulators, which are assumed to occur during typical operation of the HHB. The pressure P_{gas} and V_{gas} of the nitrogen gas in the accumulator thus have the following relation,

$$P_{gas}{V_{gas}}^{k} = const. \tag{4.16}$$

where *k* is the specific heat capacity ratio for nitrogen, which is 1.4. The state of charge of the accumulator is defined as the following,

$$SOC = \frac{P_{gas} - P_{gas,pre}}{P_{gas,max} - P_{gas,pre}} \tag{4.17}$$

where the subscripts "*pre*" and "*max*" denote the precharge and maximum pressures, respectively.

Since the work of the gas and its change in internal energy sum to zero during an adiabatic process, the change in internal energy of the gas can be represented as,

$$\Delta U_{gas} = (k-1)P_{gas,0}V_{gas,0}\left(\left(\frac{P_{gas,f}}{P_{gas,0}}\right)^{(k-1)/k} - 1\right) \tag{4.18}$$

Equation (4.18) can be used to correct the fuel economy figures for the change in stored energy in the accumulators at the end of a drive cycle. Furthermore, it can also be used to

calculate the maximum energy buffer capability of the accumulators given the operating pressure limits.

4.3.6 HHB Simulation Results and Component Sizing

The main purpose of the HHB simulator is to assess fuel economy gain and inform component sizing. The main components of the hydraulic system under consideration are the variable-displacement PM and the accumulators. The sizing of these components determines the amount of available power and energy buffer of the hydraulic system. The forward-looking simulators allow rapid iteration through various PM and accumulator combinations to test their combined effects on fuel economy. The fuel economy simulation is done on the EPA's UDDS drive cycle. The vehicle velocity is scaled by 2/3 to account for slower speed and acceleration of a typical bus.

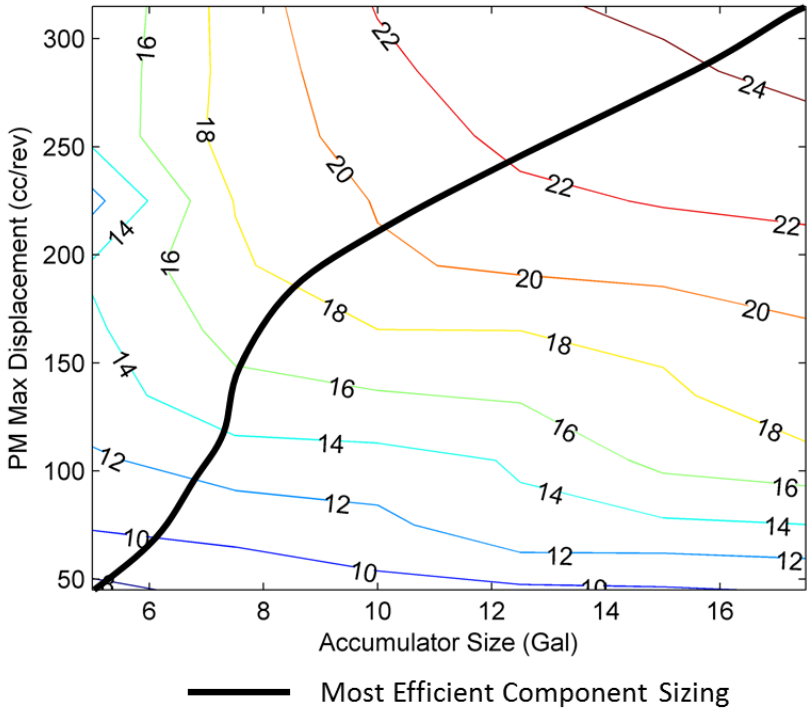

Figure 4.8: Percent fuel economy gain parameterized by component sizing

Figure 4.8 shows simulated fuel economy gains in percentages over the unmodified baseline using different combinations of PM and accumulators. Figure 4.8 suggests that, in general, increasing either the displacement of the PM or the volume of the accumulators, increases fuel economy gain. Furthermore, the thick black curve indicates roughly the most efficient component sizing. The most efficient component sizing curve suggests that fuel economy gain is achieved most efficiently by increasing the PM max displacement when accumulator volumes are small. Accumulator sizing becomes more critical when the PM max displacement reaches 150 cc/rev. Ultimately, the PM max displacement is chosen to be 280 cc/rev and the accumulator volume chose to be 15 gallon for each of the accumulators. This combination allows maximal fuel economy gain using off-the-shelf products.

4.4 HHB Prototype

The HHB prototype is built by retrofitting a Bluebird TC2000 school bus with hydraulic components. An undergraduate student team conducted the first year of system design [41]. Many details have changed since the initial design work and this thesis will provide an updated and all-inclusive description of the HHB prototype.

4.4.1 Hydraulic System

This section will cover the key hydraulic and mechanical components of the HHB. Descriptions of the component operation and maintenance will be given here and Figure C.3 in Appendix C provides a pictorial reference for the components fitted to the HHB. Finally, this section will also suggest areas for future improvements.

4.4.1.1 Pump/Motor

The hydraulic system uses a Eaton/Linde variable displacement pump/motor with 280 cc/rev maximum displacement. The model number of the pump is **HPV280R0T4ME1D0L21SAA0000000000000AA**, which can be used to look up the exact specifications in [42]. The PM is an axial piston pump using a swash plate to achieve variable displacement. Figure 4.9 shows an engineering drawing of the PM with its key plumbing ports labeled. While installed on the HHB, the right side of Figure 4.9 faces the bottom of the HHB. Port P and Port S of the PM are the main plumbing ports that connect to the hydraulic circuit. The high pressure side of the hydraulic circuit is connected to Port P (through the parallel solenoids as shown in Figure 4.1) while the low pressure side of the hydraulic circuit is connect to Port S. The PM features multiple drain ports for entrapping air in the hydraulic system. On the HHB, only Port L is used for such purposes because it is situated on the highest face of the PM when it is mounted.

One key specification of the pump is that it uses electro-proportional solenoids, labeled as Mz and My in Figure 4.9, to actuate the swash plate. Direction of the swash plate actuation, as well as the direction of PM shaft rotation, determines the pump shaft torque and fluid movement between the two main ports. On the HHB, when the PM shaft is rotating in the clockwise direction, energizing swash plate solenoid Mz will transfer hydraulic fluid from the Port P to Port S. This will result in a clockwise torque on the PM shaft. In the specific configuration used on the HHB prototype, this accelerates the HHB forward. The direction of the fluid flow and the shaft torque reverse when swash plate solenoid My is activated. When the PM shaft is stationary, energizing either swash plate solenoid will allow fluid to flow from the HP side of the hydraulic circuit to the LP side. In this case, the specific swash plate solenoid energized determines the direction of

PM shaft torque. For example, energizing swash plate solenoid My will rotate the PM shaft in the counter-clockwise direction. All rotational directions specified assume viewing the PM straight down the shaft as in the view of Figure 4.9.

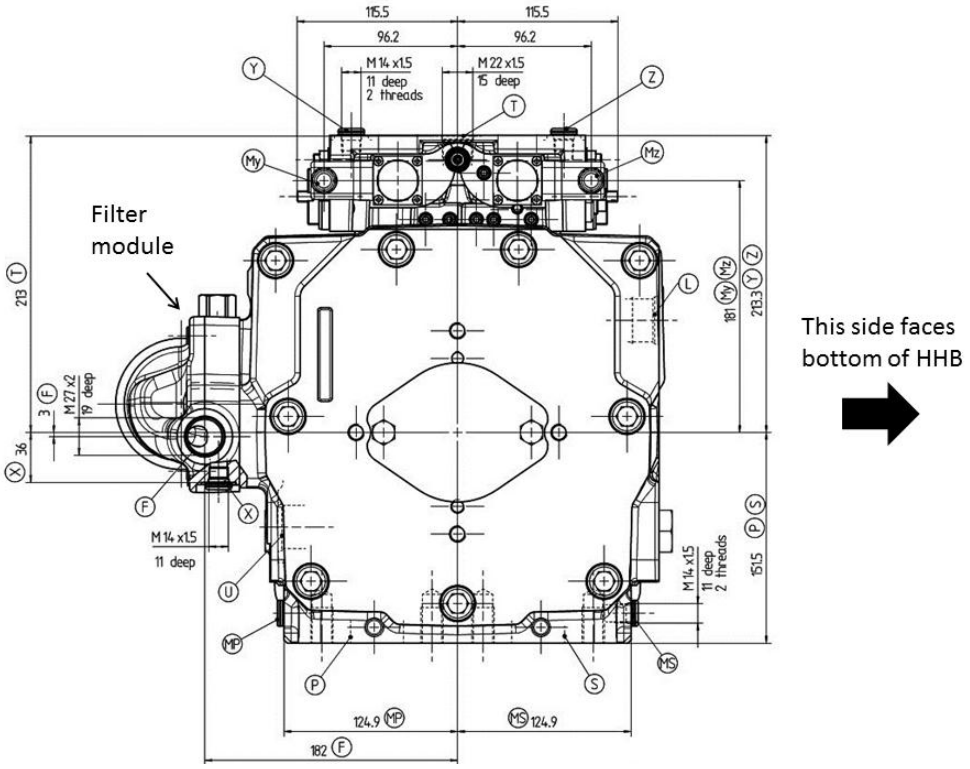

Figure 4.9: Schematic of the Eaton/Linde DuraForce pump

The swash plate solenoids operate on 24 V DC power and require a constant 290 psi control pressure. This pressure is provided by an adjustable pressure reducing valve reducing the flow from the HP accumulator to 290 psi. The working of the pressure reducing valve will be discussed in detail later. An implication of this setup is that the HP accumulator must be above 290 psi for the PM to work.

On the HHB, the 24 V signals to the swash plate solenoids are modulated by pulse-width modulation (PWM). The goal is to produce a current drawn in the range of 225

mA to 650 mA as specified by [43]. The current drawn by a swash plate solenoid is the most reliable way to verify the working order of the swash plate since this PM used does not have a swash plate angle sensor. One important thing to note is that the current drawn by a swash plate solenoid does not vary linearly with PWM duty cycle supplied. Figure 4.10 addresses this issue by plotting the experimental duty cycle supplied vs. current drawn data by a swash plate solenoid. As shown in Figure 4.10, the current response contains a dead zone between 0% to 75% duty cycles, after which the response is approximately linear. Equation (4.19) is least square fit to the linear region of the current response.

$$A_{sol} = 25.6(\%\ duty\ cycle) - 1770 \tag{4.1}$$

The data in Figure 4.10 is obtained using the Arduino-based controller. Should uncertainties regarding the swash plate solenoid working order arise after a controller hardware change, it will be imperative that the current drawn is checked against the PWM signal supplied.

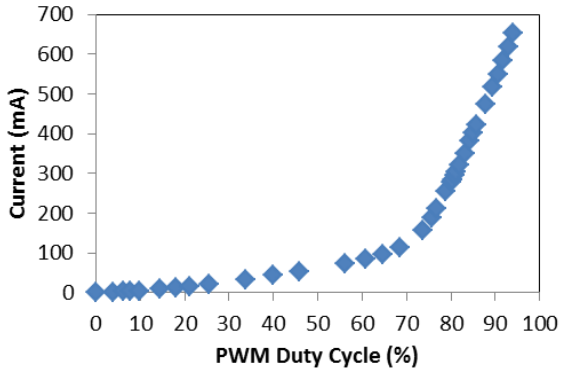

Figure 4.10: Swash plate solenoid current response

Another challenge in controlling the swash plate is returning it to the neutral position efficiently. In normal application of the DuraForce PM, control pressure is always supplied to the swash plate solenoids either via an internally geared or an external boost pump pumping oil from the low pressure side of the hydraulic system. This constant supply of control pressure returns the swash plate to its neutral position when the swash plate solenoids are not energized. However, on the HHB prototype, the control pressure is supplied by the HP accumulator. To reduce energy loss, the control pressure is shut-off when the PM is not in use. Control logics are implemented to return the swash plate to its neutral position efficiently. They will be detailed in Section 4.4.2 along with other information regarding the microcontroller.

4.4.1.2 Accumulators

Buna-Nitrile bladder accumulators from Accumulators Inc. are used in the HHB hydraulic system. The hydraulic system employs two accumulators, one at high pressure (1500 psi to 4500 psi) and another at low pressure (8 psi to 24 psi). This realizes a completely closed system and obviates the need for a filter element in the hydraulic system. Besides the reason of maximizing the energy storage capability, the LP accumulator uses such low pressure range because it is connected to the case drain Port L of the PM. It is not recommended to exceed 30 psi in such locations for protecting the integrity of the seals in these ports.

The gas bladder of the accumulators should be charged with industrial grade pure nitrogen only. The pre-charge pressure of the bladder should be at least 30% of the maximum working pressure [44]. Additionally, the minimum working pressure should be approximately 40% of the maximum working pressure. In general, this ensures there

is always fluid supplied to the pump for lubrication. Specifically in the case of the HP accumulator, as it also supplies the control pressure to the swash plate solenoids, a margin of safety above the pre-charge pressure ensures it can always supply the control pressure to operate the swash plate. The swash plate cannot be actuated if the HP accumulator runs out of fluid. The charging procedure for the gas bladder can be found in the manufacture's maintenance guide [44].

Assuming the capacity of an accumulator is split only between the gas and oil volumes, the maximum oil volumes in the accumulators can be calculated using the ideal gas law from Equation (4.16). Such calculations should be carried out using 1.4 for the heat capacity ratio (k). Equation (4.16) requires absolute pressures, while all pressures quoted are gage pressures. Using gage pressures does not result in large errors in calculations for the HP accumulators, but it will be significant for the LP accumulator since it is operating very close to atmospheric pressure.

4.4.1.3 Parallel Solenoid Valves

The main purpose of the parallel solenoid valves is to shut off the high pressure on the PM when it is not in use, as the leakage from Port P to Port S can be substantial when the pressure difference is high. The parallel solenoids valves only open when the PM swash plate is actuated to allow fluid flow between accumulators.

The parallel solenoid valves are 2-way, 2-position, normally-closed and bi-directional poppet valves. They are actuated by magnetic coils. The specific coils used on the HHB have a voltage and power requirements of 12 V and 19 W. Normally closed valves are chosen to ensure no fluid flow when the power is cut off.

4.4.1.4 Pressure Reducing Valve and Pressure Relief Valve

An adjustable pressure reducing valves reduces the flow from the HP accumulator to 290 psi to provide a control pressure for the PM swash plate solenoids. As the PM only requires the control pressure to operate the swash plate, a solenoid valve is employed to shut off the flow to the pressure reducing valve when the swash plate is not being actuated. This is necessary because the leakage through the PM control circuit is estimated to be at least 1/4 gallon per minute, a substantial rate given the volume of the accumulators.

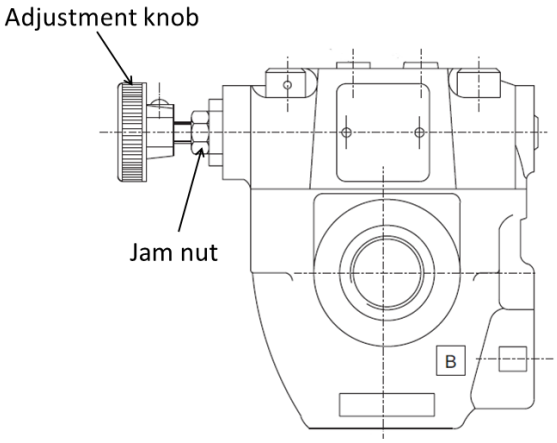

Figure 4.11: Engineering drawing of the pressure reducing valve, reproduced from [45]

A physical gauge is installed in the control pressure line to provide a visual check of the control pressure. This also allows adjustment of the pressure reducing valve setting while it is installed on the HHB. Figure 4.11 shows an engineering drawing of the pressure reducing valve. The most important features of the pressure reducing valve are the adjustment knob and the jam nut for pressure setting adjustment. To adjust the pressure setting, one must first ensure the HP accumulator has sufficient fluid (pressure

should be twice the pre-charge) and its pre-charge pressure is well about 290 psi, then the solenoid valve controlling the flow to the pressure reducing valve should be energized. Next, the jam nut should be loosened slightly and the set screw on the adjustment knob should be tightened with an Allen key. The adjustment knob is turned until the desired pressure reading is indicated on the physical pressure gauge. The set screw should be loosened and the jam nut tightened after adjustment.

The pressure reducing valve also doubles as a manual pressure relief valve for the HP accumulator. It can also be used to transfer the hydraulic oil from the HP accumulator to the LP accumulator, albeit slower than using the parallel solenoid valves for this same purpose. On the other hand, a pressure *relief* valve is installed to provide automatic relief when the pressure in the HP accumulator exceeds a certain threshold. The pressure relief valve is nonadjustable and factory-set to relieve at 4500 psi.

4.4.1.5 Transfer Case

A transfer case connects the PM to the rest of the drivetrain. It is an NV273 transfer case that is originally designed as a 4-wheel-drive device for large pickup trucks. On the HHB, it acts as a coupling that combines the torque from the transmission and the PM. Figure 4.12 shows an actual image of the transfer case.

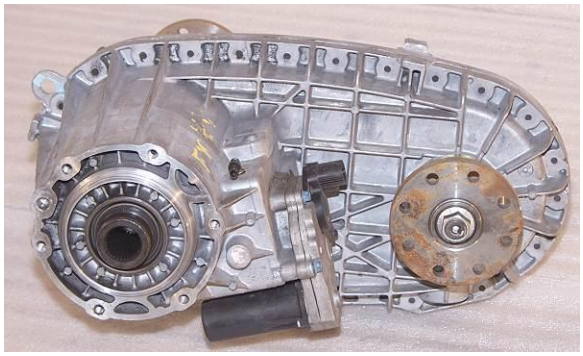

Figure 4.12: Transfer case, reproduced from [41]

The transfer case uses an electric shift motor to shift gears and an encoder to sense the shift motor position. Since the transfer case does not have a clutch, it is predicted that the binding in the transfer case will be too strong for shifting on the fly. As a result, the shift motor is removed and the transfer case is set to have the PM engaged to the drivetrain through manually adjusting the knob where the shift motor connects. The ratio between the driveshaft speed and the PM shaft speed is 1:1. In the event when the PM needs to disengage from the rest of the drivetrain, the shift knob can be turned to a disengaging position. Figure 4.13 shows the engaging and disengaging positions of the transfer case. Position 1 disengages the PM from the drivetrain while position 2 engages the PM. The shift knob can go into two more positions to the counter-clockwise direction of position 2 shown in Figure 4.13. One of those positions changes the gear ratio between the PM to the drive shaft to 2.47:1 while the other disengages both the transmission output and the PM from the driveshaft. As the 1:1 gear ratio results in higher fuel economy in the forward-looking simulation and the transmission output should connect to the driveshaft at all times, these two shift knob positions are irrelevant and never used.

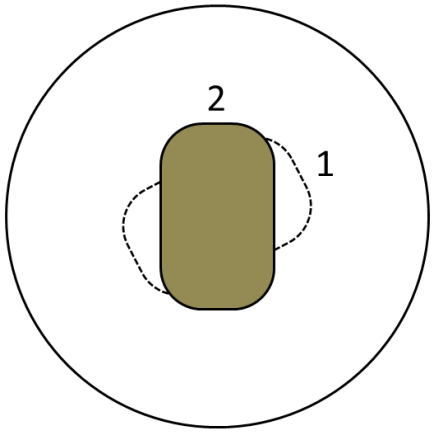

Figure 4.13: Usable transfer case shift knob positions

4.4.2 HHB Controller

The HHB controller is based on an Arduino, which is an open-source microcontroller platform. A custom fabricated printed circuit board (PCB) is employed to allow the Arduino to interface with the various types of inputs and outputs on the HHB. This section will detail the specification of the microcontroller hardware and the control logic.

4.4.2.1 Arduino

An Arduino Uno board is the heart of the microcontroller. It uses a 16 MHz crystal oscillator and has digital input/output and analog input capabilities [46]. Some digital I/O pins also support PWM with 8 bit resolutions while all the analog input pins have 10 bit resolutions. The I/O of the Arduino Uno board are 5 V based while there is also a 3.3 V power supply pin present on the board. Table 4.2 details a summary of the Arduino Uno specifications.

Table 4.2: Summary of Arduino Uno specifications [46]

Property	**Specification**
Microcontroller	ATmega328
Operating Voltage	5V
Input Voltage (recommended)	7-12 V
Input Voltage (limits)	6-20 V
Digital I/O Pins	16
Digital I/O Pins w/ PWM	4
Digital I/O PWM Resolution	8 bit
Analog Input Pins	6
Analog Input Resolution	10 bit
DC Current per I/O Pin	40 mA
DC Current for 3.3 V Pin	50 mA
Flash Memory	32 KB
SRM	2 KB
EEPROM	1 KB
Clock Speed	16 MHz

The Arduino programming language is based on C and contains a wealth of built-in functions. Its shortcomings include slow microcontroller clock speed and the small number of I/Os. Nevertheless, most of the testing of the HHB to date has been performed using the Arduino Uno due to it having a relatively simple programming language and fast compile time. As the controller logic becomes more complicated or as the number of I/Os increases, it may be necessary to move on to a more powerful controller board with faster processing speeds and more I/Os.

4.4.2.2 Controller Input and Output Requirements

The microcontroller interfaces with a wide variety of the sensors and devices on the HHB. While all the sensor outputs are 5 V based, they have different voltage input requirements. Furthermore the solenoid valves use 12 V inputs while the swash plate solenoids require 24 V inputs with PWM. Table 4.3 details the input and output requirements for the HBB controllers.

Table 4.3: HHB controller input and output specifications, amended reproduction from [41]

Component	**Input Requirements**	**Measured Output**		**Arduino**		
		Unit	Range	Type	I/O	Pin #
Throttle Position	N/A	V	0 – 5	A	I	A0
Brake Position	+5V	V	0 – 5	A	I	A1
Accumulator Pressure (LP)	+12V	V	1 – 5	A	I	A2
Accumulator Pressure (HP)	+12V	V	1 – 5	A	I	A3
Driveshaft Speed	N/A	V	0 – 5	A	I	A4
Hydraulic Fluid Temperature	+5V	V	0 – 5	A	I	A5
Swash Plate Solenoid My	+24V, 200-650mA	–	–	D PWM	O	9
Swash Plate Solenoid Mz	+24V, 200-650mA	–	–	D PWM	O	10
Transfer Case Shift Motor (Forward)	+12V	–	–	D PWM	O	5
Transfer Case Shift Motor (Reverse)	+12V	–	–	D PWM	O	6
Encoder (Wire 1)	+5V	V	0 or 5	D	I	1
Encoder (Wire 2)	+5V	V	0 or 5	D	I	2
Encoder (Wire 3)	+5V	V	0 or 5	D	I	3
Encoder (Wire 4)	+5V	V	0 or 5	D	I	4
Parallel Solenoid Valve 1	+12V	–	–	D	O	12
Parallel Solenoid Valve 2	+12V	–	–	D	O	7
Control Pressure Solenoid Valve	+12V	–	–	D	O	11
Parallel Solenoid Valve Override Switch	+5V	V	0 or 5	D	I	8
Control Pressure Solenoid Valve Override Switch	+5V	V	0 or 5	D	I	0

The sensors on the HHB include two potentiometers, two pressure sensors, one Hall Effect sensor and one temperature sensor. The potentiometers are used to measure brake and throttle pedal positions. The throttle position potentiometer requires no power supply as it is a built-in throttle potentiometer on the bus, while the brake potentiometer needs a 5 V power supply. The pressure sensors require voltage supplies in the range of 10-28 V, while outputting 1-5 V signals that vary linearly with the their pressure range. Using the 0-7500 psi pressure sensor installed in the HP accumulator as an example, an 1 V signal responds to 0 psi while a 5 V signal corresponds to 7500 psi and the signal varies linearly in between the pressure limits. The Hall Effect sensor is an existing driveshaft speed sensor on the bus. Every time the drive shaft makes a revolution, a pulse can be observed in the Hall Effect sensor signal. By recording the number of pulses in a given time, the RPM of the driveshaft can be calculated. Finally, the temperature sensor is a variable resistor. The temperature sensor is installed in series with a 5 kΩ resistor and the voltage drop across the 5 kΩ resistor is measured. The calibration is done in [41] and Figure 4.14 displays the calibration curve adapted from [41].

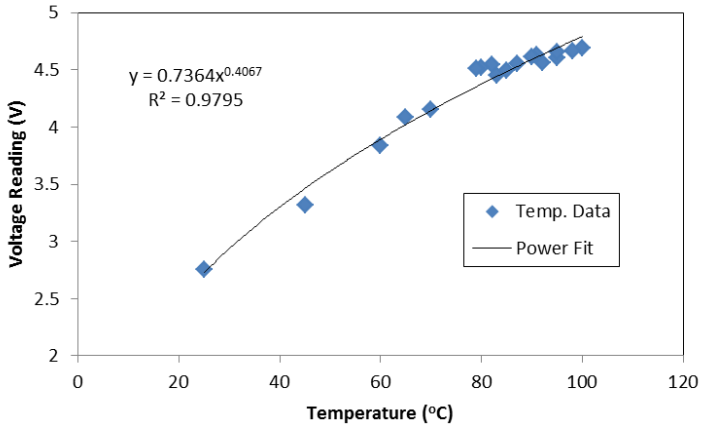

Figure 4.14: Temperature sensor calibration data, adapted from [41]

Finally, the microcontroller also has planned capabilities for controlling the transfer case shift motor. As described before, the transfer case has a shift knob on its casing. Normally, the shift knob is turned with a 12 V DC motor with an attached encoder for positions tracking. The DC motor requires both –12 V and +12 V DC power for forward and reverse movement. An H-bridge normally used for robotic applications converts the 12 V DC power from the HHB battery into both –12 V and +12 V. Two 5 V signals with PWM from the Arduino modulates the voltage output from the H-bridge to the shift motor. The encoder comprises of 4 Hall Effect sensors and it requires a 5 V power supply. Each of the encoder signal wires will output either a high (5 V) or low (0 V) signal depending on the encoder position.

Reference [41] developed a wiring schematic that integrates the aforementioned electrical components. It also integrated many of the required electrical components beyond the Arduino on a custom fabricated PCB. Figure 4.15 displays the original wiring schematic to the Arduino while Figure 4.16 displays the schematic of the custom PCB.

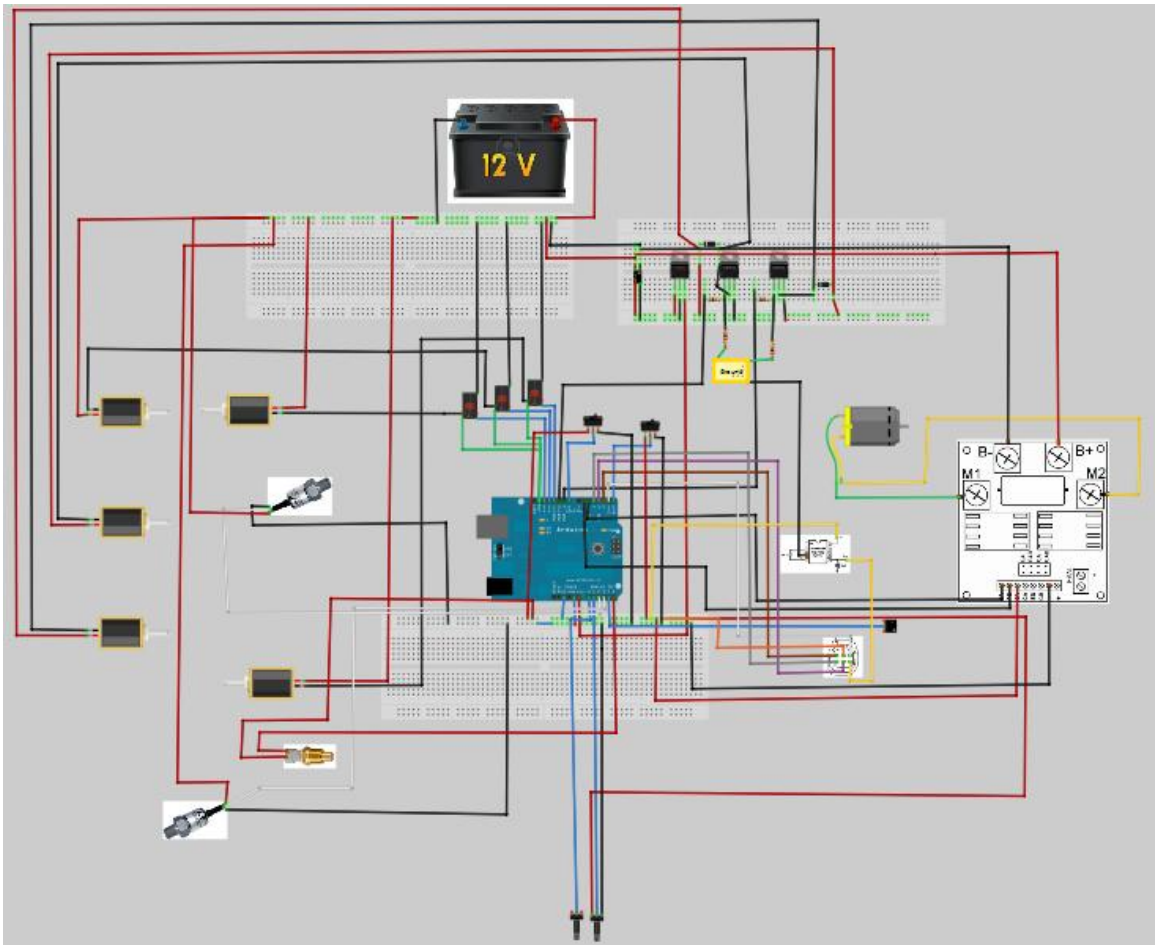

Figure 4.15: Wiring diagram to the Arduino, reproduced from [41]

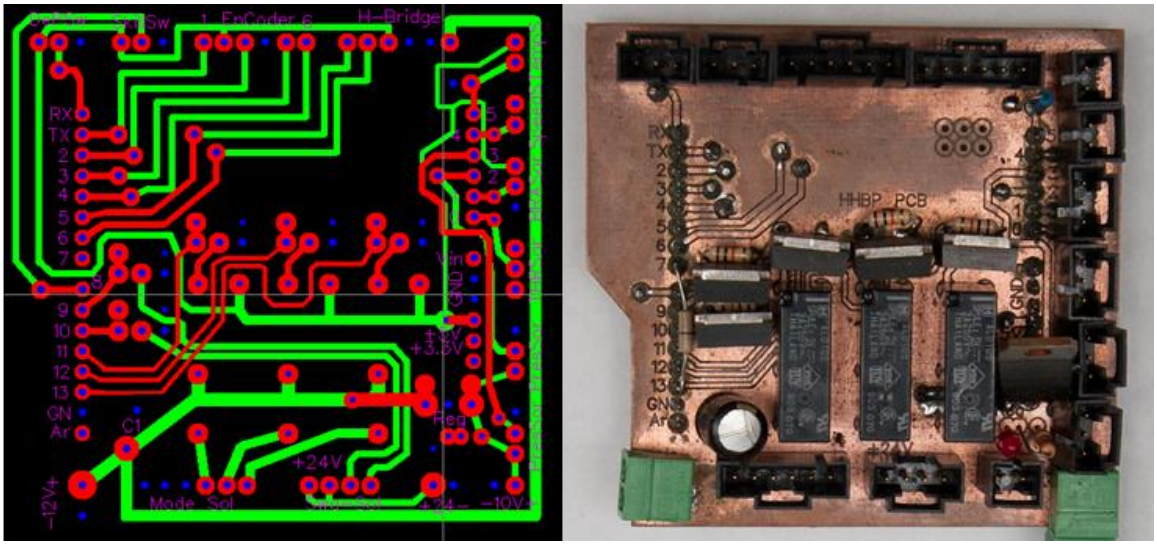

Figure 4.16: Custom PCB, reproduced from [41]

The custom PCB board has pin outputs that interface directly with the Arduino. Many components such sensors and solenoids connect to the Arduino through the PCB. A new wiring diagram shown in Figure 4.17 is developed for depicting the connections to the PCB. While the new wiring diagram is mostly consistent with the original one from [41], several changes were made to ensure the proper operations of the HHB components. Pull-down resistors were added to the signal pins of the switches, to ensure proper readings. The original wiring diagram suggested supplying a –5 V power to the encoder. This was circumvented by adding pull-down resistors to the signal pins of the encoder. Finally, the new wiring diagram also depicts the wiring of the 24 V voltage converter to the 12 V battery and an additional switch that controls the power supplied to the microcontroller from the battery.

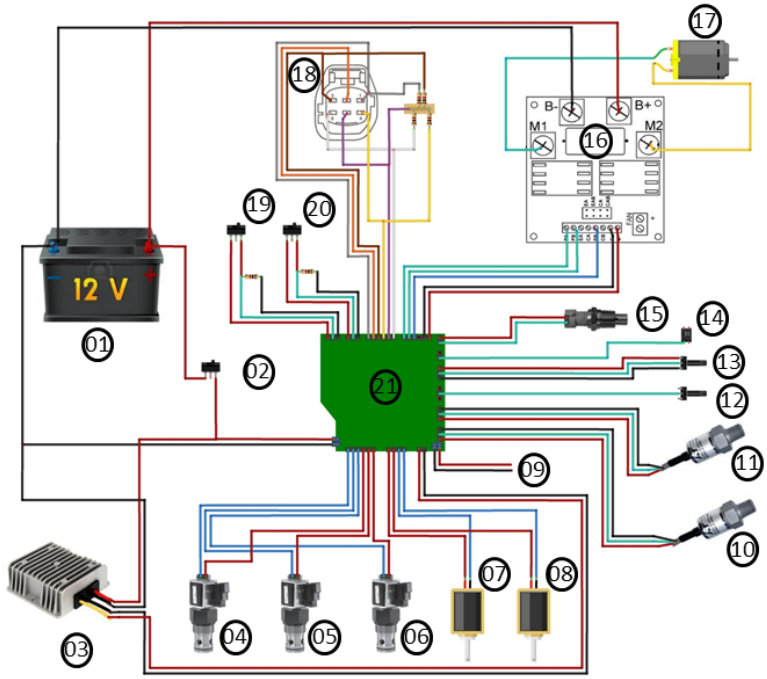

Number	Description
01	12V Battery
02	On/off switch
03	12V to 24V converter
04	Control pressure sol.
05	Parallel solenoid 1
06	Parallel solenoid 2
07	Swash plate sol. Mz
08	Swash plate sol. My
09	To Arduino power
10	High pressure sensor
11	Low pressure sensor
12	Throttle potentiometer
13	Brake potentiometer
14	Transmission speed sensor
15	Temperature sensor
16	H-bridge
17	Transfer case shift motor
18	Encoder
19	Control pressure sol. switch
20	Parallel sol. switch
21	PCB board

Figure 4.17: Wiring to the custom PCB

4.4.2.3 Controller Logic

The section will describe the control logic implemented in the Arduino-based microcontroller for the hydraulic system. The control logic closely follows the maximum *SOC* approach, which seeks to keep the accumulator stored energy level as high as possible. Furthermore, the hydraulic system controller does not interface with the engine control unit (ECU) of the bus except for monitoring two sensor signals. This allows the bus to maintain normal operation in the event of a failure of the hydraulic system controller. Figure 4.18 shows the top level decision making flow-chart of the microcontroller.

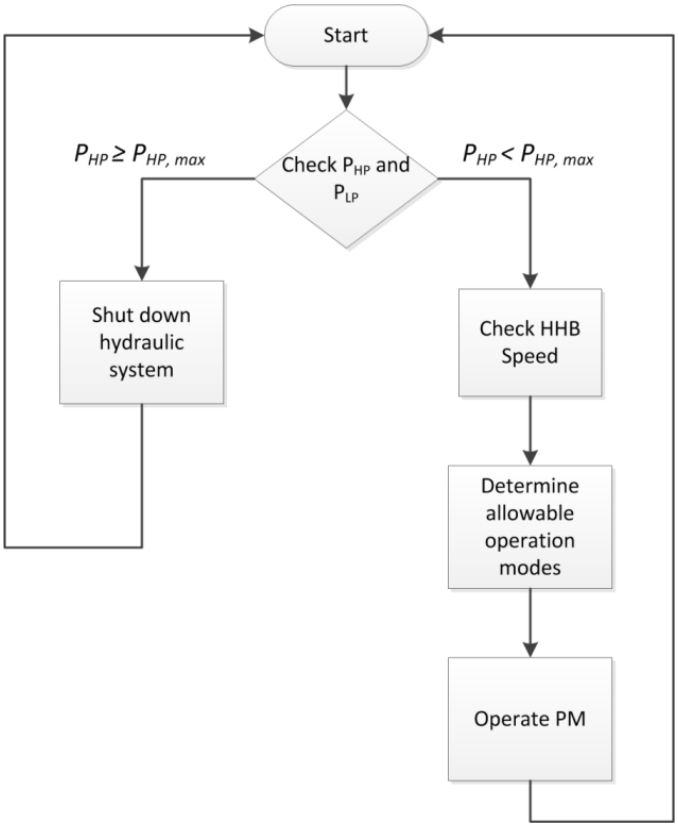

Figure 4.18: Top-level decision making flow-chart of the HHB controller

The controller will first check the pressure of the HP accumulator to ensure it has not reached the maximum allowable system pressure of 4500 psi. If the maximum pressure is reached, the control logic shuts down the hydraulic system until the pressure returns to a normal level. Otherwise, the controller will proceed with the regular operation procedures, which includes determining the allowable operation modes and operating the PM. The control logic determines the allowable operation modes based on current pressures in the accumulators and the driveshaft RPM. The microcontroller operates the accumulators between 120% and 300% of their pre-charged pressures as specified by the accumulator manufacturer [44]. Braking with the PM is not allowed at low driveshaft speed (<100 RPM), due to the extremely low volumetric efficiency of PM at speed and the possibility of propelling the HHB backward. On the other hand, motoring with the PM is currently allowed from zero driveshaft speed, which allows the PM to motor the HHB from standstill even with the engine off. However, unless an engine start-stop feature is integrated, it is more efficient to not operate the PM at low speeds.

Figure 4.19 further details the decision making in the "Operate PM" process in Figure 4.18. In this process, the microcontroller first checks whether the brake pedal is depressed. In the event where the brake pedal is depressed, the microcontroller checks whether hydraulic braking is allowable and sends appropriate signals to the swash plate solenoids if appropriate. If the brake pedal is not depressed, the microcontroller will then check whether the throttle pedal is depressed.

In contrast to the case of the brake pedal depression, the hydraulic system will either motor or brake depending on the level of throttle pedal depression. With light throttle pedal depression, the hydraulic system attempts to store energy in the HP accumulator at

the expense of the engine power where admissible. This is to maintain the accumulator *SOC* as high as possible. However, with heavy throttle pedal depression signaling a strong acceleration request, the microcontroller will use the PM to assist the HHB engine instead.

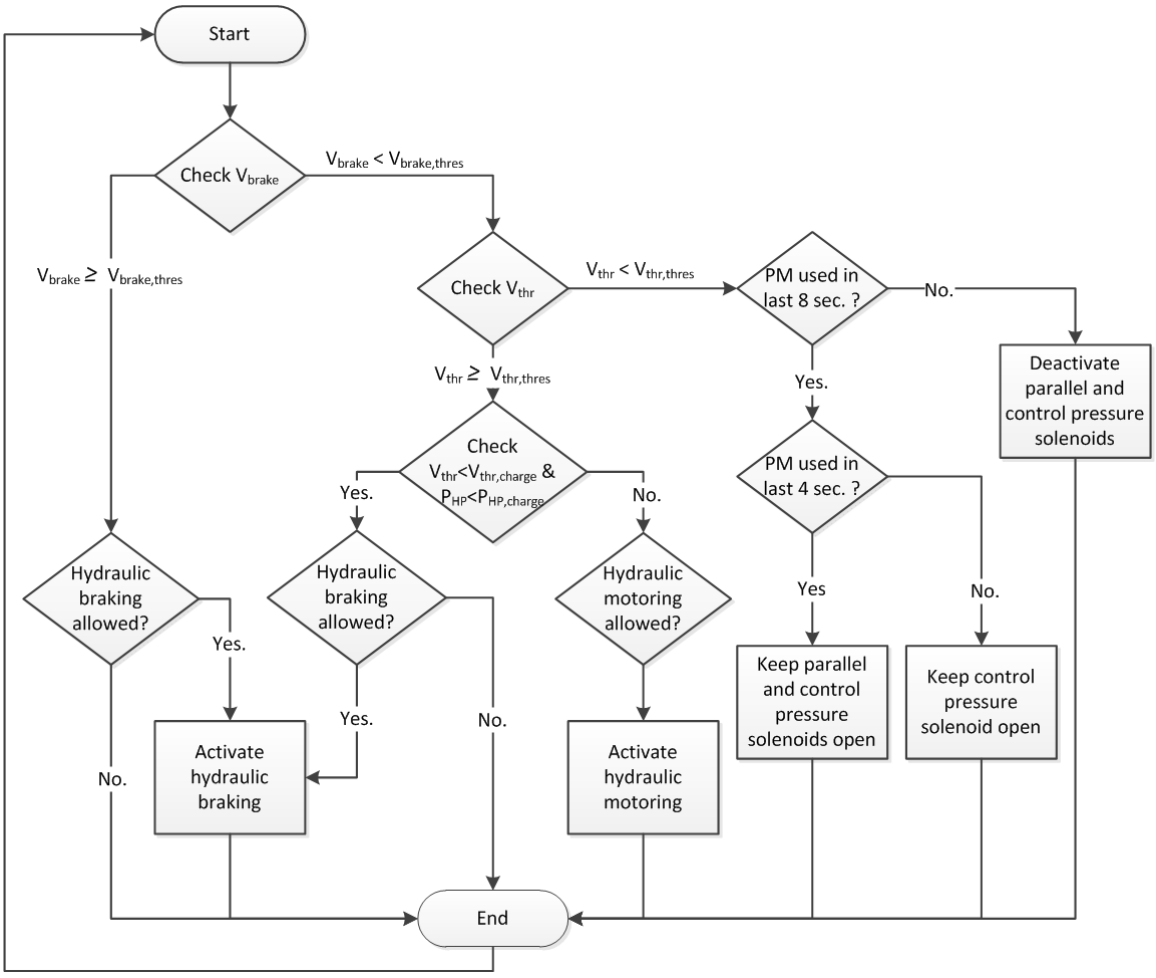

Figure 4.19: Operation flow-chart of the PM

Finally, if neither the brake nor the throttle pedal is depressed, the microcontroller will attempt to return the PM swash plate back to neutral. The is crucial since if the PM shaft rotates with the swash plate not at its neutral position, and the parallel solenoids are

closed, large pressure spikes can occur in the hydraulic system. This effect not only creates drag in the drivetrain, but also risks damaging the hydraulic components. Therefore, the microcontroller keeps the control pressure solenoid valve and the parallel solenoid valves open for 8 seconds and 4 seconds respectively following a swash plate actuation. Keeping the control pressure solenoid valve open facilitates neutral return of the swash plate while opening the parallel solenoids valves avoids large pressure spikes.

4.5 Preliminary Results

This section will discuss the preliminary results of the HHB prototype testing. Discussed will the simulated fuel economy improvements and testing highlights of the HHB prototype. Based on these results, the section will comment on the commercialization potential of the HHB prototype.

Using the exact configuration outfitted to the HHB in the forward-looking simulator, the fuel economy of the HHB over the reduced speed UDDS drive cycle is 10.83 MPG. This represent a 24% improvement over the 8.72 MPG simulate fuel economy of the unmodified baseline model. Using these numbers, the breakeven time frame for converting a bus to a hydraulic hybrid will be 8.92 years. The breakeven analysis is attached as Tables C.1 and C.2 in Appendix C. However, these fuel economy numbers are very conservative. First, the drive cycle assumed is for a passenger vehicle driving in an urban environment. However, school buses and transit buses will likely make frequent stops to pick up and drop off passengers. The hydraulic hybridization will bring much greater benefits under these start-and-stop operations. For example, in a study published by U.S. Department of Transportation, the fuel economy of a transit bus can be as low as 3.85 MPG [47]. If the percent fuel economy improvement remains the same

24%, the annual fuel cost saving will more than double, and this will decrease the breakeven time in half. Finally, the fuel saving analysis is performed using the diesel price on September 17, 2012. As demonstrated in Chapter 1, oil prices historically increase over time. This will also increase the annual fuel cost saving as the price of oil goes up.

Prototype testing efforts to date demonstrate the proof of concept and system operation. Experimental fuel economy testing has not been conducted due to highway regulation and venue constraints. Nevertheless, the hydraulic system has been pressurized to 3000 psi and the HHB prototype has been driven in a parking lot at up to 20 MPH. Furthermore, with the HP accumulator pressurized to 2000 psi, the hydraulic PM can move the HHB from a standstill to approximately 10 MPH. Issues arise from testing mainly involve the control pressure to the swash plate solenoids. As detailed before, the HHB currently reduces the pressure in the HP accumulator to 290 psi to provide the control pressure flow to the swash plate solenoids. This is very energy-inefficient and at times problematic. For example, accidental total pressure depletion of the HP accumulator will render the PM inoperable. The ideal solution would be to outfit the HHB with a PM that contains an internally geared boost pressure pump providing the control pressure. With the simulated fuel economy results and system capabilities demonstrated so far, the HHB prototype shows strong promise for commercialization with further refinement and experimental fuel economy testing. Furthermore, since the hybrid system is developed to be retrofitted on existing buses, the cost of switching to a hydraulic hybrid is much lower than purchasing an entirely new vehicle. Finally, oil

price and federal regulation conditions detailed in Chapter 1 will further increase demand for this hydraulic hybrid system.

4.6 Summary

This chapter presents the development of a hydraulic hybrid bus prototype. The design and operations of the hydraulic circuit are reviewed. Sizing of key components, specifically accumulator volume and pump/motor max displacement, is informed by a forward-looking simulator. The chapter then describes the hydraulic system and microcontroller outfitted to the HHB. Specifically, the chapter discusses operation characteristics of each component and identifies the PM being the key area for improvement. A control logic based on the maximum *SOC* strategy is also detailed, supplementing the information for the microcontroller design. Finally, simulated fuel economy data suggests the commercial viability of the system while the testing of the HHB prototype to date provides a proof of concept. The commercial viability of the HHB is also supported by the relative cheap cost of retrofitting and the increasing pressure from oil prices and government regulations.

CHAPTER 5

CONCLUDING REMARKS AND FUTURE WORK

This thesis presents development of simulation tools, control strategies, and a hydraulic hybrid prototype. It focuses simulation and control strategy work on hybrid electric vehicles (HEV), while details the design and development of the hydraulic hybrid bus (HHV) prototype. This chapter will provide concluding remarks for the thesis and suggest future work.

5.1 Simulation Tools and Control Strategies for Hybrid Electric Vehicles

In Chapter 2, a dynamic programming (DP)-informed online implementable supervisory control strategy is developed. The strategy is based on the Equivalent Cost Minimization Strategy (ECMS), which assigns an equivalent fuel for battery power. Chapter 2 demonstrates that the equivalence cost of battery can be constant and the controller can still attain near globally optimal fuel economy performance. As the control policies of both DP and ECMS have to be Pareto-optimal, DP results can in fact inform the decision of the equivalence factor. The definition of equivalence cost has great impact on the resulting fuel economy. Factors such as drive cycle and component variation will all change the optimal equivalence factor. To address these issues, Chapter 2 develops a robust form of the ECMS controller. This controller uses DP to inform a reference equivalence factor and corrects it based on battery state of charge (*SOC*) deviations. Backward-looking simulations (BLS) of parallel and power-split HEVs are used to verify the controller performance. The case studies on two HEV architectures

show that the fuel economy performance of the robust ECMS controller is nearly indistinguishable from DP globally optimal results across different drive cycles.

Chapter 3 extends the DP-informed robust ECMS concept by implementing the controller in forward-looking simulations (FLS). In contrast to BLS where a drive cycle is assumed to be followed exactly and steady-state torque balances are used, FLS simulates a vehicle in high fidelity. In FLS, a simulated driver performs speed tracking of a drive cycle and issues acceleration or braking commands. The vehicle controller interprets these commands and outputs the appropriate torques to the wheels. This mimics the command structure of an actual vehicle. In addition, component transient effects are also simulated closely in FLS.

The vehicle modeled in Chapter 3 is based on the General Motor Allison Hybrid System-II (GM AHS-II). GM AHS-II is a power-split architecture with two different EVT modes, as opposed to the single mode EVT studied in Chapter 2. This further verifies the cross platform applicability of the robust controller. Controller development for FLS employs component look-up tables generated using BLS. Simulations results demonstrate that BLS and FLS show good agreement in terms of component operation states. Fuel economy of FLS is consistently lower than that from BLS, as expected since extra propulsion energy is required at the wheels in FLS. Ultimately, application of the robust ECMS in FLS demonstrates its potential for online application.

Both Chapter 2 and Chapter 3 analyze the controller performance based on fuel economy. This is only one of the many performance metrics for an HEV. Vehicle manufacturers have to meet multiple design goals, such as emission and drivability. One area for future work is to develop a robust ECMS that can simultaneously minimize for

fuel economy and emissions. Another possible area is to investigate whether the robust ECMS controller will provide a pleasant driving experience for the end user, with less noise, vibration, and harshness (NVH).

5.2 Prototype of the Hydraulic Hybrid Bus

Chapter 4 details the development of a hydraulic hybrid prototype. While hybrid electric vehicles are widely available in the consumer market, the development of hydraulic hybrids is only in the nebular stage. This work serves to further the progress of hydraulic hybrids.

The hydraulic hybrid prototype is built by retrofitting a Bluebird school bus with hydraulic components. The architecture chosen is a post-transmission parallel type where both the engine and the hydraulic pump/motor (PM) drive the rear wheels directly. This setup allows hybridization with minimum modification to the existing drivetrain. A forward-looking simulator informs component sizing decisions and predicts favorable fuel economy improvement. Preliminary testing of the hybrid bus provides proof of concept and shows strong potential for commercial application.

The hybrid bus can be improved with a different pump/motor. The solenoids that control the variable displacement of the PM require a constant 290 psi pressure to function; this pressure is currently provided by reducing pressure from the high pressure accumulator. This is not the most efficient manner and implies that the PM will be inoperable if the high pressure accumulator is empty of hydraulic fluid. Future work should address this issue by implementing a PM with an internally geared pump to provide the constant 290 psi pressure.

Another area for improvement is the controller of the hydraulic system. While the current Arduino-based controller is adequate for testing purpose, its processing speed and input/output (I/O) capabilities are limited. Ongoing research is underway using a National Instrument sbRIO real time controller to replace the Arduino-based controller. The increased processing speed and number of I/O ports will allow for future expansion of controller features, furthering its commercial application potential.

APPENDIX A:

SUPPLEMENTARY MATERIAL TO CHAPTER 2

Tables A.1 and Table A.2 provide the simulation parameters for the parallel and power-split HEV architectures considered in Chapter 2. The diesel engine parameters in the parallel HEV are sourced from [48], while the gasoline engine model in the power-split HEV is based on the 57-kW engine used in the 2004 Prius sourced from PSAT [49]. Figures A.1 and A.2 display the brake specific fuel consumption maps and max torque capability curves used in the simulations. Finally, electric machine parameters for both HEVs are also sourced from PSAT [49], in the form of torque capability curves and combined EM and inverter efficiencies. Tables A.3-A.8 contain the fuel economy data set used to generate the fuel economy comparison charts presented in Section 2.4 of Chapter 2. All fuel economy figures are normalized to the DP numbers.

Table A.1: Parallel HEV simulation parameters

Chassis	
Mass, kg	1380
Mass Factor	1.2
Drag Coefficient	0.386
Frontal Area, m^2	2.642
Tire Radius, m	0.3
Rolling Resistance Coefficient	0.015
Drivetrain	
Transmission Gear Ratios	[3.45, 1.95, 1.28, 0.88, 0.67]
Final Drive Gear Ratio	2.67
Torque Coupling Gear Ratio	1
Engine	
Type	Diesel [48], also see Figure A.1.
Power, kW	64
Max Torque, Nm	186
Max Speed, RPM	3500
Electric Machine	
Type	Permanent Magnet [49]
Power, kW	50
Max Torque, Nm	400
Max Speed, RPM	6200
Battery	
Voltage, V	201.6
Capacity, Ahr	10

Table A.2: Power-split HEV simulation parameters

Chassis	
Mass, kg	1380
Mass Factor	1.2
Drag Coefficient	0.386
Frontal Area, m^2	2.642
Tire Radius, m	0.3
Rolling Resistance Coefficient	0.015
Drivetrain	
Planetary Gear Characteristic Ratio	30/78
Final Drive Gear Ratio	4.113
Engine	
Type	Gasoline [49], also see Figure A.2
Power, kW	57
Max Torque, Nm	123
Max Speed, RPM	4500
Electric Machine 1	
Type	Permanent Magnet [49]
Power, kW	50
Max Torque, Nm	400
Max Speed, RPM	6200
Electric Machine 2	
Type	Permanent Magnet [49]
Power, kW	30
Max Torque, Nm	153
Max Speed, RPM	10000
Battery	
Voltage, V	201.6
Capacity, Ahr	10

Table A.3: Parallel HEV fuel economy data normalized to DP with controllers optimized for the UDDS drive cycle

	LA92	NYCC	US06	HWFET	UDDS
DP	1.000	1.000	1.000	1.000	1.000
ECMS (const. s - brute force)	0.993	0.969	0.975	0.984	0.998
ECMS (const. s – avg. eff.)	0.758	0.697	0.839	0.804	0.714
ECMS (robust)	0.993	0.988	0.991	0.996	0.998

Table A.4: Power-split HEV fuel economy data normalized to DP with controllers optimized for the UDDS drive cycle

	LA92	NYCC	US06	HWFET	UDDS
DP	1.000	1.000	1.000	1.000	1.000
ECMS (const. s - brute force)	0.935	0.983	0.944	0.955	0.995
ECMS (const. s – avg. eff.)	0.795	0.658	0.875	0.928	0.791
ECMS (robust)	0.991	0.989	0.994	0.991	0.986

Table A.5: Parallel HEV fuel economy data normalized to DP with controllers optimized for the US06 drive cycle

	LA92	NYCC	US06	HWFET	UDDS
DP	1.000	1.000	1.000	1.000	1.000
ECMS (const. s - brute force)	0.936	0.923	0.995	0.966	0.936
ECMS (const. s – avg. eff.)	0.811	0.763	0.877	0.863	0.760
ECMS (robust)	0.993	0.988	0.990	0.996	0.997

Table A.6: Power-split HEV fuel economy data normalized to DP with controllers optimized for the US06 drive cycle

	LA92	NYCC	US06	HWFET	UDDS
DP	1.000	1.000	1.000	1.000	1.000
ECMS (const. s - brute force)	0.992	0.968	0.999	0.996	0.974
ECMS (const. s – avg. eff.)	0.797	0.662	0.875	0.929	0.793
ECMS (robust)	0.991	0.989	0.994	0.991	0.986

Table A.7: Parallel HEV fuel economy data normalized to DP with extreme range of s_{ref}

		LA92	NYCC	US06	HWFET	UDDS
DP		1.000	1.000	1.000	1.000	1.000
ECMS (const. s)	max	0.996	0.988	0.995	0.997	0.998
	min	0.808	0.751	0.854	0.821	0.765
ECMS (robust)	max	0.993	0.988	0.991	0.996	0.998
	min	0.991	0.987	0.989	0.995	0.997

Table A.8: Power-split HEV fuel economy data normalized to DP with extreme range of s_{ref}

		LA92	NYCC	US06	HWFET	UDDS
DP		1.000	1.000	1.000	1.000	1.000
ECMS (const. s)	max	0.998	0.998	1.001	0.996	0.995
	min	0.800	0.666	0.877	0.932	0.801
ECMS (robust)	max	0.991	0.989	0.996	0.991	0.986
	min	0.989	0.986	0.994	0.990	0.984

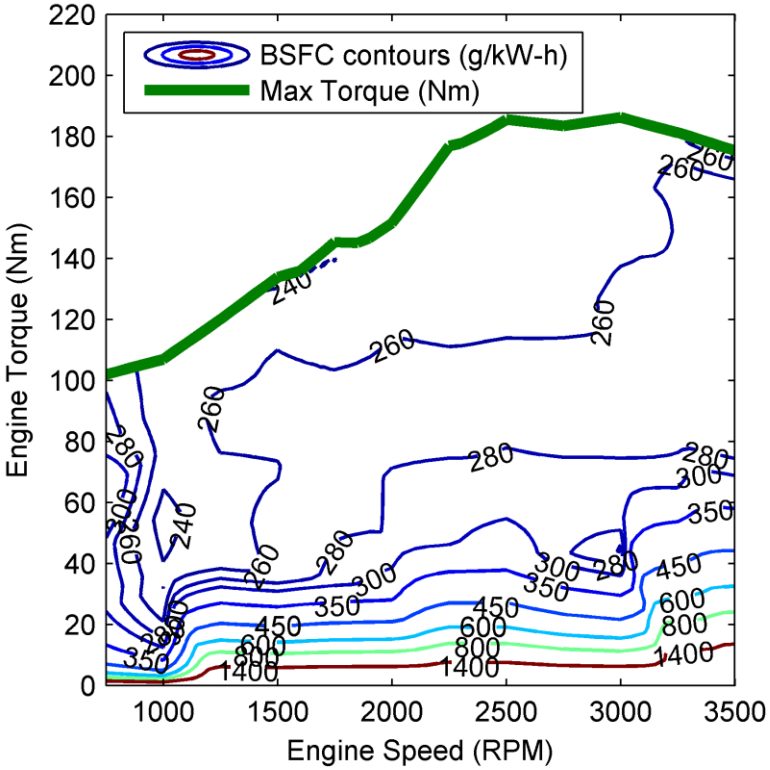

Figure A.1: Small diesel engine map, reproduced with data from [48]

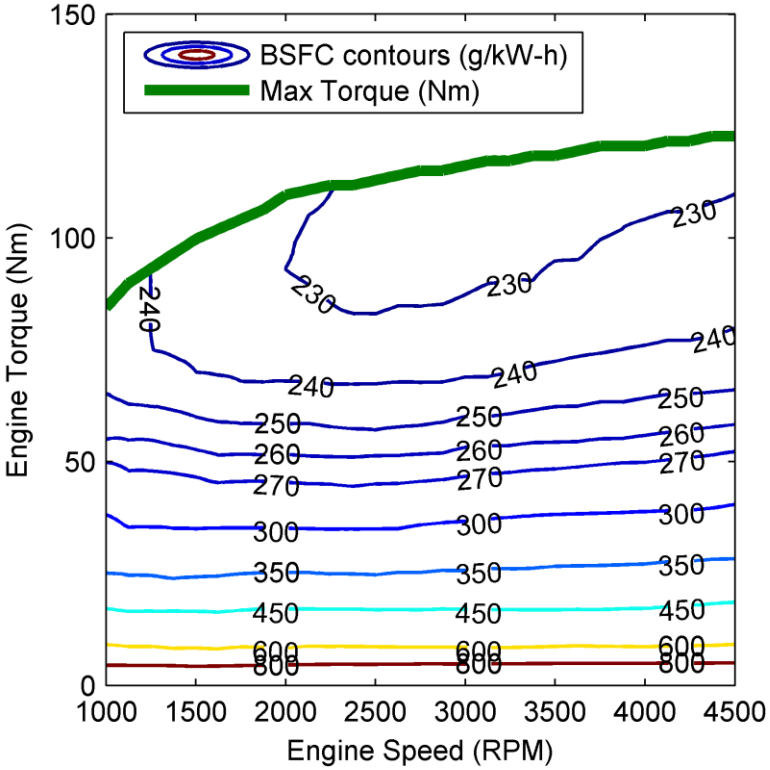

Figure A.2: Prius gasoline engine map, reproduced with data from [49]

APPENDIX B:

SUPPLEMENTARY MATERIAL TO CHAPTER 3

Table B.1: GM 2-mode power-split simulation parameters

Chassis	
Mass, kg	1380
Mass Factor	1
Drag Coefficient	0.386
Frontal Area, m^2	2.642
Tire Radius, m	0.3
Rolling Resistance Coefficient	0.015
Driveshaft Inertia, kg-m^2	1.5×10^{-3}
Drivetrain	
PG1 Characteristic Ratio	44/104
PG2 Characteristic Ratio	37/83
Final Drive Gear Ratio	3.02
Gear inertia, kg-m^2	1.5×10^{-4}
Engine	
Type	Gasoline [50], also see Figure B.1
Max Power, kW	84
Max Torque, Nm	149.5
Max Speed, RPM	6400
Inertia, kg-m^2	0.05
Electric Machine 1	
Type	Induction [51]
Max Power, kW	49
Max Torque, Nm	201
Max Speed, RPM	7500
Inertia, kg-m^2	0.02
Electric Machine 2	
Type	Induction [51]
Max Power, kW	60
Max Torque, Nm	235
Max Speed, RPM	9000
Inertia, kg-m^2	0.02
Battery	
Voltage, V	201.6
Capacity, Ahr	10
SOC Operating Range	0.4 - 0.8

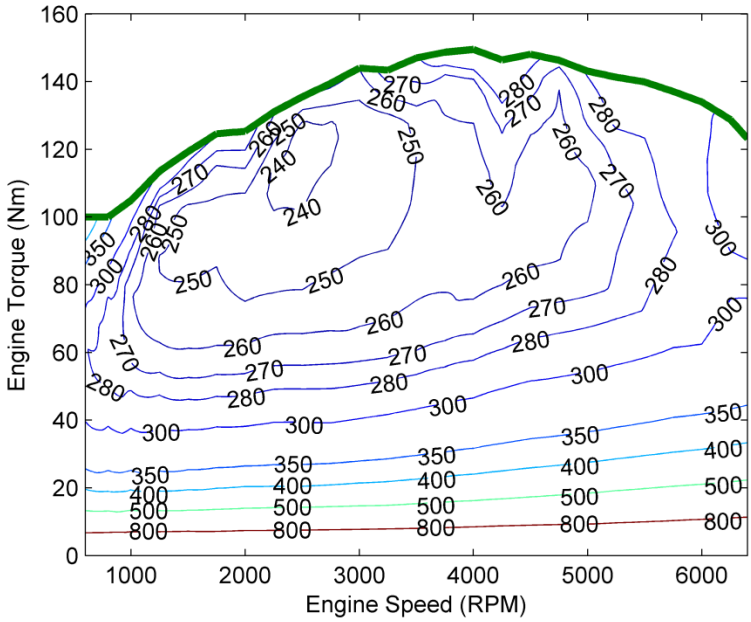

Figure B.1: GM 1.6 Lgasoline engine map, reproduced with data from [50]

APPENDIX C:

SUPPLEMENTARY MATERIAL TO CHAPTER 4

Figures C.1 and C.2 are the hydraulic fluid flow diagrams for the hydraulic hybrid bus. Figure C.3 provides a pictorial reference for the hydraulic components fitted to the HHB. Finally Table C.1 and C.2 document the break even analysis data for retrofitting a bus into a hydraulic hybrid.

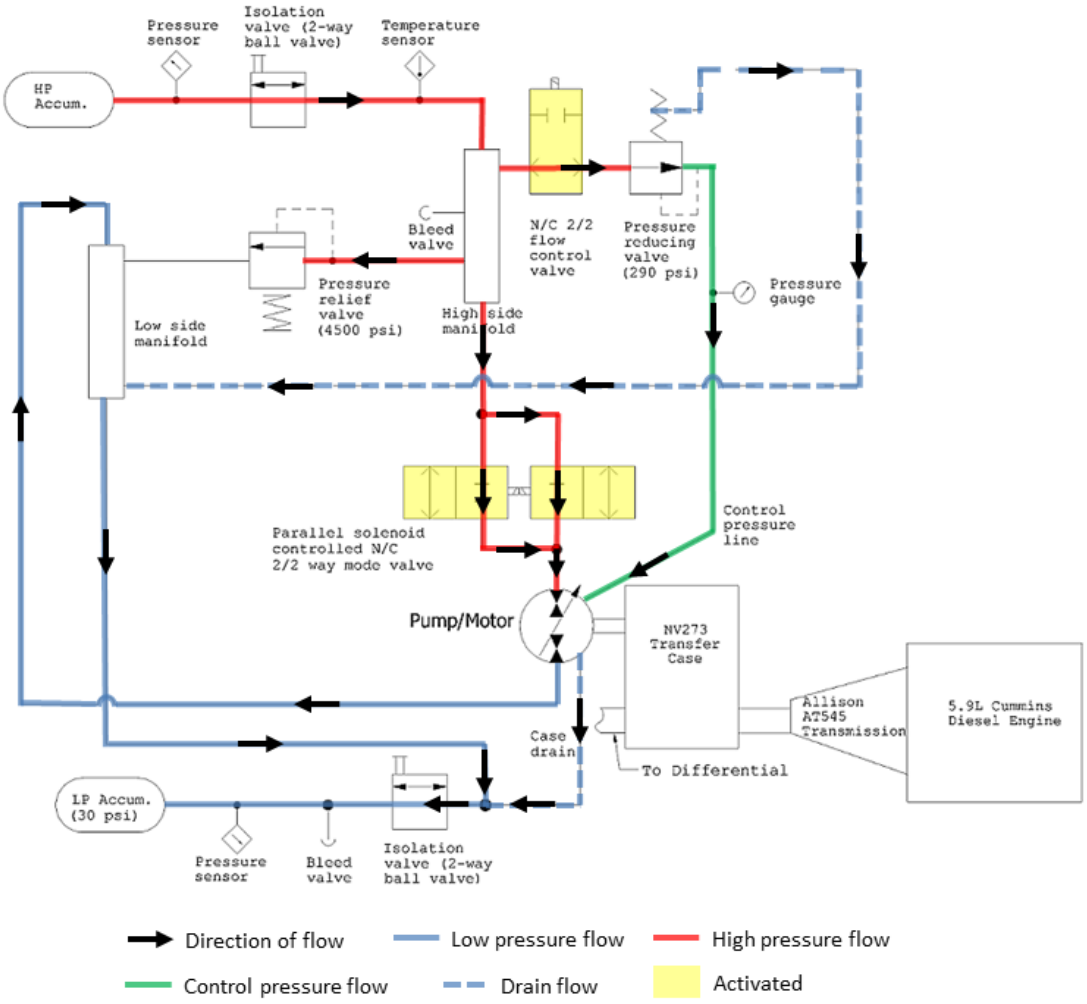

Figure C.1: Hydraulic fluid flow in the HHB during motoring

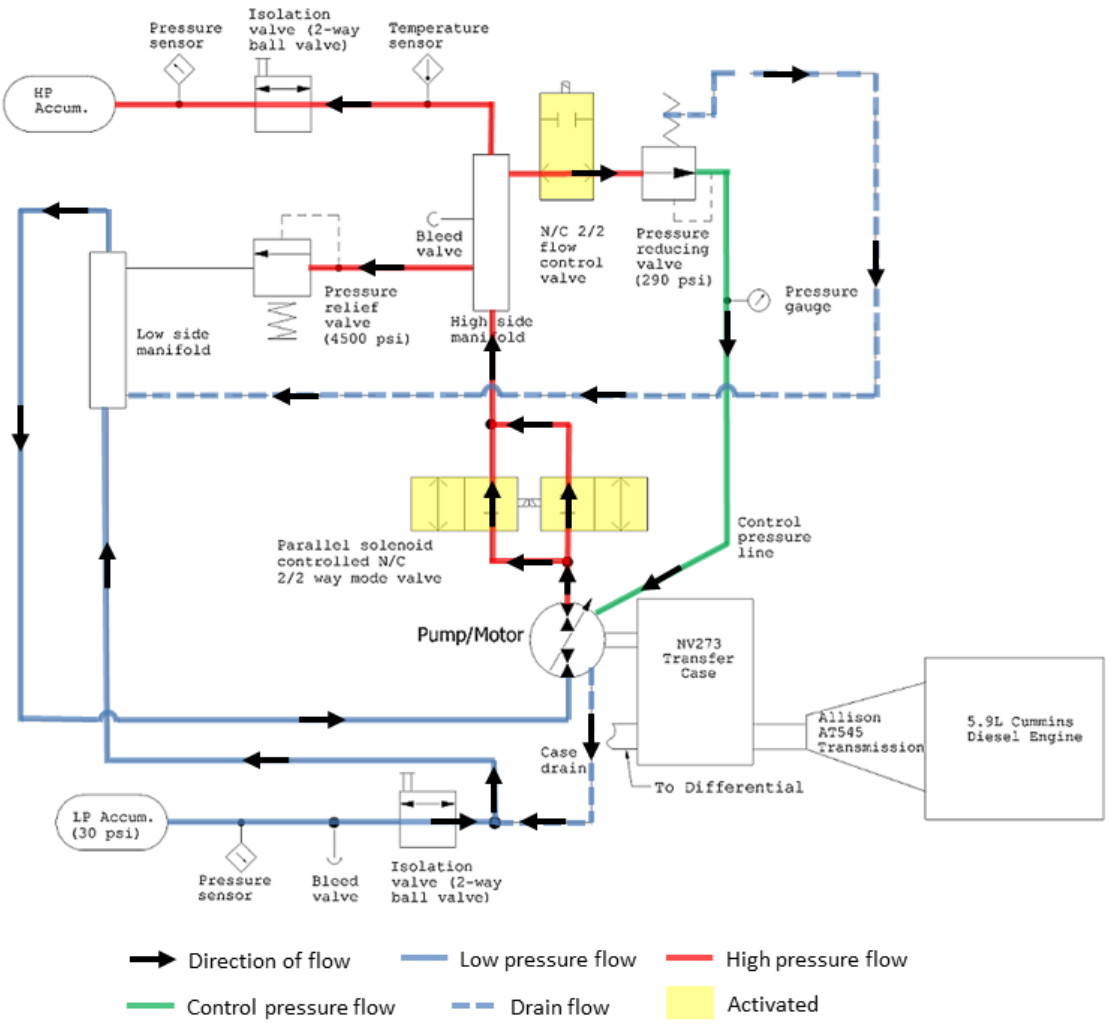

Figure C.2: Hydraulic fluid flow in the HHB during pumping

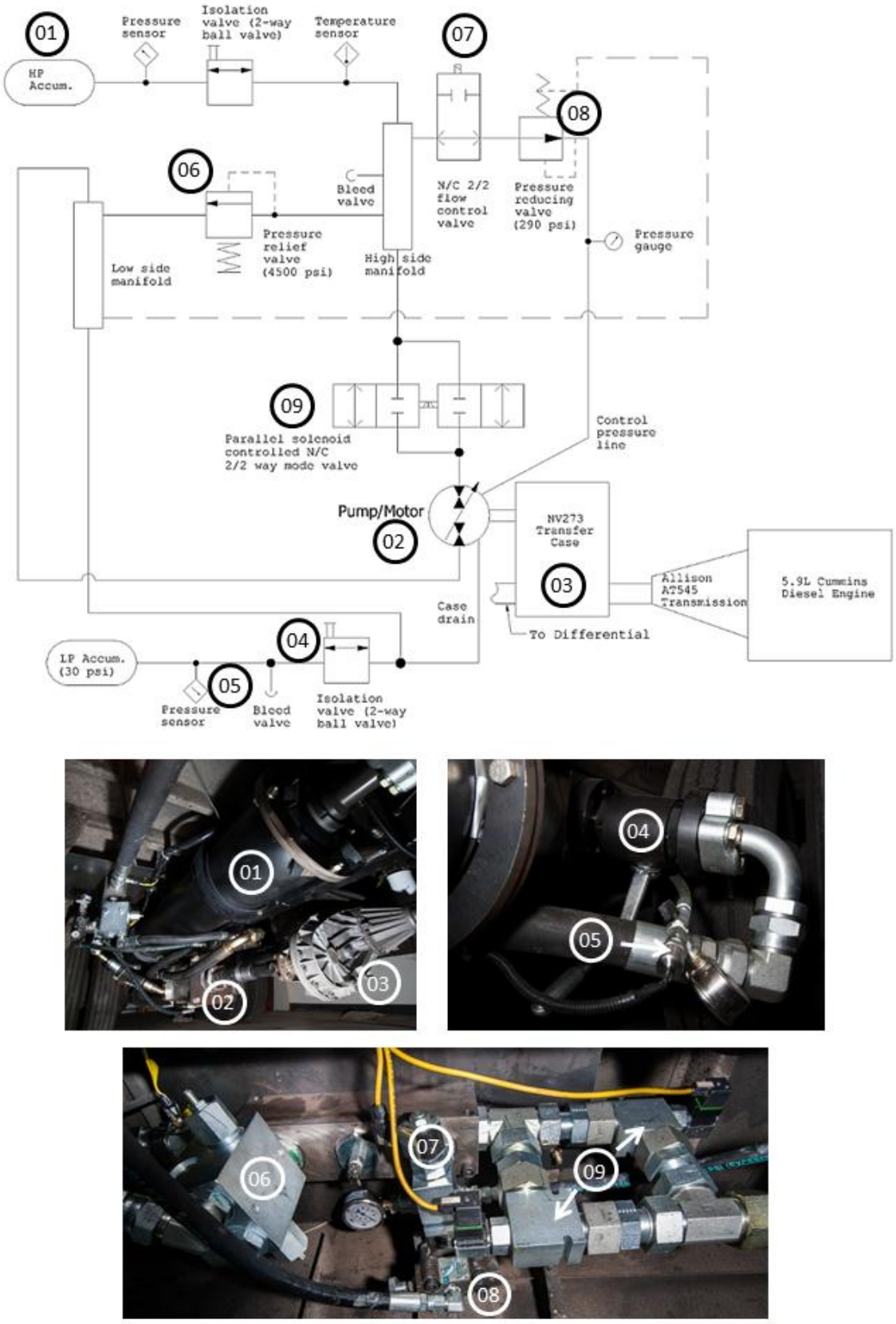

Figure C.3: Pictorial reference for the hydraulic components on the HHB

Table C.1: Break even analysis – estimation of retrofitting cost

Item	Cost	Quantity	Description	Cumulative Cost
DuraForce Pump	$8,000.00	1	Axial Piston Pump : HPV280 R0 T4ME 1D0L 21SA A000 0000 0000 00AA (price estimated)	$8,000.00
Transfer Case	$795.00	1	Transfer Case	$795.00
Pressure Sensors	$144.00	2	Sensors to get pressure of hydraulic fluid	$288.00
15 Gallon Accumulator - Accum. Inc.	$3,164.00	1	Accumulators, Inc 15 Gallon-6000psi Bottom Repairable Accumulator - Code 62 1.5" SAE Split Flange, Buna-Nitrile Bladder, A15610015	$3,164.00
DMIC Check Valve 1.5 SAE 5 PSI	$120.93	1	Check valve for pump case drain	$120.93
DMIC Ball Valve (C62 Companion connection)	$431.34	2	Accumulator isolation valves	$862.68
Parker Air Bleed Valve (1/4" MNPT)	$54.72	2	For bleeding air out of high and low pressure system sides	$109.44
Sterling Assembly - Parker - 2-way/nc, 2 position	$250.00	2	Solenoid mode valves	$500.00
MEC STD Valve Assembly - Relief Valve 5000 psi.	$420.59	1	Relief valve between high and low pressure accumulators	$420.59
N/O Accumulator Dump Valve to Unload Accumulator	$150.00	1	Normally open solenoid valve for unloading high pressure accumulator	$150.00
Sun Hydraulics Relief Valve (SAE8)	$85.00	1	RPEC-LAN-FAJ/S 290 psi pressure relief	$85.00
Veljan Pressure Reducing Valve (NPTF 3/4") 100-5000psi	$906.27	1	VR4R06-5A5-12B1	$906.27
A36 Steel	$0.45	300	A36 Steel, price in lbs	$135.00
2x4x1/4" Rectangular Steel Tube	$98.40	1	2x4x1/4" Rectangular Steel Tube	$98.40
Fastners Package	$50.00	1	Misc. Bolts/flat washers/lock washers	$50.00
1/4" Thick Neoprene Rubber	$10.12	5	1/4" Thick Neoprene Rubber	$50.60
1/4" Thick Silicone Rubber	$4.07	9	1/4" Thick Silicone Rubber	$36.63
2x2x0.25" Square	$0.55	25		$13.75

Item	Cost	Quantity	Description	Cumulative Cost
Steel Tube				
3/16" Neoprene Rubber	$34.83	1	For damping	$34.83
4x4x0.375" Steel Angle	$1.00	20		$20.00
Hoses Package	$1,993.75	1		$1,993.75
Microcontroller	$77.50	1	Microcontroller assembly	$77.50
			Total Prototyping cost:	$17,834.87
			Optimized cost @ 40%:	$10,700.92
			Annual Fuel Saving	$1,199.34
			Break Even Years	8.92

Table C.2: Break even analysis – estimation of annual fuel saving for a single bus

	Average Gallon Cost of Diesel	$4.14
	Miles Driven Per Year	13000
Regular	Average MPG	8.7235
	Gallons of Diesel Per Year	1490
	Average Cost of Diesel Fuel Per Year	$6,162.09
HHB	Average MPG	10.8317
	Gallons of Diesel Per Year	1200
	Average Cost of Diesel Fuel Per Year	$4,962.75
	Fuel Savings	$1,199.34

REFERENCES

[1] U.S. Energy Information Administration, 2012, "Spot Prices," from http://www.eia.gov/dnav/pet/pet_pri_spt_s1_d.htm.

[2] National Highway Traffic Safety Administration, 2012, "FACTSHEET: Paving the Way Toward cleaner, More Efficient Trucks," from http://www.nhtsa.gov/staticfiles/rulemaking/pdf/cafe/Factsheet.08092011.pdf.

[3] Bureau of Transportation Statistics, 2012, "National Transportation Statistics," from http://www.bts.gov/publications/national_transportation_statistics/#front_matter.

[4] U.S. Department of Energy and U.S. Environmental Protection Agency, "Advanced Vehicles & Fuels," from www.fueleconomy.gov.

[5] National Highway Traffic Safety Administration, 2012, "2017 and Later Model Year Light-Duty Vehicle GHG Emissions and CAFÉ Standards: Supplemental Notice of Intent," from http://www.nhtsa.gov/staticfiles/rulemaking/pdf/cafe/2017-2025_CAFE-GHG_Supplemental_NOI07292011.pdf.

[6] Ehsani, M., Gao, Y., and Emadi, A., 2009, *Modern Electric, Hybrid Electric, and Fuel Cell Vehicles*, 2nd ed., CRC Press, Boca Raton, FL.

[7] Salmasi, F. R., 2007, "Control Strategies for Hybrid Electric Vehicles: Evolution, Classification, Comparison, and Future Trends," *IEEE Trans. Veh. Technol.,* 56(5), pp. 2393-2404.

[8] Arata, J., Leamy, M., Meisel, J., Cunefare, K., and Taylor, D., 2011, "Backward-Looking Simulation of the Toyota Prius and General Motors Two-Mode Power-Split HEV Powertrains," *SAE Int. J. Engines*, 4(1), pp. 1281-1297.

[9] Schouten, N. J., Salman, M. A., and Kheir, N. A., 2002, "Fuzzy Logic Control for Parallel Hybrid Vehicles," *IEEE Trans. Control Syst. Technol.*, 10(3), pp. 460-468.

[10] Lee, H. and Sul, S., 1998, "Fuzzy-Logic-Based Torque Control Strategy for Parallel-Type Hybrid Electric Vehicle," *IEEE Trans. Ind. Electron.*, 45(4), pp. 625-632.

[11] Serrao, L., Onori, S., and Rizzoni, G., 2011, "A Comparative Analysis of Energy Management Strategies for Hybrid Electric Vehicles," *J. Dyn. Sys., Meas., and Control*, 133(3), 031012.

[12] Kum, D., Peng, H., and Bucknor, N. K., 2011, "Supervisory Control of Parallel Hybrid Electric Vehicles for Fuel and Emission Reduction," *J. Dyn. Sys., Meas., and Control*, 133(6), 061010.

[13] Lin, C., Peng, H., Grizzel, J. W., and Kang, J., 2003, "Power Management Strategy for a Parallel Hybrid Electric Truck," *IEEE Trans. Contr. Syst. Technol.*, 11(6), pp. 839-849.

[14] Sundstrom, O. and Guzzella, L., 2009, "A Generic Dynamic Programming Matlab Function," *Control Applications, (CCA) & Intelligent Control, (ISIC)*, IEEE, pp. 1625-1630.

[15] Sciarretta, A., Back, M., and Guzzella, L., 2004, "Optimal Control of Parallel Hybrid Electric Vehicles," *IEEE Trans. Contr. Syst. Technol.*, 12(3), pp. 352-363.

[16] Kim, N., Cha, S., and Peng, H., 2011, "Optimal Control of Hybrid Electric Vehicles Based on Pontryagin's Minimum Principle," *IEEE Trans. Contr. Syst. Technol.*, 19(5), pp.1279-1287.

[17] Serrao, L., Onori, S., and Rizzoni, G., 2009, "ECMS as a Realization of Pontryagin's Minimum Principle for HEV Control," *2009 American Control Conference*, IEEE, pp. 3964-3969.

[18] Paganelli, G., Delprat, S., Guerra, T. M., Rimaux, J., and Santin, J. J., 2002, "Equivalent Consumption Minimization Strategy for Parallel Hybrid Powertrains," *Vehicular Technology Conference*, IEEE, 4, pp.2076-2081.

[19] Musardo, C., Rizzoni, G., and Staccia, B., 2005, "A-ECMS: An Adaptive Algorithm for Hybrid Electric Vehicle Energy Management," *Proceedings of the 44th IEEE Conference on Decision and Control, and the European Control Conference 2005*, pp. 1816-1823.

[20] Liu, J., and Peng, H., 2008, "Modeling and Control of a Power-Split Hybrid Vehicle," *IEEE Trans. Contr. Syst. Technol.*, 16(6), pp. 1242-1251.

[21] U.S. Environmental Protection Agency, 2012, "Demonstration Vehicles," from http://www.epa.gov/oms/technology/research/demonstration-vehicles.htm.

[22] Matheson, P., and Stecki, J., 2003, "Development and Simulation of a Hydraulic-Hybrid Powertrain for use in Commercial Heavy Vehicles," *SAE Technical Paper* 2003-01-3370.

[23] Center for Compact and Efficient Fluid Power, 2012, "Highway Vehicles – Hydraulic Hybrid Passenger Vehicles (Test Bed 3)," from http://www.ccefp.org/research/testbeds/hydraulic-hybrid-passenger-vehicle.

[24] Kim, Y. and Filipi, Z., 2007, "Simulation Study of a Series Hydraulic Hybrid Propulsion System for a Light Truck," *SAE Technical Paper* 2007-01-4151.

[25] Matheson, P. and Stecki, J., 2003, "Modeling and Simulation of a Fuzzy Logic Controller for a Hydraulic-Hybrid Powertrain for Use in Heavy Commercial Vehicles," *SAE Technical Paper* 2003-01-3275.

[26] Wu, B., Lin, C., Filipi, Z., Peng, H., and Assanis, D., 2002, "Optimization of Power Management Strategies for a Hydraulic Hybrid Medium Truck," *Proceedings of the 2002 Advanced Vehicle Control Conference*.

[27] Li, C. and Peng, H., 2010 "Optimal Configuration Design for Hydraulic Split Hybrid Vehicles," *American Control Conference*, pp. 5812-5817.

[28] Litvin, F. L., Fuentes, A. F., Vecchiato, D., and Gonzales-Perez, I., 2004, "New Design and Improvement of Planetary Gear Trains," E-14576, University of Illinois, Chicago.

[29] Meisel, J., 2006, "An Analytic Foundation for the Toyota Prius THS-II Powertrain with a Comparison to a Strong Parallel Hybrid-Electric Powertrain," *SAE Technical Paper* 2006-01-0666.

[30] Bellman, R., 1957, *Dynamic Programming*, Princeton University Press, Princeton, N.J.

[31] Ahn, K., Cho, S., and Cha, S. W., 2008, "Optimal Operation Of The Power-Split Hybrid Electric Vehicle Powertrain", *Proceedings of the Institution of Mechanical Engineers, Part D: Journal of Automobile Engineering*, 222, pp.789-800.

[32] Li, S., Kolmanovsky, I. V., and Galip Ulsoy, A., 2012, "Distributed Supervisory Controller Design For Battery Swapping Modularity in Plug-In Hybrid Electric Vehicles," *J. Dyn. Sys., Meas., and Control*, 134(4), 041013.

[33] Meisel, J., 2011, "Kinematic Study of the GM Front-Wheel Drive Two-Mode Transmission and the Toyota Hybrid System THS-II Transmission," *SAE Int. J. Engines*, 4(1), pp.1020-1034.

[34] Hendrickson, J., Holmes, A., and Freiman, D., 2009, "General Motors Front Wheel Drive Two-Mode Hybrid Transmission," *SAE Technical Paper* 2009-01-0508.

[35] Conlon, B., 2005, "Comparative Analysis of Single and Combined Hybrid Electrically Variable Transmission Operating Modes," *SAE Technical Paper* 2005-01-1162.

[36] Arata, J., Leamy, M., and Cunefare, K., 2012, "Power-Split HEV Control Strategy Development with Refined Engine Transients," *SAE Technical Paper* 2012-01-0629.

[37] Schuette, A. R, 1971. "The Allison AT-540 Automatic Transmission in Utility Truck Applications," *SAE Technical Paper* 710658.

[38] Doidge, J. R., Cline, C. W., Green, L. E., 1994, "Hydraulic Control Systems," *Design Practices: Passenger Car Automatic Transmissions*, 3rd Ed., AE-18, Society of Automotive Engineers, Inc., Warrendale, PA, pp.631-636.

[39] Cornell, C. R., 1981, "Dynamic Simulation of a Hydrostatically Propelled Vehicle," *SAE Technical Paper* 811253.

[40] Linde America, 2011, "HPV280-02 Efficiencies", Bulletin No. HPV 280-02 03.07/026/02, from personal communication with Thomas Cleghorn of Linde America, also available in Nonlinear Mechanics Lab, Woodruff School of Mechanical Engineering, Georgia Institute of Technology, Atlanta, GA.

[41] Buchanan, A., Rhodes, D., Shoun, M., White, D., and Woodin, C., 2011, "Biofuel Hydraulic Bus Project Final Report," Nonlinear Mechanics Lab, Woodruff School of Mechanical Engineering, Georgia Institute of Technology, Atlanta, GA.

[42] Eaton Corporation, "DuraForce^{TM} HPV Varaible Pumps for Closed Loop Opeartion", Nonlinear Mechanics Lab, Woodruff School of Mechanical Engineering, Georgia Institute of Technology, Atlanta, GA.

[43] Linde America, 2011, "variable displacement pump", engineering drawing from personal communication with Thomas Cleghorn of Linde America, also available in the Nonlinear Mechanics Lab, Woodruff School of Mechanical Engineering, Georgia Institute of Technology, Atlanta, GA.

[44] Accumulators, Inc., 2012, "maintenance.pdf," available from http://www.accumulators.com/pdf/File/maintenance.pdf.

[45] Veljan Hydrair Limited, 2012, "Pilot Operated Pressure Reducer Valve – Series VR4R," available from http://www.veljan.in/press/vr4r03.pdf.

[46] Arduino, 2012, "Arduino Uno," available from http://arduino.cc/en/Main/ArduinoBoardUno.

[47] U.S. Department of Transportation Federal Transit Administration, 2012, "Transit Bus Life Cycle Cost and Year 2007 Emissions Estimation," available from http://www.fta.dot.gov/documents/WVU_FTA_LCC_Final_Report_07-23-2007.pdf.

[48] Rose-Hulman Institute of Technology and the MathWorks, 2009, "MBSD Lecture."

[49] Argonne National Laboratory, 2002, PSAT (Powertrain System Analysis Toolkit) 6.2.

[50] General Motors, 2012, "1.6L Fam 1 for Teams.xls", EcoCAR resource, also available in the Nonlinear Mechanics Lab, Woodruff School of Mechanical Engineering, Georgia Institute of Technology, Atlanta, GA.

[51] General Motors, 2012, "RWD Motor Power and Torque.xls", EcoCAR resource, also available in the Nonlinear Mechanics Lab, Woodruff School of Mechanical Engineering, Georgia Institute of Technology, Atlanta, GA.

[52] U.S. Environmental Protection Agency, 2012, "Dynamometer Drive Schedules," from http://www.epa.gov/nvfel/testing/dynamometer.htm.

[53] Fisker, 2012, "Specifications," from http://resources.fiskerautomotive.com/static/downloads/en-us/pdf/2012/karma/2012_Fisker_Karma_Vehicle_Specifications-v1.pdf.

[54] General Motor, 2012, "2013 Volt," from http://www.chevrolet.com/volt-electric-car.html.

[55] American Honda Motor, Co., Inc., "Insight – Overview," from http://automobiles.honda.com/insight-hybrid/.

[56] Hyundai Motor America, 2012, "Hybrid Mileage and Innovative Performance in Perfect Balance," https://www.hyundaiusa.com/vehicles/2012/sonata-hybrid/performance.aspx?.